ABSTRACT

Title of Document: Atomic Layer Deposition Conformality and Process Optimization: Transitioning from 2-Dimensional Planar Systems to 3-Dimensional Nano-structures

Erin D. Robertson Cleveland,
Doctor of Philosophy, 2010

Directed By: Professor Gary W. Rubloff,
Department of Materials Science and Engineering and the Institute for Systems Research

Conformal coatings are becoming increasingly important as technology heads towards the nanoscale. The exceptional thickness control (atomic scale) and conformality (uniformity over nanoscale 3D features) of atomic layer deposition (ALD) has made it the process of choice for numerous applications found in microelectronics and nanotechnology with a wide variety of ALD processes and resulting materials. While its benefits derive from self-limited saturating surface reactions of alternating gas precursors, process optimization for ALD conformality is

often difficult as process parameters, such as dosage, purge, temperature and pressure are often interdependent with one another, especially within the confines of an ultra-high aspect ratio nanopore. Therefore, processes must be optimized to achieve self-limiting saturated surfaces and avoid parasitic CVD-like reactions in order to maintain thickness control and achieve uniformity and conformality at the atomic level while preserving the desired materials' properties (electrical, optical, compositional, etc.).

This work investigates novel approaches to optimize ALD conformality when transitioning from a 2D planar system to a 3D ultra-high aspect ratio nanopore in the context of a cross-flow wafer-scale reactor used to highlight deviations from ideal ALD behavior. Porous anodic alumina (PAA) is used as a versatile platform to analyze $TiO_2$ ALD profiles via ex-situ SEM, EDS and TEM. Results of $TiO_2$ ALD illustrate enhanced growth rates that can occur when the precursors titanium tetraisopropoxide and ozone were used at minimal saturation doses for ALD and for considerably higher doses. The results also demonstrate that ALD process recipes that achieve excellent across-wafer uniformity across full 100 mm wafers do not produce conformal films in ultra-high aspect ratio nanopores. The results further demonstrate that conformality is determined by precursor dose, surface residence time, and purge time, creating large depletion gradients down the length of the nanopore. Also, deposition of ALD films over sharp surface features are very uniform, and verified by profile evolution modeling. This behavior, in contrast to that in high aspect ratio structures, suggests strongly that detailed dynamics, local flow conditions (e.g. viscous vs molecular), surface residence time, and ALD surface

reaction kinetics play a complex role in determining ALD profiles for high aspect ratio features.

# ATOMIC LAYER DEPOSITION CONFORMALITY AND PROCESS OPTIMIZATION: TRANSITIONING FROM 2-DIMENSIONAL PLANAR SYSTEMS TO 3-DIMENSIONAL NANO-STRUCTURES

By

Erin Darcy Robertson Cleveland

Dissertation submitted to the Faculty of the Graduate School of the
University of Maryland, College Park, in partial fulfillment
of the requirements for the degree of
Doctor of Philosophy
2010

Advisory Committee:

Professor Gary W. Rubloff, Chair

Professor Ray Adomaitis

Professor Robert M. Briber

Professor Joonil Seog

Professor John Cumings

# Dedication

This work is dedicated to my amazing husband, Ernie, and my mom and dad, who always believed in me and reminded me I could do this. Do you know something?

# Acknowledgements

I would like to thank all those who contributed to the development of my research and helped refine my research skills. I especially want to thank my advisor, Dr. Gary Rubloff for providing me with the opportunity and encouragement to explore and develop my scientific creativity. His guidance has helped me gain independence and a sense of confidence in my ability to do research. I would also like to thank past, current, and honorary students of the Rubloff group, especially Dr. Susan Buckhout-White, Dr. Israel Perez, Dr. Laurent Lecordier, Dr. Sebastian Engelmann, and Parag Banerjee. Thank you to Dr. Perez and Mr. Banerjee for insightful discussions about my research. Thank you to Dr. Lecordier for taking the time to teach me in and out of the lab. Thank you to Dr. Buckhout-White for being my hero and Dr. Engelmann for being a great roommate and role model.

I want to acknowledge the Maryland Nanocenter Staff, FabLab staff, and NispLab staff. I particularly want to thank Li-Chung (Larry) Lai of the NispLab for all of his support and guidance with SEM, EDS, and TEM training and image analysis. I would also like to acknowledge Wonseok Hwang of Dr. Joonil Seog's research group at the University of Maryland for his time in making AFM measurements.

This work was supported in part by the Laboratroy for Physical Science (LPS), the UMD-NSF-MRSEC under grant DMR 05-20471, and the FabLab and NispLab facilities in the Maryland NanoCenter.

# Table of Contents

# List of Tables



# List of Figures

# Chapter 1 : Introduction

## 1.1 Atomic Layer Deposition (ALD)

### 1.1.1 Background on ALD

ALD is a gas phase deposition technique which utilizes self-limiting chemistries in order to produce thin solid films down to the atomic scale. ALD is widely accepted as a means to produce high quality films with thickness control (Figure 1) over large surface areas with excellent uniformity and unprecedented conformality (Figure 2).[1-6] These key attributes are inherent to the self-limiting nature of the ALD surface reactions where it employs alternating reactant exposures of two gaseous precursors which are sequentially pulsed creating a saturated chemisorbed surface in order to achieve film growth one sub-monolayer at a time. [3, 4, 6] The sequential behavior of the precursors also helps avoid the formation of gas-phase particles that sometimes plague other gas phase deposition techniques in order to create thin, continuous, pin-hole free films which are critical to the engineering of the physical and electronic properties essential to the nano-community.

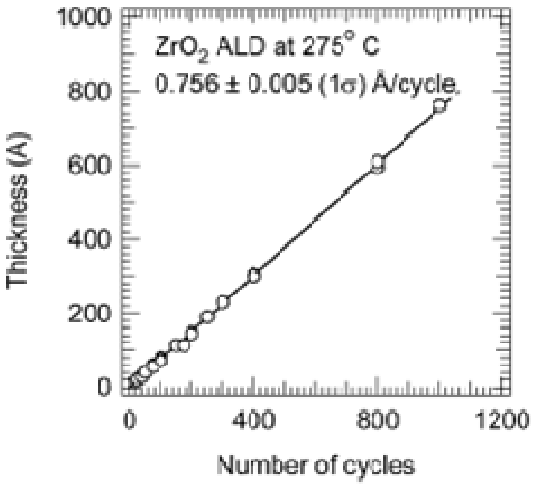


Figure 1. Linear correlation between cycle number and deposited film thickness in $ZrO_2$ ALD at 275 °C. Demonstrates the unprecedented thickness control ALD has to offer atomic layer by atomic layer.[7]

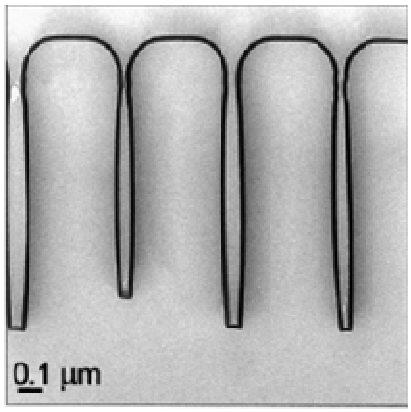


Figure 2. TEM image of 210 Å hafnium aluminate film deposited by ALD in a high aspect ratio $SiO_2$ trench.[7]

Due to its ability to deposit films with excellent uniformity and conformality over complex topographies with unprecedented thickness control, ALD has emerged as a key technology used in the down scaling of semiconductor device dimensions such as the sub-nm gate dielectrics found in transistor and high density memory devices, such as metal-insulator-metal (MIM) stacks fabricated in trench and high aspect ratio dynamic random access memory (DRAM) structures.[3, 8-14] Recently, ALD has expanded its range of applications beyond the field of conventional semiconductor technology and has pervaded in various fields, such as optoelectronics [15, 16], catalysis [17-19], energy devices [20-22], and micro-electro-mechanical systems (MEMS) [23-27]. ALD has also been a key driving force behind nanotechnology where complex 3D structures can be filled or coated to produce a wide range of nanowires [5, 28, 29], nanotubes [5, 21, 22,

29-31], and nanoparticles [32-39]. In order to support all of these advancing technologies, suitable precursors have been developed in order to deposit a wide variety of oxides, nitrides, semiconductor, and elemental materials (Table 1).[1, 4, 40]

| Oxides | Nitrides | Sulfides | Semiconductors | Elements |
|---|---|---|---|---|
| $Al_2O_3$ [4, 41-43] | TiN[21] | SrS | GaAs | Si |
| $In_2O_3$ | NbN | CaS | Si | Ge |
| $ZrO_2$ [27, 42] | TaN | BaS | InAs | Cu[37] |
| $HfO_2$ [44-47] | $Ta_3N_5$ | ZnS | InP | Mo |
| $Ta_2O_5$[48, 49] | MoN | | GaP | W[50-53] |
| $SiO_2$[31] | WN | | InGaP | Ta |
| $TiO_2$[43, 54-57] | BN | | | Ti |
| $SnO_2$[58] | | | | Pt |
| $Nb_2O_5$ | | | | Ru[39] |
| ZnO[59] | | | | Ni |
| RuO[60] | | | | Pd[38, 61] |

**Table 1. Short list of materials deposited by ALD. Puurunen listed more than 75 elements and 125 compounds that could be deposited by ALD in his 2005 review.[4]**

### 1.1.2 ALD process sequence

ALD is similar to chemical vapor deposition (CVD) in that they are both based on the chemisorption surface reactions, i.e., chemisorbed, where adsorbate species will chemically react with the atoms on the surface creating strong chemical bonds.[4] ALD differs from CVD in that precursors are sequentially introduced in a cyclic fashion to a substrate's surface rather than flown simultaneously, therefore, initiating self-limited surface reactions between a chemisorbed metal containing precursor and an adsorbed

nucleophilic reactant such as an -OH surface specie in order to deposit only one (or less than one) monolayer per cycle.[4, 7, 62] To illustrate the basic concept of the ALD process sequence, we can consider the prototypical example of $Al_2O_3$ deposition resulting from the sequential exposures of the metal precursor Trimethylaluminum ($Al(CH_3)_3$) (TMA) and water. During the first TMA half-cycle, TMA molecules are exposed to the surface and will adsorb on the active ligands present on the surface, in the case of TMA and water these are hydroxyl $–OH^*$ groups. A thermally activated reaction will occur splitting the ($Al(CH_3)_3$) molecules on the surface. The $CH_3$ ligands will combine with the hydroxyl surface groups and form a volatile organic compound, such as methane $CH_4$, which will desorb from the surface. The remaining part of the molecule chemisorbs to the surface chemically bonding the aluminum atom with either one or two oxygen atoms on the surface in order to deposit a stochiometric $Al_2O_3$ film. This reaction is referred to as a ligand exchange reaction.[4] When all the hydroxyl active sites that are physically accessible to the ($Al(CH_3)_3$) molecules then the surface is considered saturated and the half cycle is complete. Excess TMA molecules that could not react on the surface as well as desorbed reaction by-products are purged out of the reactor. For the 2nd half cycle, for this case water, water molecules will bind to the methyl groups through another ligand exchange reaction causing the release of more $CH_4$ molecules. The reaction steps can be seen in Figure 3 along with the reaction mechanisms displayed below.

*First half reaction:* $Al\text{-}(OH^*) + Al(CH_3)_3 \rightarrow Al\text{-}O\text{-}Al(CH_3)_2^* + CH_4$

*Second half reaction:* $Al\text{-}O\text{-}Al(CH_3)_2^* + H_2O \rightarrow Al\text{-}OH^* + CH_4$

*Where the asterisks denote the active surface species[63]*

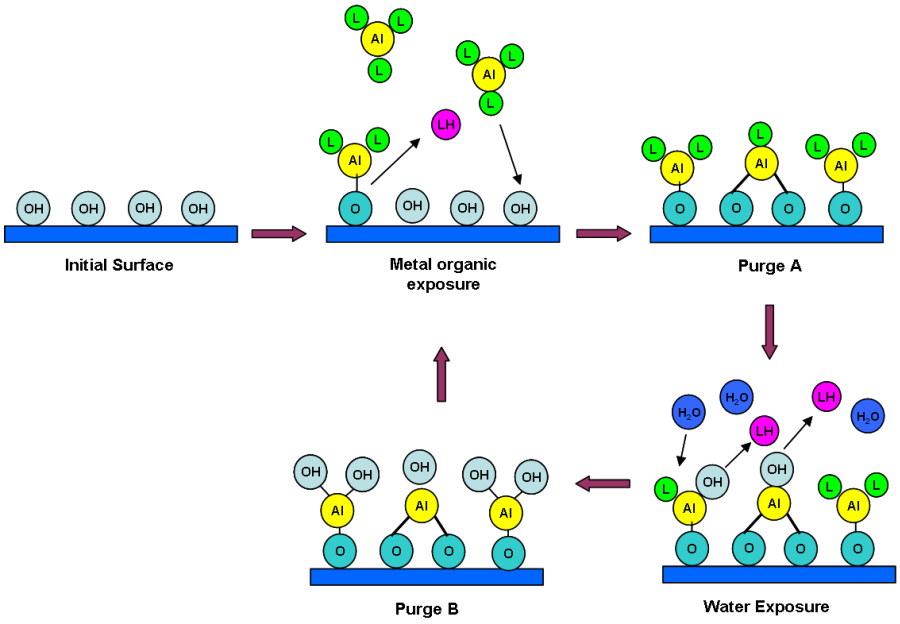


**Figure 3. Schematic of the $Al_2O_3$ ALD process sequence illustrating the four cyclic process steps of 1) metal exposure, 2) purge, 3) oxidizing exposure, and 4) purge.**

The fundamental aspect of ALD is that after the completion of the 2 half reactions, the surface is functionalized again to react with TMA, therefore depositing a new layer by repeating the cycle. This four step sequence constitutes a full reaction cycle in which a fixed amount of material is deposited, referred to as the "growth rate" (thickness/cycle).[4] Ideally, if sufficient doses are applied to saturate the surface and purge times are adequate to avoid parasitic CVD-like reactions, one monolayer of film is deposited.[58] However, most processes are limited by the steric hindrance of the metal containing precursor due to their relatively large size, therefore, blocking active surface sites from being chemisorbed by other metal precursor molecules.[4, 64] Thus, only a fraction of a monolayer (1/2ML) is actually deposited.[2] In the case of $Al_2O_3$ the growth rate is ~0.1 nm/cycle.[63]

### 1.1.3 ALD process requirements

Precise thickness control, excellent uniformity and unprecedented conformality are deemed the golden standards by which an ALD process is measured and are highly dependent upon the self-limiting behavior of the ALD process. However, a number of interdependent parameters can highly influence the performance of the process. This section will discuss only a few of the key requirements and challenges often found during ALD processing.

#### 1.1.3a Precursors

Precursor chemistry plays a vital role in order to achieve ALD.[1] Several requirements are taken into consideration when choosing a chemical precursor. (1) They must be volatile to produce a high enough vapor pressure (at least above 0.1 Torr) so they can easily be transported into the reaction zone of the process chamber. However, many precursors are low vapor liquids or even solids at room temperature and therefore require higher temperatures to raise their vapor pressure.[1, 4] (2) Precursors must be thermally stable in that they do not decompose in the source or on the substrate.[1, 4] Reactions due to the decomposition of reactants are likely to produce non-self limited reaction with higher growth rates and possible film contamination of C, H, N or halide atoms depending on the precursor used. (3) Precursors also must react rapidly and aggressively with surface groups from the previous exposure and not with its own adsorbates in order to achieve a saturated self-limiting surface in a short time (usually < 1s).[1]

Different precursors have been employed for the deposition of an oxide ALD chemistry including metal halides and several types of organometallics for the metal

containing precursor and water, $O_2$ plasma, and ozone for some of the more common oxidizers.[1, 4] Halides have been the most widely studied of all the metal containing precursors, however, their main drawback lies in the corrosive nature of the HCl by-product that is often produced causing etching of the deposited films and the encasing reactor.[1] Several organometallic precursors have been investigated including metal alkyls, amides, alkoxides, and cyclopentadienyls, however, growth rates are usually low due to the steric hindrance associated with the large ligands attached to the molecules.[1, 4]

**1.1.3b Temperature window**

ALD is a thermally activated process in order to produce self-limiting reactions on the surface of a substrate.[65] Therefore, a temperature process window can be identified based on the constant growth rate of the ALD process (Figure 4). Outside the ALD window, low temperatures are likely to exhibit low growth rates due to the fact that the reactant was unable to overcome the activation energy necessary to chemisorb on the surface. In some cases high growth rates may occur as a result of precursor condensation ultimately leading to a CVD process that can physisorb on the surface if precursors are not purged properly. This is

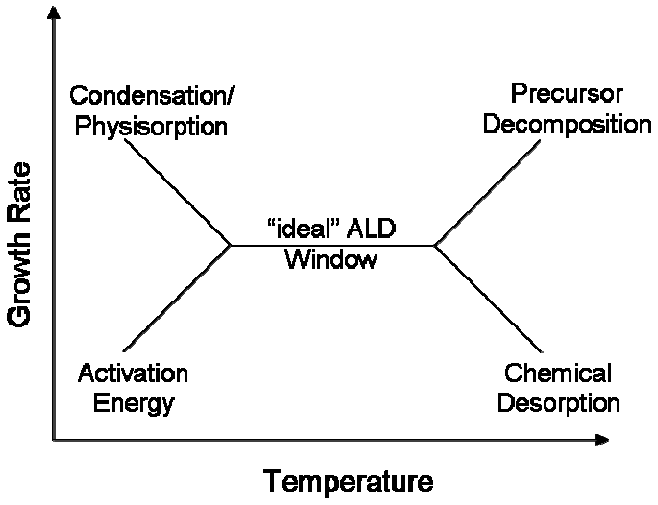


**Figure 4. Schematic of the possible behavior for the ALD growth rate versus temperature displaying the "ideal" ALD window.[63]**

particularly troubling when dealing with water, as it is a highly polar molecule that tends to stick to the surface in multilayers. However, high temperatures can lead to the decomposition of the ALD precursor or desorption of the adsorbates before they are reacted with the 2nd reactant.[4, 63]

**1.1.3c Saturating exposures**

In order to deposit uniform and conformal films across a planar surface and within a 3D nanostructure, sufficient precursor exposures and time must be supplied to fully saturate all the accessible active sites on the surface.[7, 66] The product of a precursor's partial pressure and the time it takes to fully saturate a surface (Pt) is a useful measure of the exposure dose a surface has had to the precursor,

$$Pt = S\sqrt{2\pi mkT} \qquad \text{Eq. 1}$$

Where, S is the number of molecules to saturate a surface per area, m is the molecular mass of the precursor, k is Boltzmann's constant, and T is the temperature.[66]

Determining the proper saturating dose is usually the first step in optimizing an ALD process and is achieved by incrementally increasing the dose of one precursor and

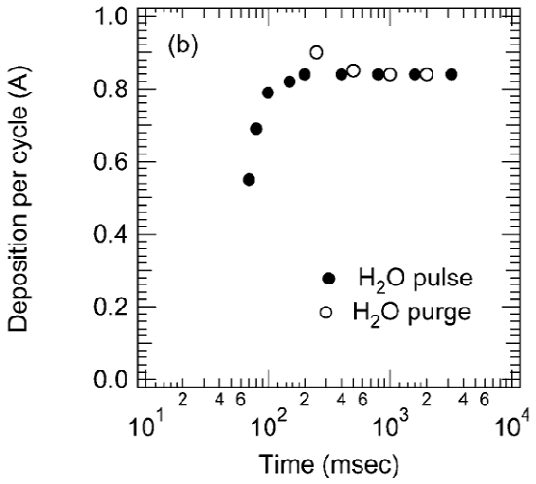


**Figure 5. $Al_2O_3$ deposition rate as a function of $H_2O$ exposure time and purge time. Saturating self-limited reactions are demonstrated by a plateau in thte growth rate once the reactant doses are at or above the saturation level. Self-limiting purge times indicate reactions are not physisorbed on the surface due to excess precursor or parasitic-CVD reactions.[7]**

measuring the growth rate. As indicated by the self-limiting nature of ALD, upon dose saturation, the growth rate will plateau designating the ALD regime as seen in Figure 5.[7] However, when depositing ALD within the confines of a high aspect ratio nanopore it becomes considerably more difficult to provide saturating exposures, not only due to an increase in surface area, but also because the reaction kinetics are now diffusion limited.[66, 67] Therefore, Gordon et al. proposed a model where the exposure dose within a high aspect ratio nanopore is a 2nd order function of the aspect ratio, a, and require longer exposure times to completely saturate the surface.[66]

$$Pt = S\sqrt{2\pi mkT}\,(1 + \frac{19}{4}a + \frac{3}{2}a^2) \qquad \text{Eq. 2}$$

Optimizing the exposure dose is important in that over-dosing a precursor will require longer purge times and waste expensive precursor, while under-dosing can lead to thickness gradients and lower growth rates across a surface.[68]

### 1.1.3e Purge window

Purge time is a critical component of the ALD cycle sequence. Insufficient purge times to fully exhaust any unreacted precursor or subsequent by-products can result in an overlap of the two ALD precursors, i.e. simultaneous presence of both precursors, thus allowing the ALD process to transition to a CVD mode.[6] Similar to the temperature window, a purge window can be created as well (Figure 6). If a CVD mode ensues upstream to the reaction zone, the reactants are likely to result in gas phase reactions and subsequently lower growth rates. However, if the temperature is too low, multilayer adsorption (physisorborption) can occur in which the excess reactants will react with the next precursor pulse resulting in higher growth rates on the surface. Water is particularly prone to this behavior due to its polarity and natural "sticky" behavior requiring longer purge times.[68] However, when purges are too long, desorption and thermal decomposition of the adsorbed species can take place leading to possible film contamination or compositional changes in the film. Figure 5 demonstrates the self-limiting behavior of the ALD process when purge times were incrementally increased by measuring film growth rates to determine growth was not in a CVD mode.

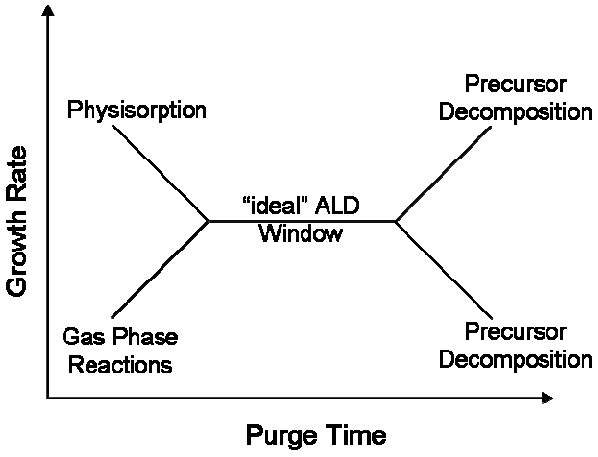


**Figure 6. Schematic of the deposition rate as a function of purge time. The figure displays the potential behaviors found in ALD.**

### 1.1.3d Pressure regime

Maintaining atomic level thickness control with wafer scale uniformity and conformality within high aspect ratio nanopores is dependent upon the complex reaction dynamics associated with chemisorbed reactions found in different flow regimes. An important issue of the ALD process is the distinction between self-limiting and saturation. The self-limiting behavior of ALD asserts that a reactant in the gas phase can only chemisorb with complementary active surface species and not with its own adsorbates or by-products, thus guaranteeing that the reaction will be self-limited.[4] However, chemisorption is a localized reaction affected by the surface energy and repulsion between neighboring adsorbates, therefore only allowing certain positions on the surface to bind with a molecule.[64] This means that upon extended pulse times, the reaction doesn't necessarily terminate because all the active sites have been consumed. However, reaction saturation occurs when an equilibrium between desorption of excessive precursor and adsorption of further species is reached for a given temperature and pressure. Therefore, if all the active surface sites have been occupied by chemisorbed species, then increasing the partial pressure of a reactant should have no effect.[4]

The process pressure within a system is directly related to the surface residence time of a precursor. Li et al. demonstrated the impact of process pressure on film growth rates and wafer uniformity and high aspect ratio conformality (i.e., step coverage) in an $Al_2O_3$ ALD process when using $Al(CH_3)_3$ and $O_3$. As seen in Figure 7a, the across wafer uniformity is compromised as a function of decreased reactor pressure; however, uniformity was restored by increasing the process temperature. Similarly, Figure 7b

illustrates a decrease in conformality within a nanopore with an aspect ratio of 13 when the process pressures become too low. The authors suggested the increase in growth rates at higher pressures was attributed to the change in surface saturation levels, the enhancement of precursor diffusion, as well as the higher probability for surface reaction to occur at the active sites.[65] Both of these cases demonstrate that the rate limiting step within a viscous flow regime (Knudsen number, Kn, < 0.01), meaning the velocity and surface irregularities are small enough for a gas to flow gently around obstructions in a laminar streamline, is the surface reaction kinetics.[69]

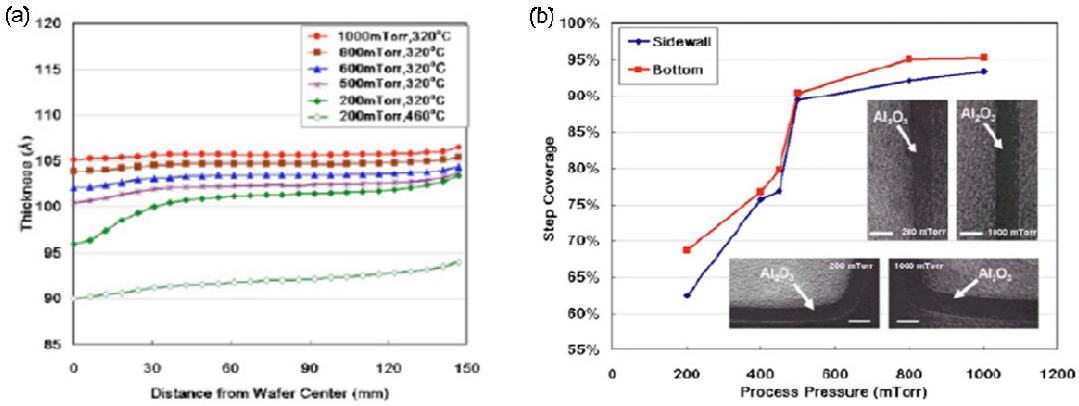


**Figure 7. Influence of the process pressures found in a laminar viscous flow regime on (a) across wafer uniformity and growth rates, as well as (b) conformality with in a high aspect ratio nanostructure.[65]**

When the flow regime transitions to a molecular flow regime (Kn > 1) often associated with ultra-high aspect ratio nanopores where the mean free path of a precursor is equal to or greater than the nanopore diameter, the deposition kinetics become subject to the Knudsen diffusion of the precursor.[69] The idea in Knudsen diffusion is that a molecule will ballistically transport its way down the length of the pore and interact with the pore wall before it interacts with another molecule. Once the molecule hits the wall it

can either chemisorb to the surface or it can deflect off changing its course of trajectory and probably a losing some kinetic energy.[69] Therefore, when in a molecular flow regime the rate limiting step is the Knudsen diffusion and will require not only longer surface residence times of a molecule to diffuse down a nanopore, but will require longer purge times for unreacted precursor and by-products to diffuse out.[66]

## 1.3 Porous Anodic Alumina (PAA)

Aluminum naturally has a highly resistant coating of oxide along its surface and the enhancement of this oxide to produce a porous anodic oxide film has garnered a lot of interest in self-assembled nanotechnology. PAA membranes are hexagonally ordered, self-aligned cylindrical nanopores formed by the controlled electrochemical oxidation or anodization of aluminum metal in certain electrolytic forming solutions.[44, 70-72] Depending on the type of electrolytic solution used different film growth mechanisms occur. Anodization in neutral pH solutions, such as neutral boric acid solution, ammonium borate, or a tartrate aqueous solutions, produce completely insoluble non-porous barrier anodic alumina (BAA) membranes; whereas, slightly acidic solutions, such as phosphoric, oxalic, or sulfuric acids will produce a slightly soluble porous anodic alumina (PAA) membrane.[70, 71] These two types of films differ in how thick one can be produced and their controlling parameters. When aluminum is anodized at a constant voltage held below the oxide breakdown voltage in a neutral pH solution, the native barrier oxide film is thickened at a constant rate of 1.4 nm $V^{-1}$, therefore, forming a protective BAA membrane ~1,000 nm thick.[70] However, the thicknesses of a PAA membrane is time dependent and can grow many times thicker than the upper limit

placed upon BAA films.

PAA is a balance between field-assisted chemical dissolution at the electrolyte/oxide interface and the oxide formation at the oxide/metal interface. A BAA layer forms when the Al metal surface reacts with $O_2^-$ and $OH^-$ ions at the anode allowing the anions to diffuse into the oxide layer and continuously react with the metal beneath. Field-assisted migration moves $Al^{3+}$ ions from the oxide/metal interface to the oxide/electrolyte interface, where Al-O bonds stretch under the high electric fields. This leads to the dissolution of $Al^{3+}$ ions at the oxide/electrolyte interface, a process aided by Joule heating due to the high fields at the pore tips. The balance of the field-assisted and chemical dissolution at the electrolyte/oxide interface and the continual diffusion of free $O_2^-$ ions across the oxide layer reacting with the Al metal at the oxide/metal interface results in the formation of porous alumina membranes which can continually grow as long as conditions remain the same.[70, 71]

The unique behavior of PAA to self-order in to a hexagonal array of parallel nanopores is highly dependent upon the anodization conditions.[72] Three types of electrolytic acid solutions with associated voltages have been identified to lead to optimum self-ordering of the PAA membrane: 2.7 wt% aqueous oxalic acid at 40 V, 20 wt% aqueous sulfuric acid at 19 V, and 10 wt% phosphoric acid at 160 V.[73, 74] All three acids lead to a hexagonal arrangement of the pores, but each provides a unique interpore spacing, $D_{int}$, and pore diameter, $D_{dia}$ (Figure 8a), which are linearly proportional to the anodizing potential.[70, 73] It has been experimentally determined that the interpore spacings for sulfuric (~ 25 V), oxalic (~ 40 V), and phosphoric (~

200V) are 66.3 nm, 105 nm, and 501 nm, respectively, while pore diameters were determine to be 24 nm, 31 nm, and 158 nm, respectively.[73, 74] Therefore, as the anodizing voltage increases, the oxide cell increases and consequently the pore density will decrease.[70] Figure 8b-c displays SEM images of a PAA template anodized in 0.3M of aqueous oxalic acid anodized at 40 V and 8 °C. Figure 8b illustrates the top down honeycomb structure while Figure 8c exhibits the straight, parallel nanopores of the PAA membrane aligned orthogonally to the underlying aluminum substrate.

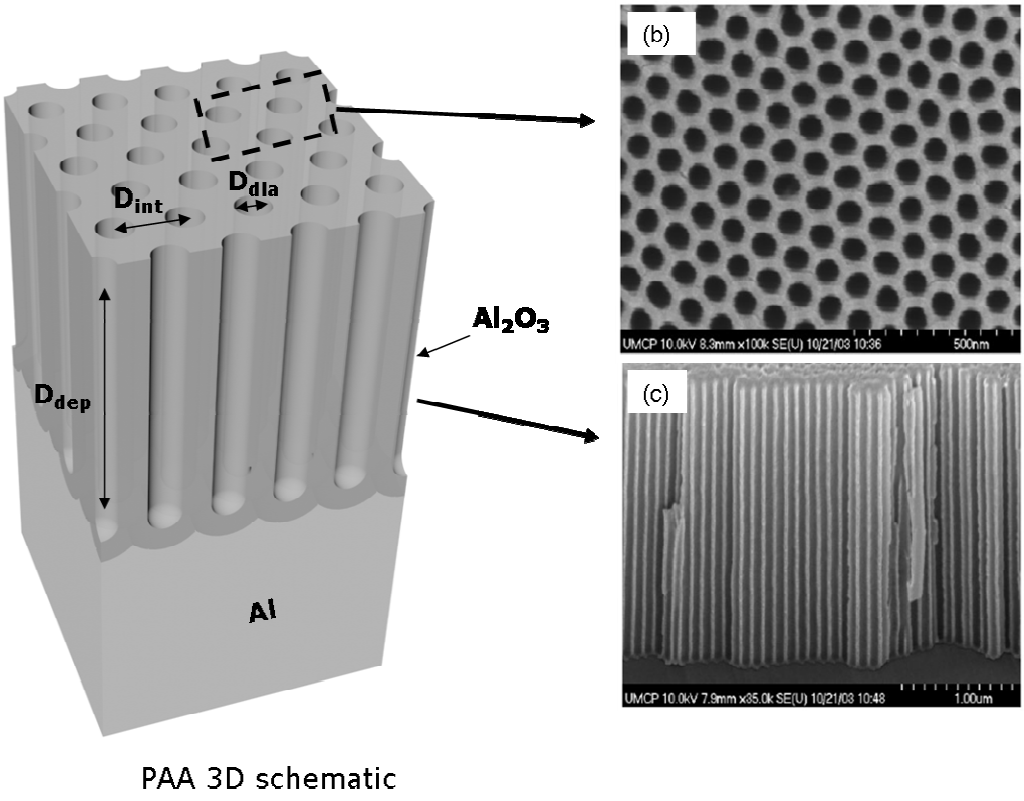


**Figure 8. PAA formed in 0.3M of oxalic acid at 40V, (a) PAA 3D Shcematic with labeled metrics, (b) Top down SEM displaying honeycomb structure and (c) cross-sectional view demonstrating straight, parallel nanopores adhered to an underlying aluminum substrate.[44]**

## 1.4 Motivation and Objectives

As device designs head towards the nanoscale, conventional ULSI technology is reaching its limits to pattern and access such small device dimensions seen in technology today. Therefore, a strong driving force behind nanotechnology is the combination of self-limiting processes with nature's ability to self-assemble. Atomic layer deposition is proving to be a powerful self-limiting technique to deposit extremely thin films with excellent uniformity and unprecedented conformality even over the most demanding nanotopographies. The nature of PAA to self-align and self-order in order to create a highly dense, parallel porous membrane over large surface areas has rendered it a useful material for nano-templating applications and device platform applications.

Energy storage is one such area that has benefited from the combination of ALD and PAA. Figure 9 demonstrates a Ragone plot displaying the state of energy storage technologies found today in terms of power density and energy density. Ideally, energy storage technologies should have a high energy density (capacity to store charge) as well as boast high power densities (rapid charge/discharge rates). Current battery technology has reasonably good energy density but lacks the power density due to its dependence on bulk ionic movement and chemical reactions to charge and discharge. Recent work on Lithium ion superbatteries have shown that coupling nanostructures and the materials science of the bulk material can lead to a high power density.[75] Electrochemical capacitors store charge by creating a double layer of ionic charge close to the surface of an electrode, therefore requiring high surface area electrodes.[76] Nanostructures with high surface areas have provided electrochemical capacitors with increased energy

densities, as well as maintaining high power density common to this technology.[77] Similar to electrochemical capacitors, electrostatic capacitors are dependent upon high surface areas in order to achieve high energy densities. Electrostatic capacitors make use of a thin dielectric material between two metal electrodes in order to store charge, and are therefore not limited by electrochemical reactions or ionic conduction to release or carry a charge.[76] However, electrostatic capacitors lack the energy density to make them a viable technology as compared to electrochemical capacitors and batteries.

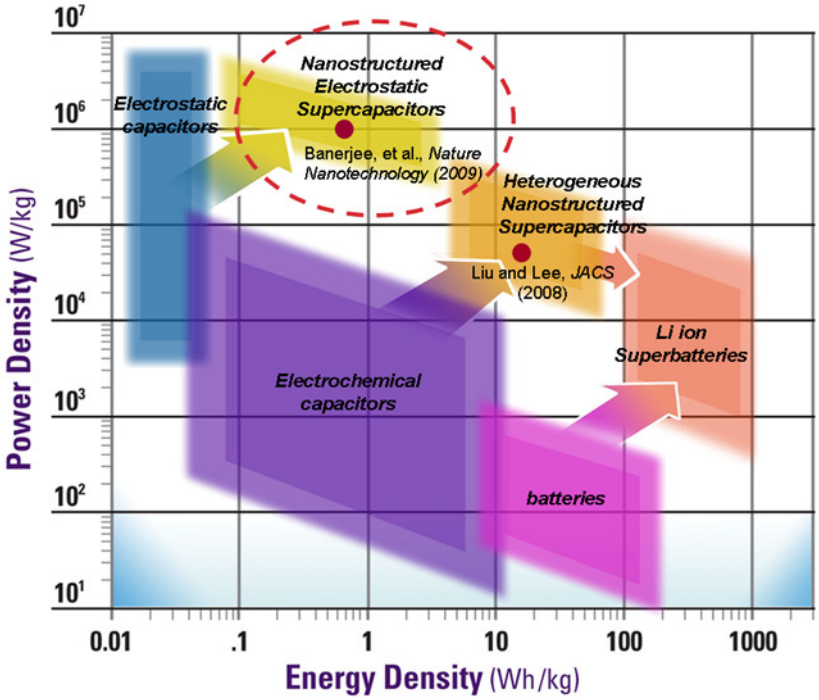


**Figure 9. Ragone plot detailing the state of energy storage technologies by contrasting their power density versus energy density.**

Recently our group has demonstrated an operational metal-insulating-metal (MIM) electrostatic nanocapacitors fabricated out of multilayer ALD thin films within the confines of an ultra-high aspect ratio PAA membrane. Using $Al_2O_3$ as a high-k

dielectric ($\varepsilon_\kappa$ ~9) we have demonstrated equivalent planar capacitances of up to 100 $\mu F/cm^2$ within a 10 μm deep nanopore.[21] It is believed through the use of even higher-k materials, such as $HfO_2$ ($\varepsilon_k$ ~14) and $TiO_2$ ($\varepsilon_\kappa$ ~80), as well as the use of higher aspect ratio nanopores, higher capacitance values can be achieved.

While the favorable nature of ALD to be self-limiting and saturating to provide exceptional coatings of thin films across planar wafers and in ultra-high aspect ratio nanosturctures, the reaction dynamics associated with different flow regimes, chemisorbed reactions, and interfering surface topographies can be quite complex. This is particularly true for the type of precursors used in ALD (organometallics, halides, water, and ozone) which can produce deviations from the "ideal" monolayer self-limiting behavior due to multilayer physisorption, steric hindrance, secondary reactions, and parasitic CVD reactions. Therefore, it is important to identify the process parameters that constitute an ALD process window, where the benefits of ALD are realized. Therefore, the objective of this work is to gain insight on the growth behavior of ALD uniformity across 2D planar wafers in relation to ALD conformality within an ultra-high aspect ratio nanopore.

In order to understand the relationship between the 2D and 3D scale, we first investigate ALD's ability to conformally coat a complex topography found in the viscous flow regime. We employ the nano-roughened surface topography of a stripped 1$^{st}$ anodized PAA surface in order to observe the influence the underlying topography will exhibit on the resulting ALD surface profiles as deposition conformally coats the surface. We employ a commercial ALD reactor in order to deposit conformal $TiO_2$ ALD films

using Tetrakis(dimethylamino) titanium (TDMAT) and water. It is imperative to understand the progression of ALD surface profiles in order to know the benefits or disadvantages of ALD to modify sharp surface structures. This is of particular importance to us because PAA membranes are plagued with sharp surface asperities that result in localized electric fields and low field breakdown in our MIM capacitor technology.

Of further interest, is the investigation of deposition mechanisms when transitioning from a 2D planar wafer into that of a 3D ultra-high aspect ratio nanopore. ALD is based upon a sequence of self-limiting and saturating behavior that often relies upon interdependent process parameters such as reactant dose, surface residence time, and purge times for specific precursors used. When a nanopore is introduced into the substrate, the surface area is increased, resulting in the need for more precursor molecules to completely saturate a surface. However, an increase in molecules does not necessarily result in conformal films down the length of a nanopore. The molecules also need time to diffuse down (surface residence time) and back up (purge time) the length of the nanopore. Therefore, it is imperative to study the relationship between various process parameters in different flow regimes, as it will be of great importance to the optimization of the ALD process in order to create uniform and conformal films. For the purpose of this work we employ a custom-built ultra-high vacuum (UHV) ALD system to deposit the high-k dielectric material $TiO_2$ using the precursors TTIP and ozone. As a means to characterize these structures, we propose a novel method to extract film thicknesses from energy dispersive spectroscopy (EDS) line scans and a cylindrical assumption.

## 1.5 Organization of the thesis

This thesis consists of six chapters in addition to the first Introduction chapter. The summary of each chapter is given below.

**Chapter 2:** This chapter reviews experimental setups that were implemented to carry out this research. It primarily focuses on the design of two ALD reactors, one custom built and one commercial, the nano-template synthesis process of the PAA templates, and a variety of ex-situ characterization techniques used to characterize the ALD thin films.

**Chapter 3:** This chapter focuses on the influence a nano-roughened topography can induce on ALD surface profiles during continual deposition and illuminate the use of ALD to modify surface structures with sharp asperities.

**Chapter 4:** This chapter focuses on the growth behavior of $TiO_2$ ALD across planar surfaces when using titanium tetraisopropoxide (TTIP) and ozone as the metal and oxidizing precursors. This chapter will emphasize the critical role a precursor's surface residence time can have on the resulting chemistry's growth rate and uniformity.

**Chapter 5:** This chapter focuses on a methodology to extract thin film thicknesses when deposited in an ultra-high aspect ratio nanopore. It proposes the use of energy dispersive spectroscopy (EDS) line scans to infer film thickness through a cylindrical assumption.

**Chapter 6:** This chapter focuses on the influence of complex interdependent ALD process parameters such as precursor dose, surface residence time and purge on the conformality of ALD thin films within 3D ultra-high aspect ratio nanopores versus the

uniform growth behavior across a 2D planar surface when using TTIP and ozone as precursors.

**Chapter 7:** This thesis is concluded with a summary of the contributions of this work and some thoughts regarding the future of this work.

# Chapter 2 : Experimental Setup

The following chapter focuses on the tools and materials that were implemented in order to carry out the proposed research. Two ALD reactors were used in this study, the first being a custom built ultra-high vacuum (UHV) ALD reactor. It was designed in 2003 and built by Dr. Wei Lei and Dr. Laurent Henn-Lecordier, two prior doctoral students. The tool was originally designed to investigate the use of mass-spectrometry in W ALD processing for in-situ sensing and real-time wafer-state metrology.[52, 78] After the completion of this work, a funded collaboration with the equipment supplier MKS Instruments was initiated to investigate new venues for ALD process optimization. The tool was upgraded with an abundance of donated equipment, including an $O_3$mega ™ ozone generator, a MKS Vision 1000C mass-spectrometer, and a liquid injection system for low vapor pressure precursors (not used in this work). Additionally a new delivery system was built to accommodate low vapor pressure precursors whose mode of delivery was very different than the W ALD precursors, tungsten hexafluoride and silane, which are both gases above atmospheric pressure at room temperature.

A commercial Beneq TFS 500 hot wall ALD reactor was purchased and installed in the Maryland Nanocenter's FabLab facilities in 2008. Designed to be the work horse for the Nanocenter's ALD thin film needs, the tool was originally configured to deposit such films as $Al_2O_3$, $HfO_2$, $TiO_2$, ZnO, and TiN. The tool allowed users to rapidly deposit ultra thin films over planar and nanoscale topography with relative ease.

In order to facilitate quantitative evaluation of ALD conformality in very high

aspect ratio nanopores, a nanoporous template that was easily produced and compatible with high resolution metrology of ALD film profiles was required. Therefore, custom made porous anodic alumina membranes were used as a versatile and easy platform to investigate the influence of key process parameters on the conformality of titanium dioxide ($TiO_2$) ALD thin films in an ultra-high aspect ratio nanopore.

Being able to easily characterize the ALD films deposited was essential to evaluating and rapidly optimizing the ALD process performances at the 2D wafer and 3D nanopore scales. A Sopra GES5 spectroscopic ellipsometer was acquired to provide maps of thicknesses and optical properties across the 2D wafer on a run-to-run basis. Through the use of the Maryland Nanocenter's NISPLab, a Hitachi SU-70 high resolution scanning electron microscope (SEM) equipped with a Bruker energy dispersive spectrometer (EDS) and a JEOL 2100F Field Emission transmission electron microscope equipped with an Oxford EDS were both readily available in order to image samples and determine film composition and thicknesses. A MFP-3D atomic force microscope was easily accessible through Dr. Seog's lab in order to map ALD surface profiles across a roughened sample.

## 2.1 ALD Systems

### 2.1.1 UHV-ALD Reactor

#### 2.1.1a Reactor design

A custom-built ultra-high vacuum (UHV) stainless steel ALD reactor was used in this study (Figure 10a). The system consists of two 8”-diameter 6-way stainless steel conflate (CF) chambers employed as a load-lock and ALD process chambers. A small 50 L/s turbomolecular pump (TMP) is used to pump down the load-lock from atmospheric pressure (760 Torr) to pressures below 1E-5 Torr within 5 minutes. The load-lock is imperative for rapid wafer throughput by limiting exposure of the main process chamber to atmosphere while minimizing potential surface contamination of the ALD reactor environment and wall memory effects during wafer loading and unloading. In order to minimize the amount of water physisorbed on the stainless steel walls of the ALD process chamber, heating tapes were used to maintain a temperature of 150 °C while a Pfeiffer TPU261 turbomolecular pump (TMP) with a pumping speed of 260 L/s provided a base pressure below 1E-8 Torr with no gas load present.

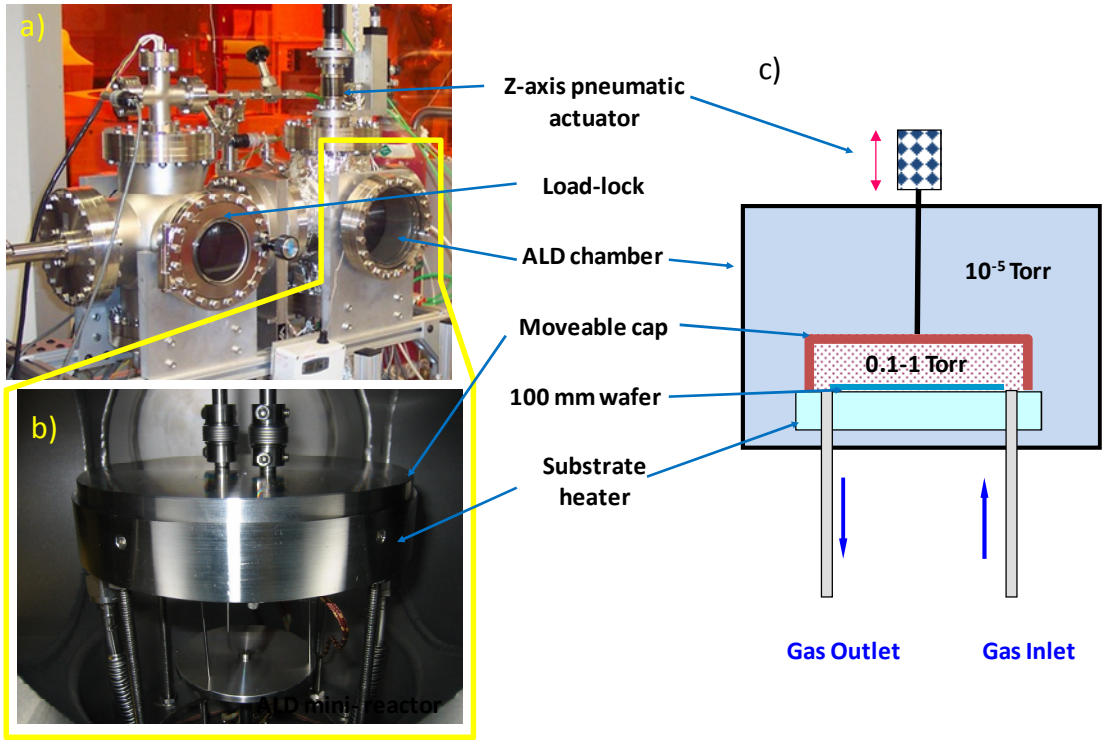


**Figure 10. Custom built UHV ALD reactor – a) ALD platform with load-lock and ALD chamber. b) Embedded mini ALD reactor in UHV chamber with cap in the down position. c) Schematic of ALD chamber.**

Due to the digital process sequence of ALD, fast cycle times of reactant gases with sufficient purge times are critical to avoid parasitic CVD-like reactions. Therefore the large volume of the process chamber, ~16 liters, makes fast cycling times of reactant gases rather difficult and would require extremely long purge times and high temperatures to suffice desorption of reactive species out of the chamber and off the walls. Therefore, a smaller mini-reactor was embedded in the main UHV process chamber as seen in Figure 10b. The volume of the mini-reactor measured 0.2 liters, therefore allowing rapid gas exchange during ALD exposures and shorter purge times. Compared to the large scale process reactor, the use of a mini-reactor allowed for shorter

residence times ~1 sec and minimized the ratio of wall to wafer surface areas to about 3 to 1 making it a suitable environment for in-situ process sensing at the wafer scale using mass-spectrometry, as well as, minimizing chamber "memory effects" often associated with adsorption/desorption phenomena.[52, 68, 78]

The mini-reactor features a pneumatically actuated stainless steel cap that is lowered and raised in order to easily transfer 100 mm wafers from the load-lock onto the substrate heater. When the cap is in the down position, a rough vacuum seal is provided between the mini-reactor and the main chamber; therefore, creating a pressure differential respectively from ~0.1 - 1 Torr to 1E-5 – 1E-4 Torr depending on the gas load applied (Figure 10c).

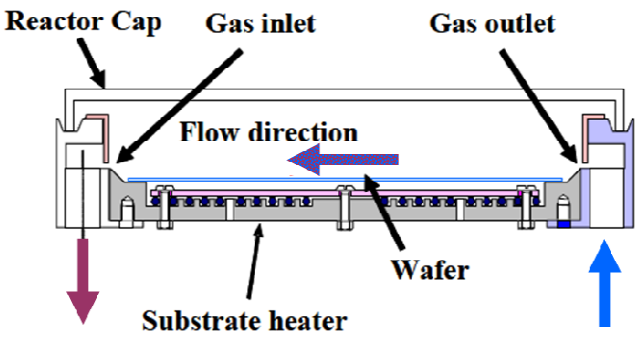


**Figure 11 – Cross-section of mini-reactor demonstrating gas flow direction.**

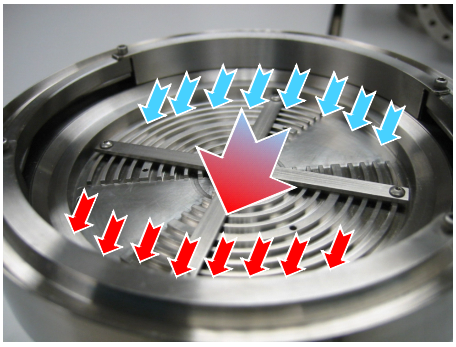

**Figure 12 – View of the 100 mm diameter substrate heater with visualization of flows across the wafer.**

The mini-reactor consists of a custom designed 100 mm stainless steel substrate heater. The base of the heater was integrated with ¼" diameter tubing that operated as gas inlet and exhaust outlet lines. Process gases were introduced and exhausted through two 1 mm wide by 100 mm long, diametrically opposing slits positioned 3mm above the

wafer as seen in Figure 11. Figure 12 shows a top down view of the 100 mm substrate heater demonstrating the cross-flow direction of gases across a wafer. An MKS Instruments capacitance monometer pressure gauge was integrated in the downstream exhaust line in order to provide the pressure reading for the mini-reactor. The operating pressure within the mini-reactor was held around 130 mTorr while the gases where exhausted to a 20 $ft^3$/min mechanical roughing pump. Under these conditions a viscous, laminar flow was achieved within the mini-reactor and across the wafer.

The temperature of the substrate heating coil is regulated by a proportional integral derivative (PID) control loop based on the feedback of a thermocouple attached on the underside of the heater. A 100 mm 13-point SensArray$^{TM}$ thermocouple wafer was used to calibrate the substrate temperature (Appendix I, Figure a). At 250 °C and 0.1 Torr the temperature non-uniformity was measured to be less than 5% across the wafer determined by the standard deviation divided by the average temperature ($\sigma/\mu$). It was critical to calibrate the actual substrate temperature as a function of the PID control temperature as pressure and the outer UHV chamber temperature will significantly impact the thermal coupling between the heater and the wafer. The mini-reactor is considered an isothermal environment meaning the outer UHV chamber has significant effect on the substrate temperature which creates a significant offset from the PID controller setpoint temperature and the actual substrate temperature (Appendix I, Figure b, c). Therefore, all temperatures hereafter refer to the estimated actual wafer temperature. The cap is only conductively heated through contact with the substrate heater and therefore is about 20 °C lower than the heater temperature and was subject to deposition as well.

### 2.1.1b Gas delivery and reactant dose control

Liquid titanium tetraisopropoxide ($Ti[OCH(CH_3)_2]_4$) (TTIP) was used as the titanium metal precursor. A 20mL stainless steel reservoir containing 5g of liquid TTIP was heated using heating tapes connected to a PID temperature controller. The source was maintained at 58 $^oC$ in order to achieve a vapor pressure of ~0.6 Torr (Appendix II). In order to achieve reproducible doses of the TTIP precursor, fast action pneumatic ALD valves were implemented on the inlet and outlet of a temperature-controlled 20 mL volume monitored by a 0-100 Torr capacitance manometer pressure gauge (Figure 13). TTIP doses were controlled by timing the opening of these valves. The inlet valve to the volume was opened for 1 s in order to fill the volume to the vapor pressure of the TTIP precursor. Upon reaching the given time setpoint, the inlet valve between the precursor source and the volume was closed and the gases were released into the chamber for 0.3 s. This time was deemed adequate to completely empty the 20 mL volume of TTIP, with the exception of some adsorption on the walls. By monitoring the minimum and maximum pressures during each cycle, the doses were approximated from the ideal gas law, $pV=nkT$ (where p is the pressure, V the volume, n the number of μmols, k the Boltzmann's constant, and T the absolute temperature). A 0.47 μmol dose of TTIP was deemed sufficient to achieve full saturation across a Si wafer within the reactor chamber.

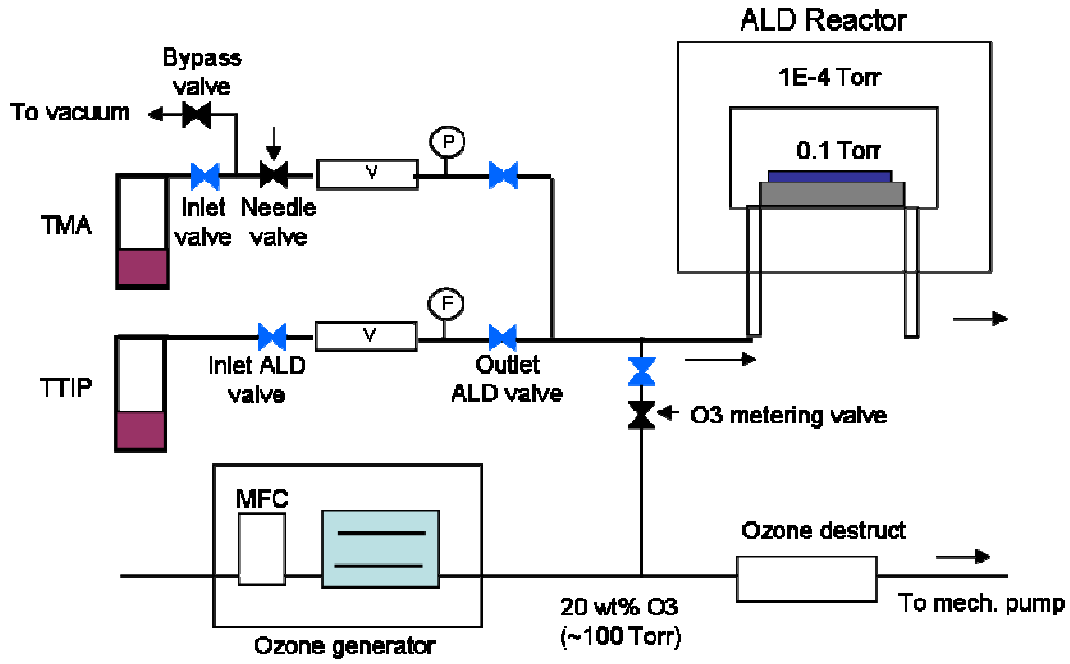


**Figure 13. Schematic of gas delivery setup. TTIP is introduced in volume V for 1 sec and the released through the outlet ALD valve. Description of TMA delivery line can be found in Appendix III.**

Ozone was obtained by flowing 200 sccm of $O_2$ (Grade 5, Praxair) into an MKS Instruments $O_3$mega ozone generator. The flow produced a 20psig pressure in the single electrical discharge cell. At 100% power, the ozone concentration at the outlet was up to 20 wt% (300 g/m$^3$) with the balance being $O_2$. Due to the high flow and high pressure required for the operation of the $O_3$mega$^{TM}$ a different control scheme of the ozone exposure was necessary. The $O_2/O_3$ mixture was flowed continuously into an HA-series catalytic ozone destruct from Ozone Engineering to deactivate ozone into oxygen. Therefore, only a fraction of the total flow was pulsed into the reactor using a Swagelok medium flow metering valve in series with a fast action pneumatic ALD valve (Figure 13). For a given needle valve conductance, the number of μmols of ozone was

determined by integrating the pressure peaks measured in the mini-reactor for different exposure times and comparing them to integrated peaks from known doses determined through pressure measurements in an attached trimethylaluminum (TMA) vessel (Appendix IV).

#### 2.1.1c Process Control

An automated PC-based control platform created by National Instruments LabView™ was used to accurately control the valve sequences during precursor exposures and purges, as well as monitor pressure signals in the precursor fill volumes and reactor. Recipes were created in an excel spreadsheet and uploaded to the platform in order to define process setpoints for each precursor, the sequence of exposures and purges, as well as the number of total cycles the process consist of.

### 2.1.2 Beneq ALD Reactor

#### 2.1.2a Reactor design

A commercial TFS 500 cross flow reactor from Beneq was used for part of this study. The reactor features a cold wall vacuum chamber with a constant nitrogen flow of 100 sccm creating a base pressure of ~7 Torr. Embedded within the vacuum chamber is a mini hot-walled furnace reaction chamber with a base pressure of ~1 Torr (Figure 14). The outer vacuum chamber is pumped down through the reaction chamber creating a pressure differential creating a sealing flow ensuring that all reactions occur within the reaction chamber and over the sample. The mini-reactor also decreases the wall to wafer surface ratio helping to restrict reactions to the wafer surface. Samples are loaded through a large chamber door, where the cap of the mini-reactor is removed by simply

lifting using an improve lever due to heat (similar to removing the lid to a pot on a stove). The system uses a water cooling system in order to keep the outer vacuum chamber's walls cold while serpentine IR heaters surround the inner vacuum chamber radiating heat to the mini-reactor chamber. Therefore, the mini-reactor and subsequent substrate within is heated by both radiation and conduction. The reaction chamber utilized a cross-flow design, introducing and exhausting process gases through two diametrically opposing holes. Gases then pass through an equally spaced porous grate allowing flow to be equally distributed over the wafer.

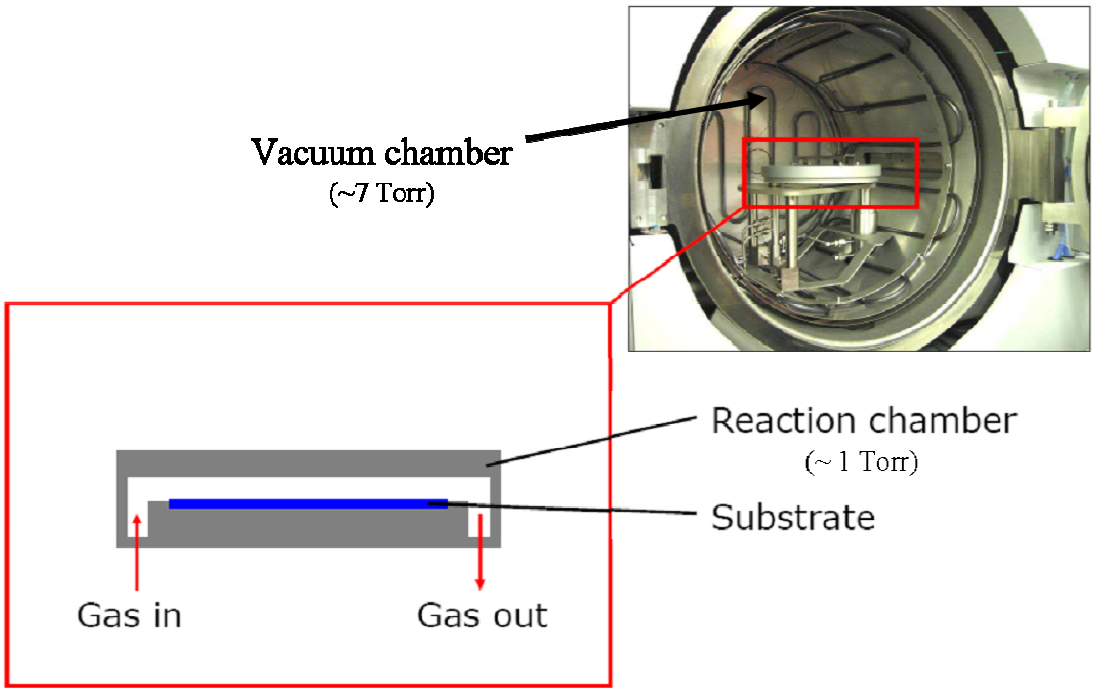


**Figure 14. Commercial Beneq ALD reactor – (a) Cold wall vacuum chamber with serpentine IR heaters surrounding an embedded mini ALD reaction chamber (b) the mini ALD reaction chamber demonstrating the cross-flow direction of gaseous precursors.**

#### 2.1.2b Gas delivery and reactant dose control

Liquid tetrakis(dimethylamino) titanium ( $Ti[N(CH_4)_2]_4$, TDMAT) was used as the titanium metal precursor. A 200 mL stainless steel bubbler containing 20g of liquid TDMAT was heated in the Beneq hot source HS200 compartment. The source was maintained at 60 °C in order to achieve a vapor pressure of ~1 Torr (Appendix II). Pulses of TDMAT were created by pulsing 100 sccm of nitrogen through the headspace of the TDAMT container (not a true bubbler system) and were introduced into the reaction chamber by leaving a high temperature ALD valve open for a set amount of time. The downside to this pseudo-bubbler approach is that the amount of precursor is limited by the vapor pressure of the precursor. If higher doses are required the set temperature on the source needs to be raised, which could be dangerous if heading towards the decomposition temperature. The decomposition temperature of TDMAT is approximately 90 °C. Water was used as the oxidizing precursor. A 200 mL stainless steel bubbler containg DI water was maintained at room temperature. Due to water's high vapor pressure (Appendix II), pulses were timed using an pneumatically actuated 3-way valve in order to determine complete purging of the lines after pulsing.

## 2.2 Porous Anodic Alumina Templates

### 2.2.1 Electropolished aluminum

Aluminum foils of high purity (99.99% or better) were cut to size, rinsed with acetone and electropolished in order to remove any particles and micro-roughness from the surface that can greatly influence the quality and growth of the final pores. Foils

were placed in a 1:5 perchloric acid and ethanol bath held at ~3 °C. In order to keep the bath cool during electropolishing a jacket beaker connected to a circulator pump was used. A mixture of 1:1 ethylene glycol and water was circulated through the jacketed portion of the beaker helping to maintain the ~3 °C necessary to keep the aluminum foil from burning due to the Joule heating during electropolishing. It was important to maintain a constant stir rate within the bath solution in order to help dissipate accumulating heat as well as help keep an even perchloric acid concentration throughout the solution.

A sheet of either aluminum or stainless steel with larger surface area than the sample was placed in the bath to act as the cathode, i.e. negative electrode, where the cut aluminum sample is the anode, i.e. positive electrode. Samples were electropolished for 5 minutes and the aluminum surface has a mirror like finish. Mirror like finishes were unattainable if perchloric solutions started at temperatures higher than 5 °C, however processes starting below 5 °C and raised to ~ 10 °C could still be attained.

### 2.2.2 Two-step anodization procedure

A two-step anodization procedure first reported by Masuda et al was used to create ultra-high aspect ratio porous anodic alumina membranes.[79] Electropolished aluminum samples were placed in a bath of oxalic acid (0.3 M in deionized (DI) water) within a similar circulator jacket setup as the electropolishing setup. The oxalic solution was cooled to ~8 °C and constantly stirred in order to encourage even etching of the alumina surface. Using an aluminum sheet as the cathode and the electropolished aluminum sample as the anode, samples were anodized for ~7 hrs at 40 V. After samples

reached an optimum pore ordering, they were stripped of the anodic oxide formed during the 1st anodization in an aqueous mixture of phosphoric acid (6 wt%) and chromic acid (1.8 wt%) at 60 °C. The stripped PAA surface left an ordered pre-textured aluminum surface at which a second anodization of the aluminum could commence. The second anodization took place under the same conditions as the first, producing well ordered parallel nanopores that were perpendicular to the aluminum substrate underneath. The pore depth was a function of the 2nd anodization timing using a pore growth rate of ~73 nm/min. After the desired pore depth was achieved, pores were widened in a 0.1 M aqueous solution of phosphoric acid at 38 °C. The pore widening etch rate of the PAA under these conditions was ~0.79 nm/min. The amount a pore can be widened is limited by the interpore spacing of the PAA membrane, roughly 105 nm for a template made in oxalic acid. Therefore, pores with an initial diameter of ~35 nm can only be widened to a maximum of ~90 nm.

## 2.3 Spectroscopic Ellipsometry

### 2.3.1 Operational Principles

Film thickness is one of the most important parameters for the application of thin films in devices.[80] Due to ALD's self-limiting properties film thickness can be precisely controlled by the number of ALD cycles and the growth rate per cycle can be determined from the change in film thickness with the number of cycles. The film thickness as a function of ALD cycles is determined by ex-situ spectroscopic ellipsometry. Spectroscopic ellipsometry provides a fast, non-destructive and accurate

method to measure film thicknesses and optical properties ranging from sub-nanometers to a few microns. In addition it can also be used to characterize composition, crystallinity, roughness, doping concentration, and other material properties associated with a change in optical response.

Ellipsometry works by measuring the change in linear polarization as light reflects from a surface and basically consists of a light source and a detector unit.[80-82] A broad spectral range light source, usually ranging from near infra-red to ultra-violet, is passed through a set of polarizers and retarders, thus defining the polarization of the incoming light on a surface. In turn, the polarization of the relected light is determined by the combination of another polarizer and a detector. Ellipsometry is a specular optical technique, meaning the angle of incidence is equal to the angle of reflection and span the plane of incidence in a material. Consequently, the linear polarized light incident upon the sample can be decomposed into two components: an s component which oscillates perpendicular and a p component which oscillates parallel to the plane of incidence. Ellipsometry basically measures how p- and s- components of a wave change in relation to one another upon reflection on the surface. Accordingly a known polarization is reflected onto the sample and the ouput polarization is measured. This change in polarization can be written as the complex ellipsometric parameter ρ:

$$\rho = \frac{R_p}{R_s} = \tan(\Psi)e^{i\Delta} \qquad \text{Eq. 1}$$

where, $R_p$ and $R_s$ , are the complex Fresnel reflection coefficients determined by the magnitude of the s and p components before and after reflection, and correspond to the

product of the amplitude ratio, tan(Ψ), and the phase shift, Δ, induced by the reflection. Δ is denotes the phase difference between p- and s- wave components respectively, before and after reflection, where:

$$\Delta = \delta_1 - \delta_2 \qquad \text{Eq. 2}$$

Figure 15 demonstrates the relationship between the incoming linearly polarized light and the outgoing elliptically polarized light.

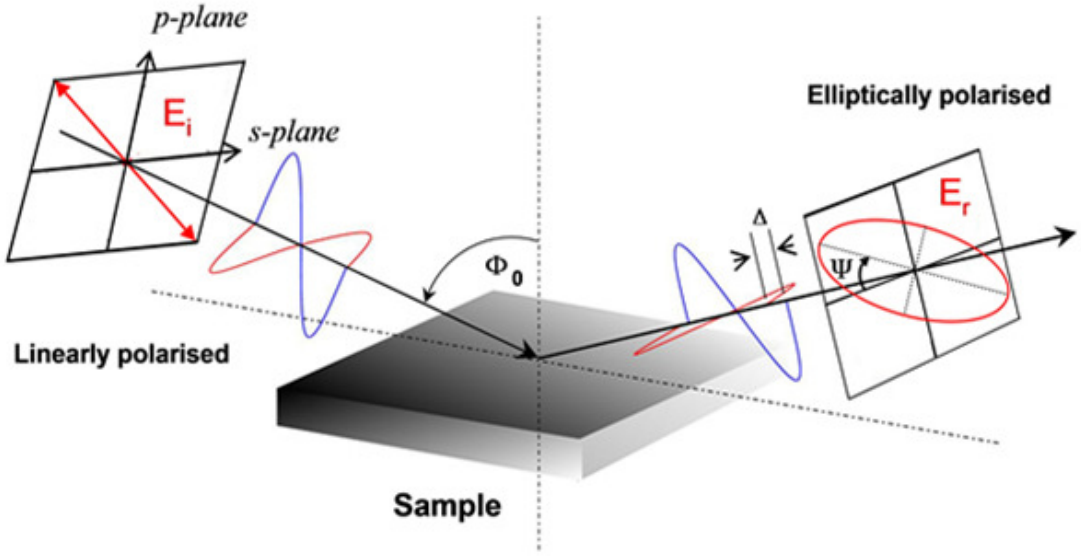


**Figure 15. Ellipsometry measures the change of polarization of a linear polarized light when reflected on a surface. Upon interference with the film, the reflected light is elliptically polarized. Film properties, thickness, and refractive index are determined by the measure in phase change, Δ, and amplitude change, Ψ, of the reflected light.[83]**

From the data obtained, the film thickness and the complex refractive index, ñ, over the photon energy range can be determined.[80-82] The complex refractive index is expressed as

$$\tilde{n} = n + ik \qquad \text{Eq. 3}$$

where n is the index of refraction and k is the extinction coefficient, but they are often represented in terms of the real, $\varepsilon_1$, and imaginary, $\varepsilon_2$, parts of the complex dielectric function ε where

$$\varepsilon = \varepsilon_1 + \varepsilon_2 \qquad \text{Eq. 4}$$

$$\varepsilon_1 = n^2 - k^2 \qquad \text{Eq. 5}$$

$$\varepsilon_2 = 2nk \qquad \text{Eq. 6}$$

However, because film properties are not measured directly (only Ψ and Δ are) but instead have to be extracted from models, such as Drude and Cauchey. The models are setup to describe the film structures on the sample and then fit the data using a regression analysis. Therefore, determining a films index of refraction and subsequent thickness can be difficult to determine due to the fact that the index of refraction will change with film thickness for very thin films and as the number of unknown properties increases, the more convoluted the data becomes.[82] However, a variable angle spectroscopic ellipsometer such as the Sopra GES5 allows for the interrogation of complex structures where each wavelength and angle will provide a new set of (n, k) values and corresponding equations.

### 2.3.2 Sopra GES5 ellipsometer

A Sopra GES5 spectroscopic ellipsometer was used for rapid film characterization. The GES5 uses a 75W high intensity Xenon arc lamp in order to obtain a continuous spectrum of light from 1.2 to 6.5 eV (190-1030 nm). The use of the ultra-violet range is particularly useful to study high band gap materials, such as $TiO_2$. Figure 16 displays the configuration of a rotating polarizer and a fixed analyzer. At location A, the linearly polarized light is reflected upon the surface where it is elliptically polarized during location B. As the polarizer rotates, the ellipticity of the beam is varied with time. The light is again linearly polarized when passed through the fixed analyzer at location C, however this time its amplitude varies with the relative position of the fixed analyzer. The GES5 uses a charge coupled device (CCD) detector adapted for a grating spectrograph. A goniometer is used to vary the angle of incidence θ from 7° to 90° along with a 200 mm automated XY stage for wafer mapping. With the use of microspot optics the beam spot size can be reduced from its nominal 1-5 nm dimensions down to 365 x 270 µm.

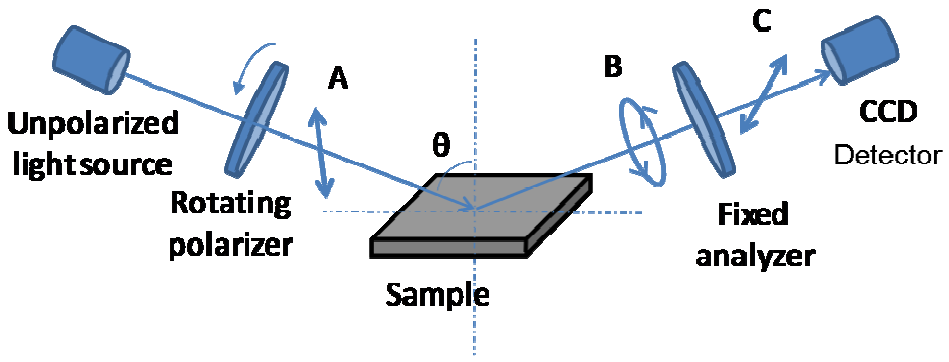


**Figure 16. Sopra GES5 spectroscopic ellipsometer configuration.**

## 2.4 Scanning Electron Microscopy

### 2.4.1 Operational principles

With features residing in the nanoscale, a strong need exists to image such small features. Optical microscopes are limited by their lack of resolution on such small features therefore, electron microscopes are used to reveal information about a samples morphology, chemical composition, and crystalline structure and orientation of materials making up a sample.[84] An SEM operates by using a focused beam of high-energy electrons to generate a variety of signals that can be used to image the surface of a sample. The most common thermionic electron gun uses a tungsten filament cathode because it has a high melting point and lowest vapor pressure of all the metals, thereby allowing it to be heated high enough to produce the emission of electrons. Other types of electron emitters are lanthanum hexaboride ($LaB_6$) cathodes, Schottky emitters of zirconium oxide, or a tungsten field-emission tip.[84, 85] Through the interaction of the electrons and atoms at or near the surface of the sample secondary electrons, back-scattered electrons (BSE), characteristic x-rays, light (cathodoluminescence), and transmitted electrons can be produced in order to reveal details about samples 1 to 5 nm in size.[84, 85]

In order to produce an image, the electron beam with an energy ranging from 0.5 keV to 40 keV, is focused by one or two condenser lenses to a spot of about 0.4 nm to 5 nm in diameter.[86] The beam then passes through a pair of scanning coils which deflects the beam on an x and y axes so that it scans in a raster fashion over a rectangular

area of the sample surface. When the beam interacts with the sample, the incoming electrons lose energy by repeated scattering and absorption within a teardrop-shaped volume of the sample called the interaction volume, which can extend from 100 nm to around 5 μm into the surface depending on the atomic number of the sample, the sample's density, and the accelerating voltage of the beam.[84, 85] The energy exchange between the electron beam and the sample results in the reflection of high-energy electrons by elastic scattering, emission of secondary electrons by inelastic scattering and the emission of x-rays, each of which can be detected by their own specialized detector.[84] Signals emitted from the sample are collected by their respective detectors and amplified, where the intensity is then modulated on a TV monitor and rastered in synchronization with the electron beam in order to produce an image.[84] Figure 17 displays a schematic of an SEM operational setup. In order to increase the magnification of the image, the raster size on the sample is decreased.[84]

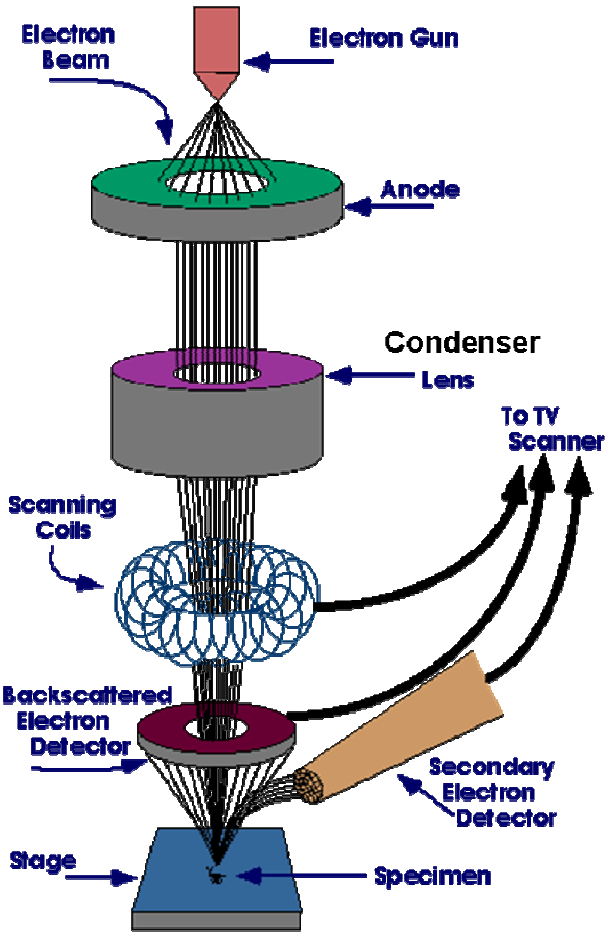


**Figure 17. Schematic of an SEM setup.[87]**

### 2.4.2 Hitachi SU-70 SEM

A Hitachi SU-70 SEM with a ZrO/W Schottky field emission gun was used to image top down and cross-sectioned samples of AAO in order to characterize AAO pore sizes and ALD film thicknesses. For high resolution images an accelerating voltage of 10 kV was used with the probe current set on high in medium mode. Using a working distance of 5 mm, secondary electrons were collected using a mixture of upper and lower detectors.

### 2.4.3 Cross-sectional sample preparation

In order to fabricate porous AAO samples for cross-sectioning, samples were epoxied to a small piece of silicon with a notch scribed in the back center pore side down. The backside of the AAO template was scratched to induce etching of the aluminum substrate in a $Cu_2Cl$ solution. Templates were etched with help of a sonicator for approximately 20 min followed by sonicating the sample in isopropanol for an additional 10 min removing any Cu particles left on the surface. Samples were then cleaved using the notch in the back side of the silicon as an initiator. See Figure 18 for a schematic of the sample prep process flow. Before imaging samples were coated with a thin film of sputtered Au/Pd in order to reduce sample charging during measurements. Au/Pd films were sputtered using a small table top sputter in Dr. Sang Bok Lee's lab. The chamber was evacuated to ~60 mTorr and samples were coated using an argon generated plasma for 15 sec.

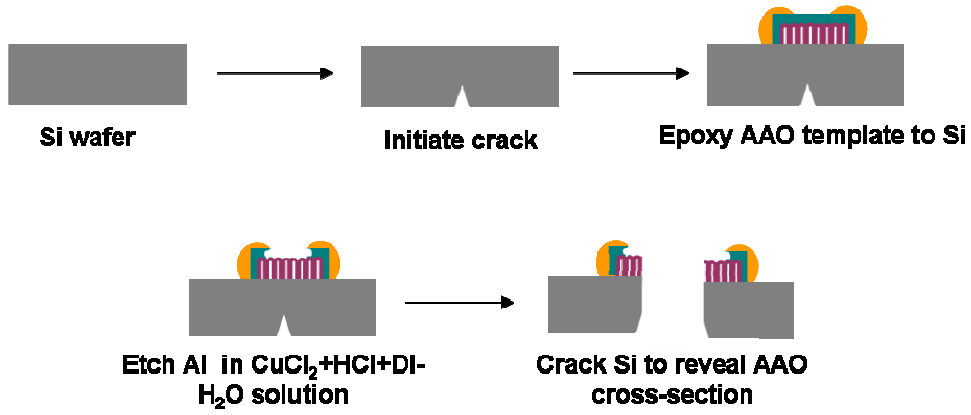


**Figure 18. Schematic of SEM sample preparation for AAO cross-sections.**

## 2.5 Transmission Electron Microscopy

### 2.5.1 Operational principles

Transmission electron microscopy (TEM) is a powerful tool for investigating the microstructure of samples on the nanoscale. TEM uses a high energy beam of electrons to transmit electrons through a sufficiently thin sample. The maximum thickness for an electron to transmit through depends upon the atomic number of the material, where this range typically lies between 250-500 nm.[86] However, higher electron energies help transmit more electrons through the sample.

A TEM is a complex tool composed of an illumination system, specimen stage, and an imaging system all within an evacuated column. The illumination system is comprised of an electron source usually using a tungsten filament of a $LaB_6$ crystal, together with an assembly of condenser lenses located above the sample. The specimen stage can either be held stationary or moved with the use of a double tilted stage. The imaging system is made up of an objective lens, intermediate lenses, a projector lens, and a phosphor screen all positioned beneath the sample as seen in Figure 19. After electrons are emitted from their source they are accelerated to their final kinetic energy by applying a potential difference to a cathode and an anode, which is a metal plate containing a central hole in which the beam is accelerated through. The beam is then sent through a strong magnetic lens called the first condenser lens. This lens forms a demagnified image of about 1 μm in diameter and is then projected on to the specimen by a second condenser lens with a magnification typically around 2.[86] The final illumination spot

on the specimen can be a small as 2 μm, which should be sufficient to fill the viewing screen.[85, 86]

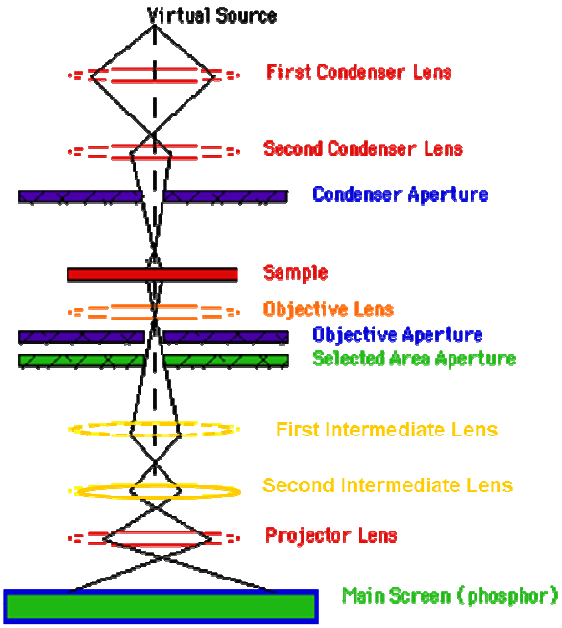


**Figure 19. Schematic of the path an electron beam takes within the evacuated column of a TEM.[88]**

All TEM specimens are made a standard 3 mm diameter circular disk, where the specimen must be thin enough to allow electrons to be transmitted. The specimen stage is meant to hold samples as stationary as possible, as any vibrational causing drifts would be magnified in the final image.

Electrons that have been transmitted through the sample are then focused through an objective lens with a small focal length. Therefore, the objective lens produces a magnified real image of the specimen at ~10 cm below the center of the lens. The beam then passes through an objective aperture, which is comparable to a diaphragm that helps produce contrast in the image and limits the amount of blurring that arises from spherical

and chromatic aberrations. The beam then travels through a selected area aperture, which is a diaphragm that is inserted in the plane that contains the first magnified real image of the specimen, i.e. the image plane of the objective lens. This diaphragm is used to record the electron diffraction pattern associated with the sample. Most TEMs make use of several intermediate lenses between the objective lens and the projector lens. The lenses are used to first, change the beams focal length into smaller step allowing the overall magnification of the TEM to be varied over a large range, ~ $10^3$ to $10^6$ and second, by producing an electron diffraction pattern on the TEM viewing screen. A projector lens is used to produce an image or a diffraction pattern across the entire TEM screen. In order to determine the magnification of the image it is an algebraic product of the magnification factors associated with each of the imaging lenses used. A phosphor screen is used to display the electron image as a visible form.[85]

### 2.5.2 JEOL 2100F field emission TEM

A JEOL 2100F microscope with a $LaB_6$ thermionic emission electron source operated at 200 keV and a post-column Gatan CCD camera were used to image $TiO_2$ ALD based nanotubes held on a double tilted specimen holder. Much of the focusing and imaging was done by Dr. Larry Lai of the NispLab staff.

### 2.5.3 Nanotube sample preparation

$TiO_2$ ALD based nanotubes were fabricated by the dissolution of the porous AAO membrane the ALD films were deposited in. Samples were placed in a 25 wt% phosphoric acid solution for 24 hrs, which dissolved the alumina membrane thus

releasing the $TiO_2$ nanotubes in solution. Nanotubes were filtered using DI water and a drop of solution with dispersed nanotubes was placed on a standard holy-carbon TEM grid and left to dry for several hours.

## 2.6 Energy Dispersive X-ray Spectroscopy

### 2.6.1 Operational principles

Scanning electron microscopy (SEM) and scanning transmission electron microscopy (STEM) in conjunction with energy dispersive x-ray spectroscopy (EDS), is a powerful tool for obtaining chemical information from a wide variety of materials found in nanotechnology. EDS is an analytical technique which utilizes x-rays that are emitted from the specimen when bombarded by the electron beam of an electron microscope in order to identify the elemental composition of the sample.[89] When a high energy electron bombards an atom in the sample, an electron is ejected from an inner shell leaving a vacancy in its place, see Figure 20. This vacancy is then filled by an electron from a higher energy state and releases energy in the form of an x-ray. This emitted x-ray is characteristic of the element from which it was emitted. Therefore, elements with high atomic numbers will produce more x-rays. This type of x-ray is called a characteristic x-ray.[89] In addition to characteristic x-rays, there are also background x-rays called "Bremsstrahlung" radiation. Bremsstrahlung radiation is produced by the deceleration of an electron as it passes through the sample. Bremsstrahlung x-rays are also dependent upon the atomic number of the material being analyzed, but are not a good source for quantitative analysis and are in large part

responsible for background noise during analysis.[85, 89]

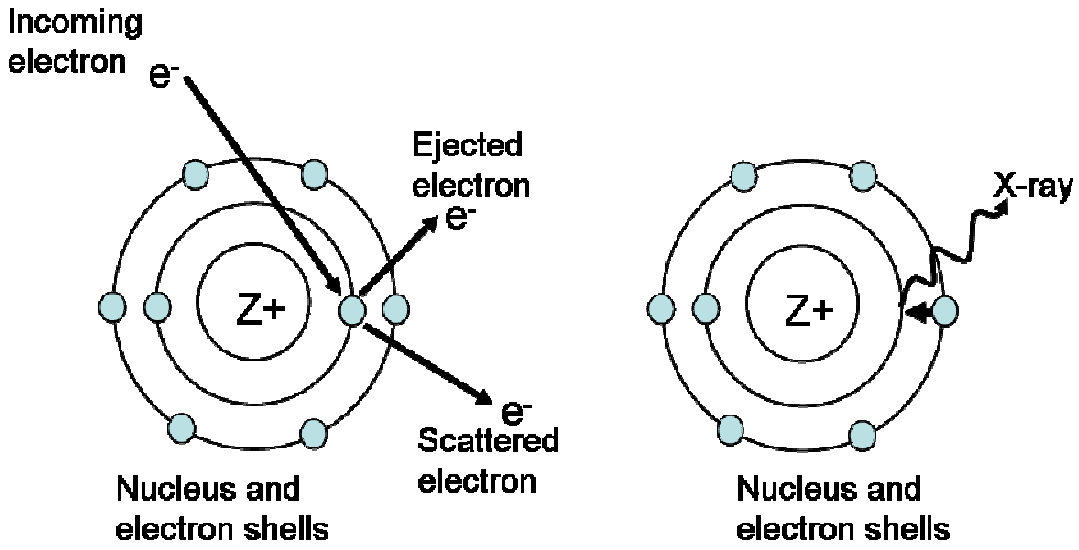


**Figure 20. Characteristic x-ray production.**

When an x-ray enters the detector it passes through a beryllium window, where they are collected by a solid state detector comprised of a single crystal of silicon with a layer of lithium diffused within. When x-rays enter the detector they create electron-hole pairs, where the number of electron-hole pairs are equivalent to the energy of the x-ray.[85, 86, 89] The detector is cooled using liquid nitrogen in order to reduce containments, as well as limit the production of electron-hole pairs through thermal generation.[85] The charge produced from the electron-hole pair is converted to a voltage by a field effect transistor (FET) preamplifier and then sent to a multichannel analyzer where the voltages are sorted.[86] The energy for each incident x-ray, as determined from the voltage measurement, is sent to a computer display for further user analysis.[86]

### 2.6.2 Bruker EDS detector

A Bruker EDS detector was used in combination with a Hitachi SU-70 SEM in order to obtain quantitative chemical analysis of thin films. Because SEM samples tend to be thicker, it is easier to focus the electron beam within the sample allowing for complete absorption of the beam in the sample. This causes the beam to spread within the sample and leads to a higher generation of x-rays as seen in Figure 21.

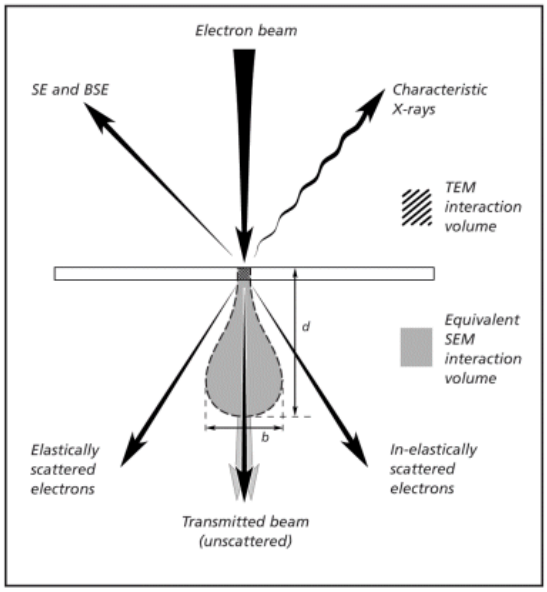


**Figure 21. Schematic of the diminished electron beam interaction within a TEM sample versus an equivalent SEM sample.[90]**

### 2.6.3 Oxford EDS detector

An oxford EDS detector was used in conjunction with a JEOL 2100F Field Emission TEM. TEM requires the use of very thin samples in order to transmit electrons through the sample; therefore, few x-rays are produced than those found in SEM, as seen in Figure 21.[90]

## 2.7 Atomic Force Microscopy

### 2.7.1 Operation principles

Over the past 20 years, the quest for miniaturization has led to an increased interest in characterizing the unique quantum and surface phenomena that matter exhibits at the nanoscale. Atomic force microscopy (AFM) is a type of scanning probe

microscopy that provides very high resolution down to the nanometer scale to provide 3-dimensional images of a specimen's surface topography. AFM operates by bringing an extremely sharp tip in contact or in very close proximity to a sample in order to scan the sample's surface.[86] The tip is usually a couple of microns long with a radius of curvature of less than 100 Å in diameter and is located at the free end of a silicon or silicon nitride cantilever, 100 to 200 μm long (Figure 22).[91] The tip is brought into close proximity of the sample's surface, where the forces between the tip and the sample lead to a deflection of the cantilever. Typically deflections are measured by a laser reflected from the top surface of the cantilever and into an array of photodiodes where the signal is fed into an electronic interface and computer in order to control the feedback keeping the force constant while scanning the sample surface (Figure 23).[86] Other techniques commonly used are optical interferometry, capacitive sensing, or the use of piezoresistive cantilevers.[91] Depending on the sample setup many physical properties can be determined through the types of forces measured, such as mechanical contact forces, van der Waals forces, capillary forces, electrostatic forces, magnetic forces, chemical bonding, etc.[86, 91, 92] In comparison to other microscopy techniques, AFM provides comparable or better topographical information and unobstructed views of the surface because images are obtained without expensive sample preparation or conductive coatings often necessary in SEM and TEM imaging.

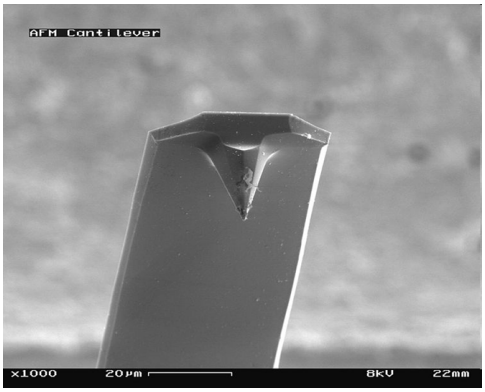


**Figure 22. SEM image of the AFM Si tip at the free end of a Si cantilever.[92]**

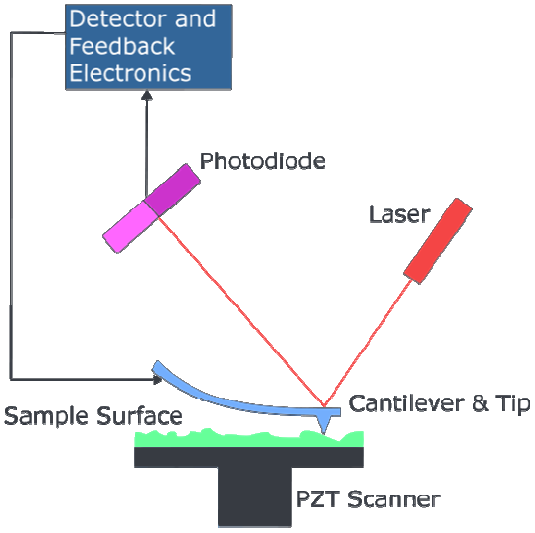


**Figure 23. Schematic of an AFM operational setup.[92]**

AFM probes can operate in two modes: constant force mode and tapping mode. In constant force mode the force between the tip and the sample is kept constant by forcing the tip to remain in contact with the sample. In this case samples can either be rastered underneath the tip while the tip remains stationary or the probe can be scanned over the sample. However, in either mode the sample can become damaged causing a loss in resolution as the sample is continually rastered. Therefore, to reduce this problem, AFM systems have been modified to operate in a tapping mode. In tapping mode, the cantilever is lightly tapped against the sample, reducing lateral shear forces and reducing damage to the sample. The cantilever is oscillated up and down near its resonance frequency by a small piezoelectric element mounted in the AFM tip holder. This mode is particularly useful for mapping polymers and other biological samples.[86, 91]

### 2.7.2 MFP-3D AFM

An MFP-3D stand alone atomic force microscope was used for easy topographical mapping across a sample. The MFP-3D used a silicon tip in tapping mode at a scan rate of 1 Hz and a driving frequency of 200 kHz. Samples were mounted on glass slides where 1 μm scans were made across sample surfaces. The AFM stage was encased in a vibration damping box on top of a levitated optical table in order to eliminate environmental vibrations that may have influenced surface measurements.

# Chapter 3 : Profile Evolution for Conformal ALD Over Roughened Nanotopography

The self-limiting reactions which distinguish atomic layer deposition (ALD) provide ultrathin film deposition with superb conformality over the most challenging topography. This chapter addresses how the shapes (i.e. surface profiles) of nanostructures are modified by the conformality of ALD. As a nanostructure template, we employ a highly scalloped surface formed during the 1$^{st}$ anodization of the porous anodic alumina (PAA) process, followed by removal of the alumina to expose a scalloped Al surface. SEM and AFM reveal evolution of surface profiles that change with ALD layer thickness, influenced by the way ALD conformality decorates the underlying topography. The evolution of surface profiles is modeled using a simple geometric 3D extrusion model, which replicates the measured complex surface topography. Excellent agreement is obtained between experimental data and the results from this model, suggesting that for this ALD system conformality is very high even on highly structured, sharp features of the initial template surface. Through modeling and experimentation the benefits of ALD to manipulate complex surface topographies are recognized and will play an important role in the design and nanofabrication of next generation devices with increasingly high aspect ratios as well as nano-scale features.

## 3.1 Introduction

Paralleling the trend in electronic devices, high surface area 3D architectures for applications in energy [21, 93], catalysis [18, 61], and sensors [30, 94] are exploiting the benefits found in using nano-scaled structures with increasingly high aspect ratios. In exploiting these nanostructures, the 3D topography is perhaps even more complex and demanding than in conventional applications found in ULSI based applications such as those demonstrated in trench and stacked capacitors in DRAM devices [9], barrier technology for copper metallization[95], and gate dielectric deposition on planar Si [8] and Fin-FET geometries [13]. For example, Banerjee et al recently demonstrated a novel metal-insulator-metal (MIM) nanocapacitor using a combination of self-limiting processes to build multilayered functional films and self-assembled nanotemplates with nanopores ~50 nm wide x 10 μm deep (aspect ratio= 200) [21]. In these structures, a primary performance limitation was set by the geometry of the nanoporous template consisting of sharp asperities, leading to enhanced local electric fields and low field breakdown which would ultimately limit energy storage density [21]. This example emphasizes the need for understanding and optimizing our ability to synthesize complex 3D nanostructures. Complex surface topographies consisting of high aspect ratios, sharp asperities, and nano-roughness significantly challenge the ability to conformally coat complex nanostructures using traditional physical vapor deposition (PVD) and chemical vapor deposition (CVD) techniques [66, 94, 96]. However, atomic layer deposition (ALD) offers high quality films with atomic level thickness control and unprecedented uniformity and conformality in the most demanding 3D nanostructures [1, 2, 67].

In this chapter, we explore the evolution of surface profiles for ALD films deposited on a prototype of a topographically rough surface. We utilize highly scalloped Al templates formed by the removal of porous anodic alumina (PAA) membranes. PAA is a self assembled, electrochemical templating technique that results in a highly dense close-packed hexagonal array of cylindrical nanopores on the surface of aluminum [97]. PAA naturally lends itself to many nanotechnology applications, such as a template for growing nanowires and nanotubes and for self assembling these structures in parallel, periodic arrays used to fabricate catalysts membranes [61, 94], dye sensitized solar cells [98], batteries [99] and sensors [30, 94]. When the PAA film is etched off, a self-ordered, close-packed hexagonal array of nano-dimples is left imprinted in the underlying aluminum surface (Figure 24a) [100]. Nearest neighbor dimples meet at sharp points and the overall surface topography consists of periodic peaks and valleys (Figure 24b). Such surfaces are ideal for testing the influence of film conformality on surface topography.

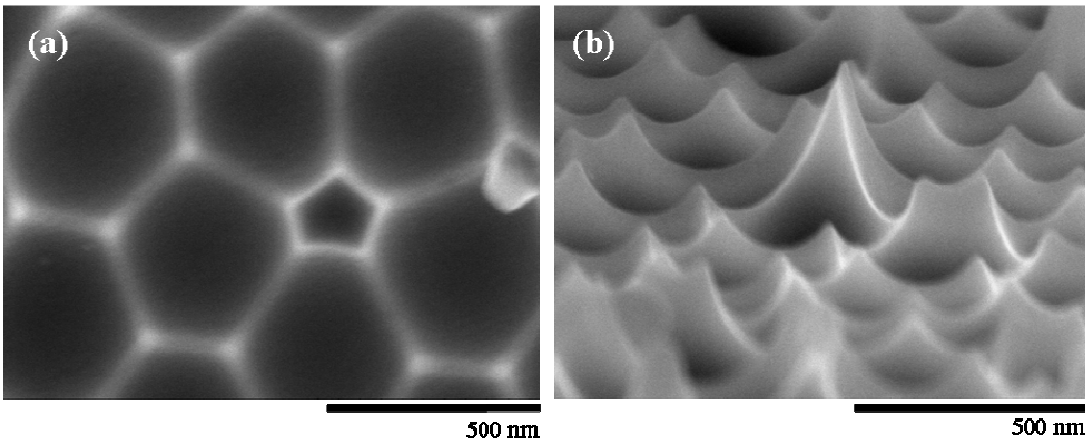


**Figure 24. A removed PAA template imaged in SEM: (a) top-down view of the hexagonal nano-dimple array and (b) cross-section view of the scalloped Al surface, emphasizing the peak structure above the nano-dimples.**

ALD is a self-limiting process which utilizes sequential chemisorbed surface reactions of precursor molecules to achieve deposition one monolayer at a time and is dependent upon molecule flux, adsorption/desorption probability, and surface diffusion [3]. Much work has focused on analytically understanding the performance of ALD conformality, particularly in high aspect ratio structures where process metrics, i.e., reactant exposures and purge times, must be modified to compensate for the higher surface areas and molecular flow type dynamics occurring in 3D nanostructures. This includes developing simple models for determining precursor dose for conformal coatings [66], using Monte Carlo techniques [67], solving simultaneously Boltzmann's transport and surface reaction equations [101] and correlating them with experimental results while trying to optimize conformality in ultra-high aspect ratio structures. The prevailing message in the above reports is that ALD yields unparalleled performance when it comes to depositing thin films across complex 3D nanostructures, but requires precise process control to ensure complete surface saturation and avoid excess deposition characteristic of CVD-like behavior [3]. On the other hand, the surface evolution of ALD films across complex surface topographies, especially with sharp asperities and nano-roughness has not been systematically explored – experimentally or theoretically. Such complex topographies are still likely to incur complete saturation reactions and avoid topography induced nucleation delays that could potentially affect the conformality of the films and the resulting topography [3, 5]. Therefore this work is aimed at investigating the surface evolution of ALD films in the context of highly scalloped surfaces.

Our test-bed utilizing a combination of a removed PAA membrane from an Al

template and ALD provides us with the ability to monitor surface evolution of ALD films as they are deposited on a highly scalloped surface. We use two different templates with different interpore spacings ($D_{int}$) to reveal a universal behavior for the growth of ALD films on such surfaces following simple scaling laws. Furthermore, a surface extrusion model is used to verify this behavior and the resulting surface area as a function of ALD deposition thickness. This work demonstrates that through modeling and experimentation the benefits and limitations of ALD can be realized for complex nanostructures. Understanding this behavior will play a crucial role in the design and nanofabrication of next generation energy devices with increasingly high aspect ratios as well as nano-scale feature sizes.

## 3.2 Materials and Methods

Scalloped aluminum templates were synthesized by the removal of PAA membranes formed during a one-step anodization method [79]. High purity 200 μm thick aluminum foils (99.99%, Alfa Aesar), were electropolished in a 1:5 perchloric acid to ethanol bath held at ~ 3 °C in order to remove micro-roughness from the surface, which influence the quality of the pores. The electropolished aluminum was then anodized at (1) 40 V and 10 °C in an electrolytic bath of 0.3M oxalic acid to achieve an interpore spacing, $D_{int}$, of 110 nm or (2) at 160 V and 4°C in an electrolytic bath of 10 wt% phosphoric acid to achieve $D_{int}$ of 450 nm. Foils were anodized for ~7 hours so PAA pores would self organize and align orthogonally with respect to the underlying Al substrate. After anodization, the PAA film produced was removed in an aqueous solution of phosphoric acid (6 wt%) and chromic acid (1.8 wt%) at 60 °C leaving a hexagonally

organized nano-dimple array with a highly scalloped surface imprinted in the remaining aluminum.

Titanium dioxide ($TiO_2$) ALD thin films were thermally deposited at 150 °C in a Beneq TFS-500 cross-flow ALD reactor using Tetrakis(dimethylamido)titanium (TDMAT) and water. Pulses and purges of 500 msec for both precursors resulted in atomic thickness control with a growth rate of 0.055 nm/cycle as a sub-monolayer of film was consistently deposited for each cycle. Three samples were loaded during the first run and deposition was carried out in 3 intervals of a fixed number of cycles, i.e. 244 or 1000 for templates anodized in oxalic or phosphoric acid, respectively. After each interval one sample was removed from the reactor and characterized via high resolution scanning electron microscopy (SEM, Hitachi SU-70) and atomic force microscopy (AFM, MFP-3D Asylum Research) in tapping mode. Film growth rates were determined using a spectroscopic ellipsometer (Sopra GES5) on planar Si samples.

## 3.3 Results & Discussion

The evolution of ALD surface profiles over complex nano-topography was investigated with particular focus on how ALD modifies surface topography. PAA membranes formed in phosphoric acid with a $D_{int}$ of 450 nm were removed from the underlying aluminum surface revealing a highly textured surface of peaks and valleys that rise above an array of hexagonal dimples as seen via cross-sectional SEM (Figure 24a-b). Peaks are seen positioned along the [121] direction of the template, whereas valleys are found to traverse the [111] direction. Peak structures are multifaceted in shape due to the convergence of multiple hexagonal dimples. Peaks that rise notably above the

average peak height and non-hexagonal dimples are considered defects. Defects are preferentially found along domain boundaries and are generally created during the anodization process when starting from a completely disordered structure, as opposed to a stamped template where the ordering is considered perfect [102].

Templates formed in phosphoric acid were coated with three consecutive layers of 1000 cycle $TiO_2$ ALD. Top-down SEM images display surface profiles of $TiO_2$ ALD deposited on the scalloped Al surface after 0 cycles, 1000 cycles, 2000 cycles, and 3000 cycles (Figure 25a-d). Images reveal that increased ALD deposition results in the formation of triangular patterns originating from the peak structures across the surface. In Figure 25b, it appears that ALD deposition is nucleating at these sharp tips, thus dominating ALD growth across the surface and creating areas of higher growth over others as seen in Figure 25c. As deposition continues, growth fronts originating from these peaks start to merge and exhibit symmetric, repeating patterns of raised triangles decorating the surface with “nano-petunias” as seen in Figure 25d.

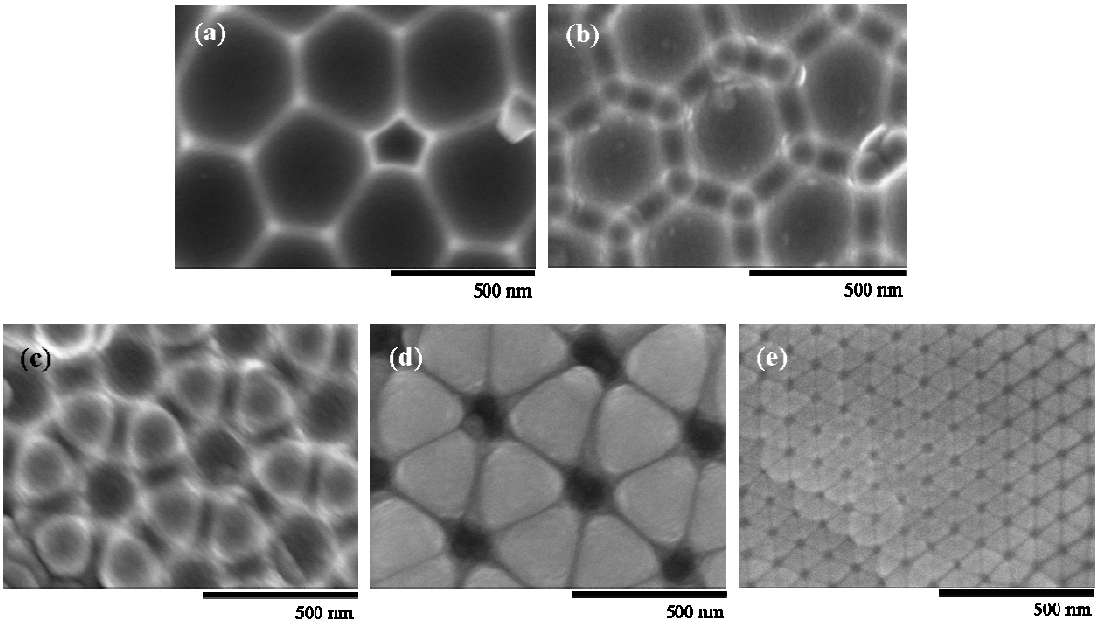


**Figure 25. Progression of TiO2 ALD profiles across a scalloped Al surface formed using phosphoric anodizing acid imaged in SEM after (a) 0 cycles, (b) 1000 cycles (~55 nm), (c) 2000 cycles (~110 nm), and (d) 3000 cycles (~165 nm). (e) SEM image of a scalloped Al surface using oxalic anodizing acid coated with 733 cycles (~40 nm) of TiO2. Top-down images (d and e) display the same formation of triangular ALD surface profiles for the same ratio of equivalent thickness (t) to interpore spacing distance (Dint) for each anodizing acid.**

A simple scaling law was devised to adequately compare the ALD surface profiles deposited on templates formed with different interpore spacing using either phosphoric or oxalic acid. Using the film's growth rate, deposition on one template could be scaled by a factor of k defined in equation (1) as

$$k = {}^{t}\!/_{D_{\text{int}}} \tag{1}$$

where t is the measured film thickness for a set number of cycles deposited on planar surfaces, in order to calculate an equivalent film thickness (τ) for a template with a

different interpore spacing ( $D_{\text{int}}^{o}$ ). Leaving $\tau = k * D_{\text{int}}^{o}$ . SEM images display templates produced with different interpore spacings of 450 nm for phosphoric acid (Figure 25d) and 110 nm for oxalic acid (Figure 25e) coated with equivalent film thicknesses of 165 nm for 3000 cycles and 40 nm for 733 cycles of $TiO_2$ ALD, respectively. Both samples display the formation of triangular patterns across the surface, revealing a universal behavior for templates with similar scalloped surfaces but different dimensions.

$TiO_2$ films were deposited for 733 cycles to a film thickness of ~40 nm on scalloped Al templates formed in oxalic acid. A tilted top-down SEM image of a thin delaminated film of $TiO_2$ retaining the original hexagonal pattern from the initial scalloped Al surface is shown in Figure 26a. However, the film's surface topography no longer displays the sharp peak structures that extruded from the initial, now-covered surface. A tilted-bottom up view of the delaminated film suggests the emergence of growth fronts for the evolving ALD film, where they eventually merged as indicated by arrows in Figure 26b. As a $TiO_2$ film is conformally deposited over the original scalloped template, the ALD film topography changes shape with deposition and displays substantial smoothing of the original scalloped surface. This behavior underscores the benefits of conformal ALD to blunt or smooth sharp asperities and surface features with increasing film thickness. This is particularly important in some applications, e.g., for local enhancement of electric fields at asperities and consequent low field breakdown of an MIM nanocapacitor [21].

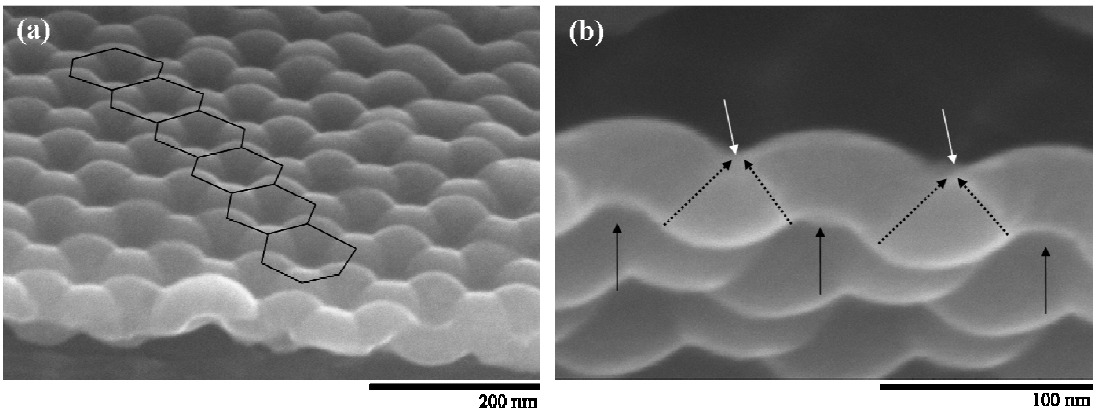


**Figure 26. A delaminated conformal TiO2 ALD film imaged in SEM: (a) tilted top-down view of merged growth fronts influenced by the hexagonal pattern of the removed underlying surface and (b) tilted bottom-up view of the film where dashed arrows in the cross-section indicate where growth fronts merged and laterally moved due to film broadening at the peaks (solid black arrows) and causing the disappearance of the nano-dimples (solid white arrows).**

We attribute the display of growth fronts to the direct consequences of ALD conformality over surface topography that includes rounded as well as sloped regions. While other physical or chemical deposition mechanisms convey some measure of conformality over topography, ALD's self-limiting chemistry provides unprecedented capacity to maintain conformality even in the most challenging nanotopography. Sidewall deposition, i.e. on the inclined surfaces, is as rapid as on the rounded surfaces. This causes the rise of directional growth fronts where there is a significant change in incline on the surface (i.e. shift from the sloped side walls to that of the concave valley or dimple). Growth fronts merge at crossing points between the inclined and curved regions and move laterally as deposition proceeds as indicated by the dashed arrows found in Figure 26b. When the initial surface is comprised of scalloped peaks and valleys that rise above lower dimples, the successive ALD layers exhibit changes in the surface profile,

leading to the lateral growth and rounding of the peaks and reduction (or ultimately disappearance) of the valleys and lower dimple areas, as seen in Figure 26b.

This behavior is evident from AFM maps for ALD $TiO_2$ film profiles seen in Figure 27. $TiO_2$ films deposited on templates formed in phosphoric acid for 0 cycles, 1000 cycles (55 nm), 2000 cycles (110 nm), and 3000 cycles (165 nm) were mapped using AFM in order to monitor the progression of surface profiles and the decrease in surface area with increasing ALD film thickness. Figure 27a displays an AFM contour map for 2000 ALD cycles (110 nm), with the position of underlying peaks (A, B, C, and D) of the initial scalloped surface denoted along with the [121] and [111] directions. The map illustrates the emergence of triangular surface profiles as areas of higher topography allow growth fronts to extend out and finally merge along the [111] direction. AFM line scans taken of increased deposition across the [121] direction were layered and separated by the experimental growth rate for $TiO_2$, where 0, 1, 2, and 3 indicate the number of intervals for 1000 cycles, with 0 being the bare template (Figure 27b).

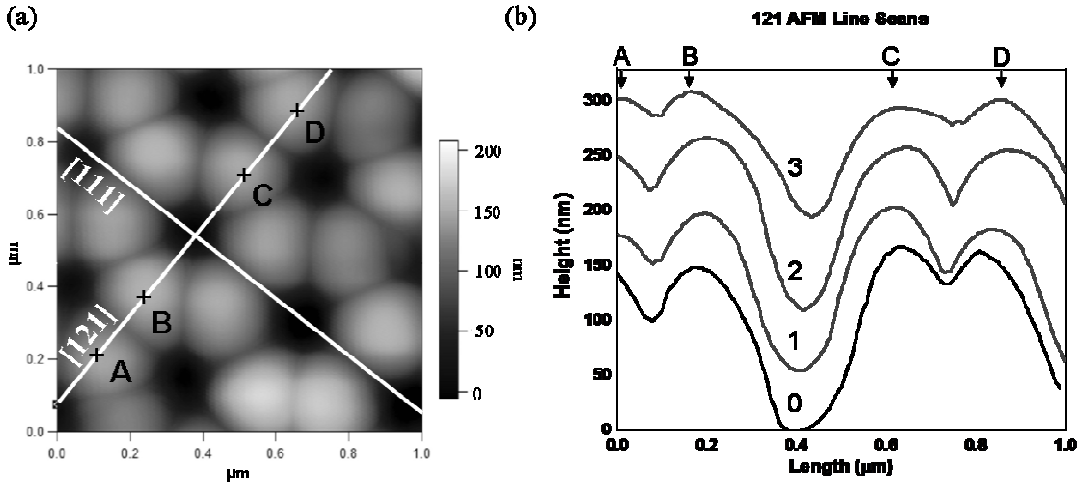


**Figure 27. (a) AFM contour map of a 2000 cycle (~ 110 nm) TiO2 ALD film on a scalloped Al surface dictating the [111] and [121] directions with peaks A, B, C, and D (denoted by x) across the template. (b) AFM line scans across the 121 direction after 0 cycles, 1000 (~ 55 nm), 2000 cycles (~110 nm), and 3000 cycles (~165 nm) of deposited TiO2 ALD (arrows denote locations of peaks). The profiles are numbered 0-3 for intervals of 1000 cycles each.**

These results illustrate the broadening of peaks in the original scalloped surface initiated at positions A, B, C, and D. As neighboring peaks positioned at A and B as well as C and D expand, they first cause a sharpening of the valley between them, and then begin to close and diminish the valley with further ALD coverage. At the location of the original dimples in the scalloped surface, e.g. between B and C, much less of this effect is seen due to the lower plateau centered at the dimple being considerably wider to begin with. Ultimately, this behavior lends itself to the formation of the triangular pattern or "nano-petunias" across the surface. Although surface features of the samples were smaller than the AFM tips used, an increase in deposition indicates a decrease in surface area as growth fronts merge and the complex peak structure is rounded. ALD's ability to

conformally coat and thereby modify a topographically rough surface will prove to be of great importance when engineering detailed geometries sometimes found in 3D nanostructures. For example, ALD growth kinetics in high aspect ratio structures become primarily mass-transport limited via molecule diffusion in and out of the pores rather than surface reaction-limited [66]. Therefore, as the ALD deposition profile evolves, the entrance to a pore potentially found between B and C in Figure 27 will start to close off, creating an ever decreasing orifice diameter for molecules to diffuse through with each cycle, and increasingly challenging ALD's ability to conformally deposit within a high aspect ratio nanopore.

## 3.4 ALD-PAA Simulation

A simple geometric 3D extrusion model was developed by Dr. Israel Perez, a former graduate student, to demonstrate the influence of a complex surface topography and track the progression of ALD surface profiles. The model replicated the topography found on a scalloped Al template after removal of the PAA membrane by using the two key dimensions: interpore spacing, $D_{int}$, and the scallop's equivalent sphere radius, $r_s$. The interpore spacing of the scalloped array is a well known dimension and is related to the anodization potential used for a specific anodization acid [103]. For the purpose of this simulation $D_{int}$ is taken as 105 nm corresponding to oxalic acid templates. The $r_s$ value is the radius of curvature of the nano-dimple imprinted in the Al surface and was extrapolated from AFM data of a bare scalloped Al surface. The maximum peak height was measured as the difference in the z-height between the bottom of the dimple and the top of the peak, which for a PAA surface anodized in oxalic acid at 40 V is

approximately 42 nm. Knowing this value allows the surface to be modeled by adjusting $r_s$, until the maximum ideal peak height is ~42 nm, which gives a value of $r_s$ ~65 nm. Therefore, an ideal scalloped surface was coded in MatLab® by spacing hemispheres with radius $r_s$ in a hexagonal array, with inter-sphere spacing of $D_{int}$ in the closed pack direction, and removing all intersecting data.

As mentioned earlier, much work already exists in the literature covering the strict theoretical modeling of ALD in terms of thickness as a function of cycles [104], nucleation and growth kinetics [53], and Monte Carlo simulations in ultra-high aspect ratio nanopores [67]. For the purpose of this simulation, "ideal" ALD was assumed, where one monolayer of film is conformally deposited per cycle and ignores nucleation delays potentially present during the initial cycles of $TiO_2$ ALD on a removed PAA surface [105]. Instead it used experimentally determined growth rates and assumed that for each cycle the entire surface will be conformally coated with a specific amount of material given by the growth rate for the specified ALD process. The 2D cross-section schematic in Figure 28 depicts the step-by-step simulation sequence for a single ALD cycle. Starting with five equally spaced points on the initial surface (Figure 28a), surface normals were determined (Figure 28b). New data points were placed along each surface normal at a distance specified by the growth rate of the ALD process being simulated (Figure 27b). The new data points were no longer equally spaced along the x-axis; therefore, they were best fit with a new line (Figure 28c). A new set of equally spaced data points were created and placed along the best fit line, ultimately, creating the new surface (Figure 28d).

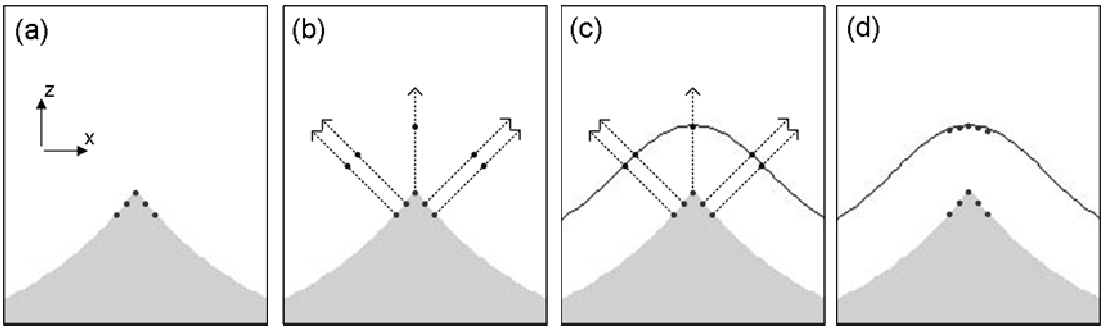


**Figure 28. Geometric 3D extrusion model: (a) five equally spaced data points on the surface of a sharp peak. (b) surface normals are projected out and the data points for the new surface are placed along them using the prescribed growth rate; (c) the new data is fit with a "best fit" line; (d) the "best fit" line is used to generate more data which is equally spaced in the x-direction.**

The model described above used an initial surface prepared using oxalic acid and therefore, cannot be directly compared with experimental results on a template prepared using phosphoric acid at 160 V. However, a similar scaling factor, k, used to compare film thicknesses from different templates can be used to compare the experimental results with the simulation, where $D_{int}$ is 450 nm and $D_{int}^{o} = D_{sim} = 105$ nm. Top view SEM images (Figure 29a-d) and top view simulation results (Figure 29e-h) were compared illustrating the surface evolution of ALD on a scalloped Al surface mirrors what is seen in the extruded surface simulation.

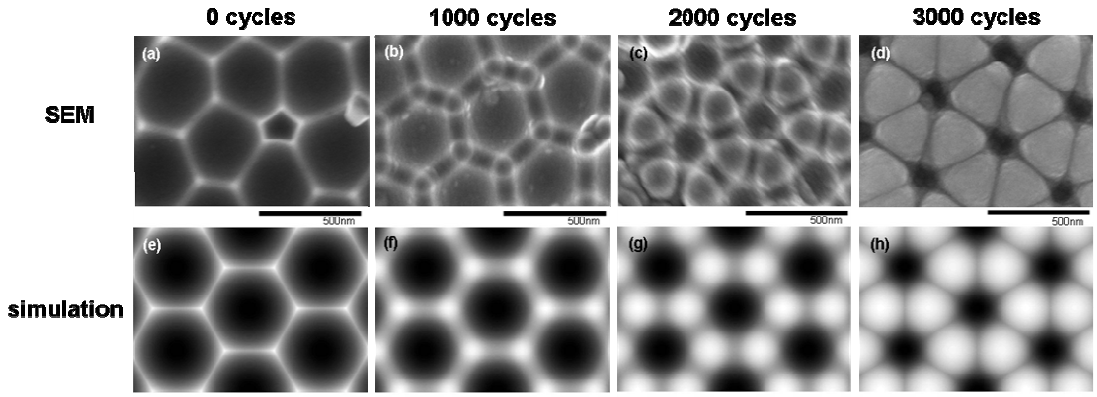


**Figure 29. (a-d) Scalloped Al surface imaged in SEM after TiO2 ALD deposition of 0 cycles, 1000 cycles (~55nm), 2000 cycles (~110nm), 3000 cycles (~165nm); (e-h) simulation of surface evolution by extruding a model of the initial surface at same rate as the deposition per cycle for ALD TiO2.**

Cross-sectional view SEM images along the [111] direction of a scalloped Al surface show three discrete 1000 cycle $TiO_2$ ALD films deposited one on top of another (Figure 30a). Each film set displays a distinct interface where the surface was exposed to air for ex-situ characterization and indicates the presence of surface contamination. As deposition continued, films took on the form of the underlying film's surface eventually creating a rounded knoll atop the initial peak in the Al template's surface signifying there was no substantial topography-induced nucleation. Top down and cross-sectional profiles along the [111] and [121] directions of the 3D model (Figure 30b) reemphasize that ALD deposits in a conformal manner, and that the formation of triangular islands seen in both SEM images and the 3D model is an artifact of the underlying surface and not due to nucleation and growth resonating from the tips of the sharp peaks.

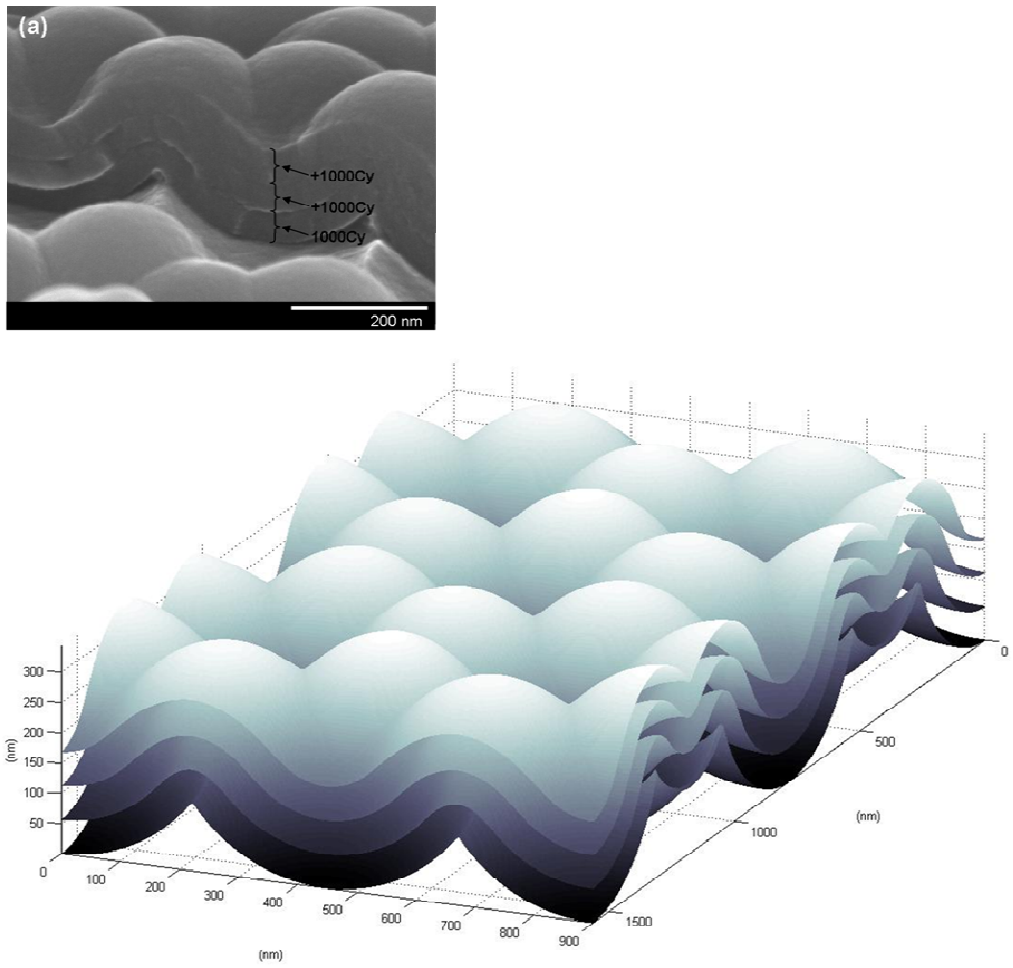


**Figure 30. Cross-sectional surface profiles as a function of film thickness: (a) SEM image of three discontinuous 1000 cycle TiO2 ALD films along the 111 direction of a scalloped Al surface and (b) modeled profiles of TiO2 ALD films along the 111 and 121 directions of a scalloped Al surface.**

Surface area plays an integral part in the design and nanofabrication of next generation energy devices such as MIM nanocapacitors. Matlab® simulations developed by Dr. Perez were used to estimate the change in surface area as a function of film

thickness. The surface area was estimated by summing the areas of all the quadrilaterals that comprise the modeled surface as defined by the X, Y, Z coordinate data. The planar equivalent area is the 2D surface equivalence to the area projected onto the XY plane from the 3D model. From these estimations the initial surface of a template formed in oxalic acid was estimated to have a 30% larger area than its planar equivalent. Templates formed in phosphoric acid would have smaller surface areas due to larger interpore spacings, meaning there are fewer peaks for the same planar area used above. Starting with the initial surface of the scalloped Al template an ALD simulation was performed for 1000 cycles with a growth rate of 0.1 nm/cycle. The normalized surface area (the estimated surface area divided by the planar equivalent surface area) as a function of ALD film thickness was plotted with corresponding 3D representations of the evolving surface profile (Figure 31).

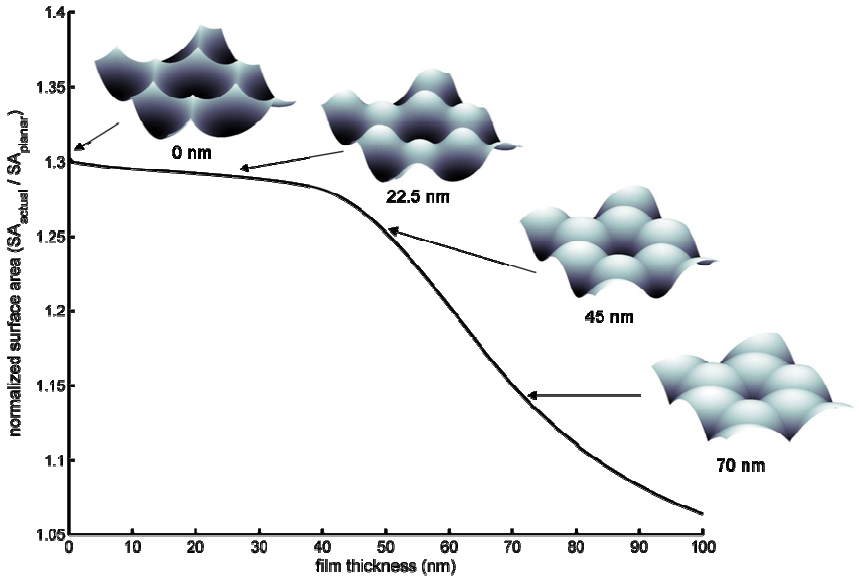


**Figure 31. Normalized surface area as a function of ALD film thickness.**

As the deposition proceeds the normalized surface does not change appreciably until after ~45 nm. After 45 nm of film growth, the normalized surface area asymptotically decays towards a limiting value of 1 implying that the surface has been effectively "planarized". The shoulder at 45 nm seems to coincide with the appearance of lines in the film where film growth fronts have started to merge along the [111] direction of the hexagonal scalloped cell, see Figure 31. This is the moment at which the curvature of the saddle points between the peaks in the scalloped surface is completely inverted by the continued extrusion of the ALD deposition over the sharp peaks. Further deposition results in the extension of these lines towards the center of the scallops further unifying the surface.

## 3.5 Conclusion

$TiO_2$ ALD films were deposited on a highly scalloped Al surface to demonstrate the ability of ALD to provide exceedingly conformal films over a complex topography of a template's initial surface. SEM images and AFM scans reveal the progression of triangular surface profiles that change with ALD layer thickness, influenced by the way ALD conformally coats the underlying topography, and further emphasizing that ALD nucleation is rather insensitive to the surface topography at least for the experimental process chemistry investigated here.

We demonstrated the usefulness of a simple geometric 3D extrusion model to simulate the evolution of ALD films' surface profiles as they conformally coat the complex surface topography of a modeled scalloped Al surface. The scalloped Al surface was modeled and calibrated using dimensions extracted from SEM and AFM scans. The surface was then extruded in a stepwise manner using experimentally obtained growth

rates of the particular ALD chemistry being simulated. The model illustrates how conformal ALD films cause the surface topography to change with each deposited layer, ultimately leading to a decrease in surface area as a function of film thickness. Results from this model and experimental data are in excellent agreement, leading to the conclusion that no nucleation related effects were observed and the resulting triangular pattern is an artifact of the underlying textured Al surface.

This work illustrates the benefits of ALD to conformally coat and manipulate surface topographies in which sharp asperities or nano-roughness could potentially limit device performance. Ultimately this work will play an important role in the design and nanofabrication of devices which exploit nano-processes such as PAA and ALD.

# Chapter 4 : $TiO_2$ ALD Thin Film Growth Behavior Across 2D Planar Wafers Using TTIP and Ozone

This chapter discusses the critical role of interdependent process parameters, such as temperature, dose, surface residence time, and purge time, have on one another as the process window for $TiO_2$ ALD thin films based on the precursors titanium tetraisopropoxide (TTIP) and ozone is determined across planar substrates. As with any deposition technique, determining a process window of parameters is critical when optimizing a new ALD process. This usually incorporates a limited number of deposition experiments combined with ex-situ thickness and uniformity measurements. In the case of ALD, an effective regime is typically indicated by the self-limiting properties of the ALD precursors thus leading to a constant thickness per ALD cycle. This behavior is confirmed by wafer-scale measurements of across-wafer thickness and uniformity. As seen in Chapter 1, the ALD process space includes many parameters that can influence the growth behavior of a film including dose, surface residence time, purge time, process pressure and temperature. Even when limiting ourselves to the most obvious parameters, the task of finding an optimal process recipe can prove challenging.

## 4.1 Introduction

Titanium dioxide ($TiO_2$) has been extensively studied due to its versatile chemical and physical attributes for a wide range of applications as a thin film and a bulk material. Titania's high refractive index, ranging from 2.2-2.6 depending on the deposition method used, makes it a common component in optical filters and coatings.[33, 106] Due to its good transmission in the visible and near infra-red regions, $TiO_2$ is a leading photocatalyst and serves as a critical component in emerging photovoltaic technologies, as well as in photonic crystal waveguides.[16, 33, 107] $TiO_2$ also exhibits some very attractive electrical properties in terms of it high dielectric constant of 40-110, making it a highly sought after candidate for electrostatic nanocapacitors, DRAM, and thin-film transistor applications.[8, 14, 48, 106, 108] The main limitation in using $TiO_2$ for electrical applications is its high leakage current caused by oxygen deficiencies in the material.[14, 106]

A variety of thin film deposition techniques have been used to deposit $TiO_2$, including chemical vapor deposition (CVD)[55], sputtering[109], plasma-enhanced CVD (PECVD)[110, 111], and atomic layer deposition (ALD)[14, 104, 112-114]. ALD has attracted widespread attention on account of its excellent atomic level thickness control over large surface areas with unprecedented uniformity and conformality. The ALD process is a gas phase deposition technique which relies on self-limiting chemisorbed surface reactions through the employment of two alternating reactant precursor exposures separated by intermediate purge steps in order to build films atomic layer by layer. The digital introduction of precursors helps diminish gas-phase particles that sometimes

plague CVD processes in order to create thin, continuous, pin-hole free films. However the optimization of ALD process recipes is often challenging as interdependent variables, such as dose, surface residence time, purge time, temperature or pressure, must be optimized for a given reactor design and chemistry.

Precursor chemistries play an important role in ALD in that they must be volatile, yet thermally stable.[4] A wide variety of precursors have been employed for the deposition of $TiO_2$. Commonly used Ti precursors are halides, alkyl amides, or alkoxides, such as $TiCl_4$, tetrakis(dimethylamino) titanium ($Ti[N(CH_3)_2]_4$, TDMAT), titanium tetraisopropoxide ($Ti[OCH(CH_3)_2]_4$, TTIP), respectively.[104-106] Each precursor group has their limitations; halides produce HCl as a corrosive by-product provoking etching of the films or the reactor and the organometallic precursors tend to decompose at temperatures greater than 300 $^oC$ leading to parasitic CVD-like reactions.[4] The most common oxidizer used for the deposition of $TiO_2$ is water, but hydrogen peroxide, molecular oxygen, and oxygen plasma have also been used.[57, 104, 105, 112, 113, 115] The push to find high-k dielectric materials with low leakage current has lead researchers to investigate ozone ($O_3$) as an alternative to water as an oxidizing agent as it reduces the incorporation of impurities, such as hydroxyl ions ($OH^-$).[116-118] $O_3$ is a strong oxidizing agent and is highly volatile allowing for lower doses, lower deposition temperatures, and unlike water, physisorption on the surface is not a problem allowing for shorter purge times.[56, 117] However, despite the interest in $O_3$ as an ALD oxygen source, the surface reaction mechanisms are not well understood. In $H_2O$ and $O_2$ plasma-based ALD processes, hydroxyl groups are generally considered the reactive sites for the chemisorption of the metal precursor. However, during the ALD of $TiO_2$ from

TTIP and $O_3$, surface carbonates have been identified as the reactive sites for TTIP chemisorption.[56]

The self-limiting behavior of an ALD reactant depends on many factors, such as process temperature, reactant dose, surface residence time, purge time, process pressure, etc. However, thus far, only a small set of ALD processes have been explored in order to understand the detailed relation between process parameters and their surface reaction mechanisms that happen during deposition. It is generally known that ALD is a thermally activated process, where lower temperatures usually result in the use of higher reactant doses in order to achieve self-limiting growth; however, this leads to longer surface residence times.[65] The reactant dose (Pt) is defined as the partial pressure of the precursor times the exposure time. Where the partial pressure of a reactant is determined by how many molecules of a precursor are introduced into the system and the exposure time is the amount of time needed to supply a saturating dose (S) to the surface.[66] Conventional methods to increase exposure doses are typically done by extending the precursor exposure times, therefore, allowing more time for molecules to react and saturate the surface.[66, 67] However, longer pulse times can lead to low throughput. As seen in work by Li [65], it was recognized that higher process pressures resulted in higher surface residence times and had considerable influence on film growth rates. The surface residence time is how long reactants remain exposed to a surface before being pumped away to the exhaust and is based on the partial pressure of a reactant within the system and the temperature of the reaction chamber. Therefore, this chapter investigates the role of key process parameters such as temperature, reactant dose, surface residence time and purge time on the growth behavior of $TiO_2$ ALD thin

films when using TTIP and ozone as the metal and oxidizing precursors, respectively. We use a novel scheme to introduce reactants into the reaction chamber by breaking up the reactant dose and introducing it as a set of μpulses in parallel or in series.

## 4.2 Experimental Setup

High-k dielectric titanium dioxide ($TiO_2$) films were deposited in a custom built stainless steel ultra-high vacuum (UHV) cross-flow wafer scale ALD reactor using alternating reactant exposures of TTIP (99.99% grade, Air Liquide) and ozone ($O_3$). A 0.1L mini-reactor is embedded in the UHV process chamber equipped with a 100 mm substrate heater and a pneumatically actuated cap. Precursors and nitrogen gases were introduced and exhausted through 2 opposing slits positioned 3 mm above the wafer. The mini-reactor was operated at 100 mTorr and the substrate heater was maintained at 200 °C. The substrates used were 100 mm Si (100) test wafers cleaned in a 1% hydrofluoric acid, followed by a DI rinse and dried via $N_2$ gas.

Liquid titanium tetraisopropoxide (TTIP) was used as the titanium metal precursor. The TTIP precursor container was heated to 58 $^{o}$C in order to achieve a vapor pressure of ~0.6 Torr. In order to achieve reproducible doses of the TTIP precursor, fast action pneumatic ALD valves were implemented on the inlet and outlet of a temperature-controlled 20 mL volume monitored by a 0-10 Torr capacitance manometer pressure gauge. TTIP doses were controlled by timing the opening of these valves. The inlet valve to the volume was opened for 1 s in order to fill the volume to the vapor pressure of the TTIP precursor. Upon reaching a given time setpoint, the inlet valve between the precursor source and the volume was closed and the gases were released into the chamber

for an exposure time of 0.3 s. By monitoring the minimal and maximal pressures during each cycle, the number of molecules entering the system were approximated from the ideal gas law, pV=nkT (where p is the pressure, V the volume, n the number of μmols, k the Boltzmann's constant, and T the absolute temperature).

Ozone was obtained by flowing 200 sccm of $O_2$ (Grade 5, Praxair) into an MKS Instruments $O_3$mega ozone generator. The flow produced a 20psig pressure in the single electrical discharge cell. At 100% power, the ozone concentration at the outlet was up to 20 wt% (300 g/m$^3$) with the balance being $O_2$. Due to the high flow and high pressure required for the operation of the $O_3$mega$^{TM}$ a different control scheme of the ozone exposure was necessary. The $O_2/O_3$ mixture was flowed continuously into an HA-series catalytic ozone destruct from Ozone Engineering to deactivate ozone into oxygen. Therefore, only a fraction of the total flow was pulsed into the reactor using a Swagelok medium flow metering valve in series with a fast action pneumatic ALD valve. For a given needle valve conductance, the number of μmols of ozone was determined by integrating the pressure peaks measured in the mini-reactor for different exposure times and comparing them to integrated peaks from known doses determined through pressure measurements in an attached trimethylaluminum vessel.

Wafer maps of film thicknesses and refractive indexes were obtained using a Sopra GES5 spectroscopic ellipsometer integrated with an automated xy stage and a 75W high intensity Xenon arc lamp to obtain a continuous spectrum of light from 2.0-6.0 eV. Thickness profiles were taken at 5 equidistant points across the wafer in the direction of the cross-flow, with the first point being closest to the gas inlet and the last point being

closest to the exhaust outlet. The percentage of non-uniformity within a wafer was determined by the ratio of the standard deviation over the average film thickness ($\sigma/\mu$).

## 4.3 Results

In order to investigate the influence of substrate temperature on the deposition of $TiO_2$ ALD temperatures were varied from 160 °C to 200 °C with a viscous flow regime of 100 mTorr. TTIP doses of 0.24 Torr-sec and over-saturating exposures of ozone, 1.3 Torr-sec, were introduced into the system followed by an evacuation purge of 20 sec for each precursor. Figure 32 displays the relationship between film thicknesses and the changing number of deposited cycles for two different temperatures, 160 °C and 200 °C. The plot demonstrates fairly good thickness control of the titania process at a processing temperature of 200 °C, where the slope is the growth rate per cycle and is equivalent to ~0.65 Å/cycle. Films were deposited with the same conditions for 150 cycles at a substrate temperature of 250 °C and were measured to have a growth rate of ~0.66 Å/cycle. However, for the 160 °C case, a growth rate of only ~ 0.2 Å/cycle was achieved. The term ALD window usually refers to the temperature range in which the growth rate is constant.[4] Lower growth rates could be attributed to the substrate temperature not being high enough to overcome the activation energy required for a TTIP molecule to chemisorb on the surface. Therefore the optimal temperature window for $TiO_2$ ALD using TTIP and ozone was deemed to be between 200 °C and 250°C. However, temperatures higher than 250 °C where not investigated due to the decomposition temperature of TTIP to be reportedly around 275 °C [105, 112, 113].

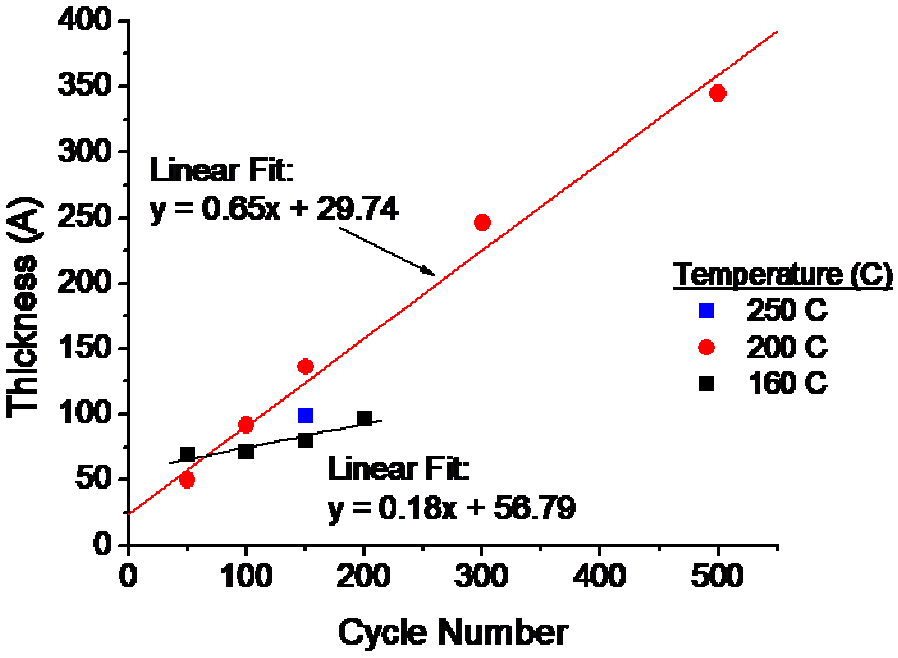


**Figure 32. Film thicknesses as a function of number of ALD cycles as determined by ellipsometry for two different reaction temperature, 160 °C and 200 °C. Linear regression demonstrates a growth rate of ~0.65 Å/cycle for the 200 °C case and that the growth never really took off for the 160 °C case.**

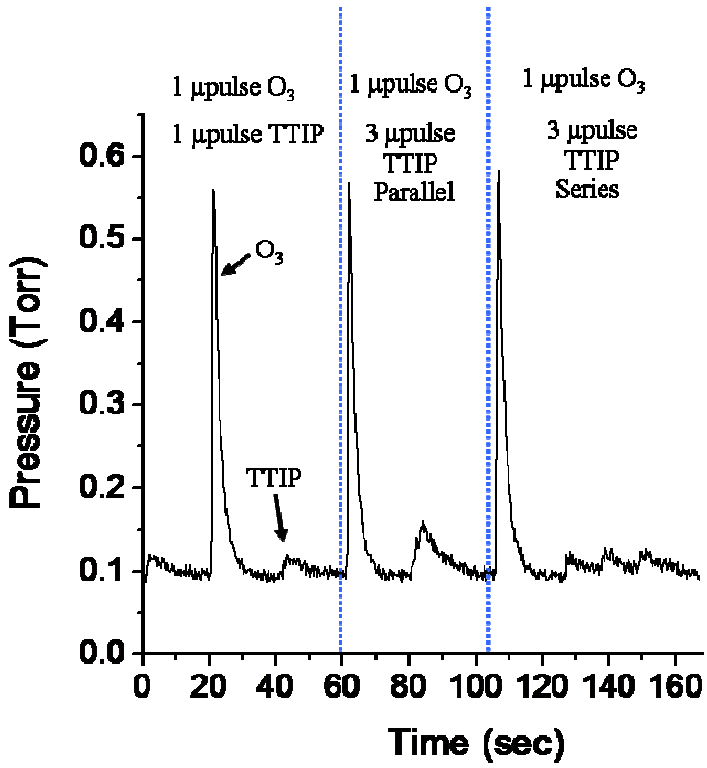


**Figure 33. Representation of pressure within the mini-reactor during three different runs: (a) single µpulse of TTIP, (b) 3 µpulses of TTIP in parallel and (c) 3 µpulses of TTIP in series.**

In order, to illustrate the effect of the process parameters dose and surface residence times of a reactant on the deposition rates of $TiO_2$ thin films across planar 100 mm Si wafers a set of experiments were designed using a novel scheme to introduce the TTIP precursor into the mini-reactor chamber. Figure 33 displays alternating exposures of an over-dosed µpulse of ozone (1.3 Torr-sec) and three different scenarios for introducing TTIP doses: a single µpulse, µpulses in parallel, and µpulses in series. Figure 33a demonstrates the first scenario of a single µpulse of TTIP being flowed into the mini-reactor followed by a 20 sec purge before introducing the ozone precursor and is

monitored by a down stream pressure gauge. By subtracting the base pressure and integrating under the curve the dose of 1 μpulse of TTIP was determined to be 0.24 Torr-sec. The surface residence time was determined by monitoring how long it took for the increased process pressure during a precurosor half-cycle to return to the base pressure of 100 mTorr. Therefore, surface residence time of the TTIP precursor was determined to be ~10 sec and the ozone surface residence time was determined to be ~ 14 sec. A 20 sec purge was deemed sufficient for both precursors to completely evacuate the reactor.

We refer to exposures introducing TTIP μpulses as "in parallel" if they comprise of a group of consecutive rapid fire single μpulses, meaning that the μpulses are spaced so closely in time that the 2$^{nd}$ μpulse subsequent in the sequence occurs well before a residence delay is observed for the previous μpulse, i.e. the "in parallel" case behaves like a single bigger pulse. This allows for higher TTIP doses by increasing the partial pressure, but also increases the TTIP surface residence time within the mini-reactor, as seen in Figure 33b for 3 μpulses again followed by a 20 sec purge. It was noticed that the TTIP surface residence time for doses introduced in parallel push the limits of the 20 sec purge by barely having sufficient time to return to the base pressure before the ozone μpulse is introduced. The third scenario introduces TTIP exposures as "in series" which are a combination of single μpulses separated by a 10 sec delay allowing the pressure between each μpulse to head towards the base pressure, as seen in Figure 33c for 3 μpulses and a 20 sec purge immediately after the introduction of the last μpulse. After each μpulse the pressure within the chamber heads towards the base pressure before the next μpulse is introduced, allowing for higher doses, but without increasing the surface

residence time of the precursor within the system. Therefore, the TTIP surface residence time will be consistent with the single μpulse case and ensures that the 20 sec purge is adequate before introducing the ozone μpulse.

One of the hallmarks of the ALD process is the self-limiting surface chemistry, meaning that an increased dose should still yield a consistent film thickness. However, growth rates are not only a function of the dose, but are also dependent on the surface residence time of the precursor within the chamber. The reported density of $TiO_2$ ALD films is 3.84 $gcm^{-3}$ [119] and was used to calculate an ideal monolayer of film thickness as $d = \rho^{-1/3}$ ~3.3Å.[120] Amorphous $TiO_2$ ALD films were deposited using an over-saturating dose of ozone with one of the three dosing schemes described above. A precursor's partial pressure within a volume is proportional to the number of molecules with in said volume; therefore, as the number of μpulses increase, the partial pressure also increases, thus creating a direct relationship between the dose and the number of molecules in the system. Figure 34 demonstrates the relationship between a film's growth rate as a function of the number of molecules associated with the three dosing schemes used to introduce TTIP into the reaction chamber. The plot demonstrates that increased doses lead to higher growth rates and subsequent film densities. However, as discussed earlier, doses introduced in parallel will have higher surface residence times than those introduced in series. Although the same number of TTIP molecules entered the system for each scheme, the increased surface residence times led to higher growth rates and increased film densities, again exemplifying the importance of a precursor's surface residence time. It can be believed that the increase in dose leads to an over-

saturation of precursor within the reaction chamber. Therefore, when a delay between μpulses is introduced as is the case with the "in series" scheme, the delay behaves as an intermediate purge step, allowing some of the excessive molecules to purge away, as well as, desorb any physisorbed molecules. The plot also demonstrates that doses introduced in series have higher growth rates than the single μpulse case even though they have similar surface residence times within the process chamber. This goes against the idea that ALD is self-limiting and results in much more complex mechanisms than originally thought.

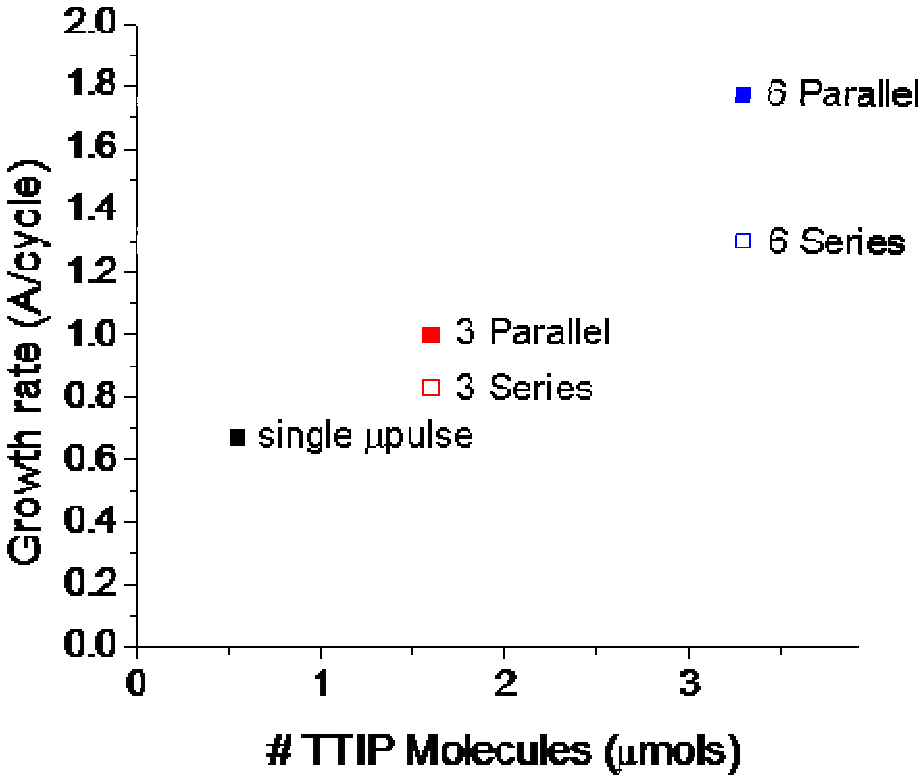


**Figure 34. Growth rate as a function of the number of TTIP molecules when doses are introduced in parallel or in series. Demonstrates that an increase in molecules leads to higher growth rates and subsequent film densities, however, TTIP doses introduced in series have lower growth rates and densities as opposed to their in parallel counterparts.**

Purge time is a crucial parameter in the ALD process sequence. Inadequate purge times to fully exhaust any unreacted precursors from the reactor before the introduction of the next precursor will result in an overlap of the two precursors, creating parasitic CVD-like reactions leading to higher growth rates. However, decreasing growth rates can indicate desorption of adsorbed species during extended purges contradicting the fundamental requirement that a chemisorbed reaction is irreversible. $TiO_2$ films were deposited for 250 cycles at a substrate temperature of 200 °C using two different TTIP dosing schemes: the single μpulse (0.24 Torr-sec) and the 3 μpulses in parallel (0.56 Torr-sec). Both cases used an over-saturating dose of ozone (1.3 Torr-sec) and a subsequent 20 sec purge. Growth rates plotted as a function of TTIP purge time exhibit the self-limiting behavior typical of a $TiO_2$ ALD deposition (Figure 35). While a 10 sec purge seemed adequate to deposit self-limiting films for the single μpulse case, it does not appear to be sufficient for the dose of 3 μpulses in parallel. This is due to the fact that the surface residence time of the TTIP molecules during the 3 μpulse case exceeds the 10 sec purge time used; therefore creating a parasitic CVD reaction when the ozone pulse is introduced. However, as purge times are increased, the saturating behavior for both cases demonstrates that the purge time did not affect the growth rate indicating that the higher growth rate was not due to multi-layer physisorbed molecules or parasitic CVD-like reactions and the origin of the higher growth rates can be attributed to a density increase of surface carbonates or hydroxyl groups as a result of higher TTIP doses and surface residence times.

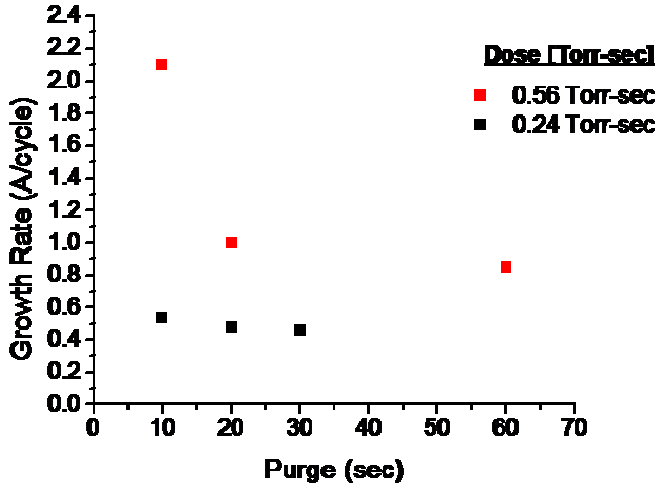


**Figure 35. Growth rates as a function of TTIP purge time for two different TTIP doses and an over-saturating dose of ozone (1.3 Torr-sec) for 250 cycles at a reaction temperature of 200 °C.**

Across wafer uniformity is also a useful process metric to evaluate the self-limiting behavior of ALD. $TiO_2$ ALD films were deposited across 100 mm wafers for 250 cycles using an over-saturating dose of ozone and one of the three dosing schemes for TTIP at a process temperature of 200 °C. Figure 36 displays highly uniform film growth rates associated with the three different TTIP dosing schemes as a function of position across a wafer, with 0 mm being closest to the inlet and 70 mm being closest to the exhaust. The single μpulse case displays the best film uniformity of 99.6% (standard deviation, 1 sigma) where the uniformity only degrades by 2% as the worst case associated with the "in parallel" cases. These results support the idea that film deposition was not influenced by parasitic CVD-like reactions and implies that all of the active surface sites are reacted.

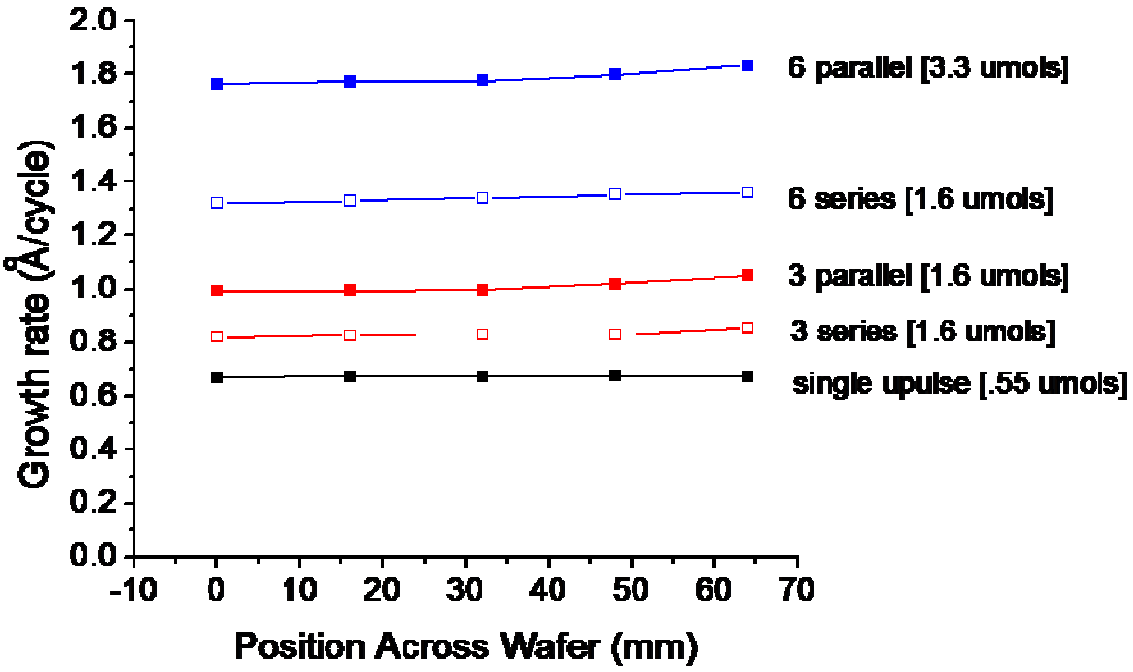


**Figure 36. Growth rate profiles of $TiO_2$ ALD films after 250 cycles deposited on 100mm wafers.**

## 4.4 Discussion

It is widely accepted that in $H_2O$ and $O_2$-plasma based ALD processes, hydroxyl groups play an important role as the reactive sites for the chemisorption of the metal precursor, including TTIP.[56, 121] Conversely, Rai et al reported that with the use of ozone as the oxidizing agent, the dominating reactive species for TTIP chemisorption were surface carbonates.[56] When ozone is used as an oxidizer, the reaction goes through a combustion process producing $CO_2$ and $H_2O$ as by-products, leaving surface carbonates as the reactive sites for the TTIP molecules.[56, 122, 123] However, if purge times are not deemed long enough after an ozone dose, physisorbed, i.e., weakly bound

molecules through Van-der Wall forces, water molecules become a source of hydroxyls, therefore, partially re-hydroxylating the surface for a TTIP molecule.[47] Although, the use of ozone greatly reduces the presences of $H_2O$ it does not eliminate it therefore creating two competing reaction pathways during the $TiO_2$ ALD process. Reactions with surface carbonates are deemed 1$^{st}$ order reactions, where reactions with surface –OH groups are considered secondary reactions. However, the growth rates associated with ozone based $TiO_2$ ALD are comparable to $H_2O$ and $O_2$-plasma assisted works, suggesting that the increase in growth rates during the ALD processes are possibly associated with the method at which TTIP doses are introduced into the system.[54, 56, 57, 124, 125]

Ideally, the self-limiting surface adsorption and reaction process of ALD should garner one monolayer of film thickness per cycle, provided sufficient doses and purge times are supplied. However, a perfect layer by layer growth does not always occur, and the growth behavior for which it does is deemed the "ideal" case.[126] Therefore, most ALD processes deposit less than a monolayer of film and are dubbed "non-ideal". Consequently, the non-ideal behavior observed during $TiO_2$ ALD using TTIP and ozone is not surprising due to the large steric hindrance associated with the large size of the allkoxide ligands of the TTIP molecule. Figure 37 is a schematic of the TTIP molecule and Table 2 is its associated bond lengths and angles.[55] From the associated bond lengths and angles the radius of the TTIP molecule was calculated as 5.1 Å, which is much larger than the 3.3 Å associated with one monolayer of $TiO_2$ film.

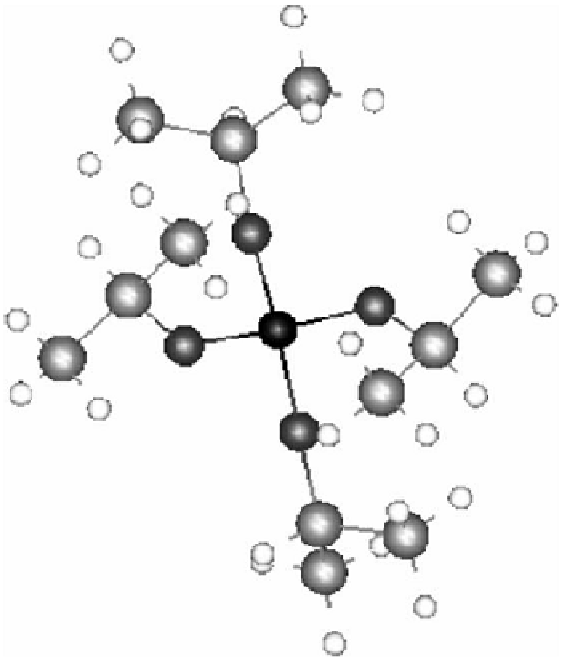

**Figure 37. Schematic of the structures of a free TTIP molecule, where the black ball is the Ti atom, the dark grey balls are oxygen, the light grey balls are carbon, and the white balls are hydrogen. Their associated bond lengths and angles are reported in Table 3.[55]**

**Table 2. Bond lengths (Å) and angles (degrees) associated with the titanium tetraisopropoxide molecule shown in Figure 38.[55]**

| Molecular parameter | Value |
|---|---|
| d (C-O) | 1.43 |
| d (C-H) | 1.11 |
| d (Ti-O) | 1.82 |
| d (C-C) | 1.52 |
| < (O-Ti-O) | 112.9 |
| < (Ti-O-C) | 144.7 |
| < (O-C-C) | 110.8 |
| < (C-C-H) | 110.7 |
| < (C-C-C) | 111.7 |
| < (O-C-H) | 106.1 |
| < (O-Ti-O-O), torsion | 123.4 |
| < (O-C-C-C), torsion | 122.9 |

Through investigative studies by Rai, it was determined that $H_2O$ is a by-product during the TTIP ligand exchange during $TiO_2$ ALD.[56] This has lead to the use of TTIP as both the metal containing and oxidizing precursor at elevated temperatures nearing its decomposition temperature.[127] Due to this innate behavior of the TTIP precursor, the increase in surface residence time of the TTIP molecule is known to have a significant effect on the extent of decomposition and formation of excessive $H_2O$ during the TTIP half cycle.[128, 129] Therefore, the use of doses in parallel will increase the $H_2O$ production and lead to unexpected secondary reactions leading to higher growth rates. However, when doses are introduced in series, the $H_2O$ production is significantly decreased, leading to lower growth rates than the parallel case. Nevertheless growth rates were still higher than those of the single μpulse case. This can be attributed to the extended purge during the TTIP half cycle due to the 10 sec delays between μpulses, where excessive $H_2O$ molecules produced during the ligand exchange will have less opportunity to create secondary reactions. Although all films demonstrated an increase in growth rate, none exceed the deposition of a full monolayer of $TiO_2$ film growth.

## 4.5 Conclusion

The growth behavior of $TiO_2$ ALD thin films have been investigated as a function of key interdependent ALD process parameters, such as temperature, reactant dose, surface residence time, and purge time. It was determined that $TiO_2$ ALD films deposited using TTIP and ozone as precursors are thermally activated between 200 °C and 250 °C and display good linearity between film thicknesses and cycle numbers. A unique dosing scheme to introduce precursors was developed in order to examine the relationship between a precursor's partial pressure and its surface residence time. It was determined that growth rates and subsequent film densities are highly dependent upon the surface residence time of a precursor. It was proposed that the use of TTIP and ozone as precursors leads to a more complex ALD reaction mechanism, where the production of $H_2O$ was assumed to be a by-product during the TTIP half-cycle leading to secondary reaction mechanisms and higher growth rates. Longer purge times and excellent across wafer uniformity ascertained that secondary reactions are the reason for higher growth rates and are not associated with multilayer physisorption or parasitic CVD-like reactions.

# Chapter 5 : Metrology of ALD Conformality in 3D Ultra-high Aspect Ratio Nanopores

This chapter details a method to extract film thicknesses and subsequent conformality of deposited ALD films in ultra-high aspect ratio nanopores with the use of a chemical analysis tool. $TiO_2$ ALD films were deposited in porous AAO membranes with an aspect ratio of 111. EDS line scans were taken across the cleaved interface of the membrane in order to extract Ti intensity profiles as a function of pore depth. A relationship between the Ti intensity profiles and film thicknesses was determined through a cylindrical assumption and planar film thicknesses measured by ellipsometry. Film thickness profiles demonstrate a strong gradient down the length of the nanopore and are in strong agreement with direct measurements of wall thicknesses measured from corresponding released nanotubes imaged via TEM.

## 5.1 Introduction

ALD's ability to deposit conformal thin films in ultra-high aspect ratio structures makes a desirable technique used in the design and fabrication of nanotechnology. Traditional techniques used for extracting thin film thickness and conformality within high aspect ratio nanostructures, such as scanning electron microscopy (SEM) and transmission electron microscopy (TEM), usually involve extensive sample preparation, including sample thinning and cross-sectioning which typically takes a lengthy amount of time. Nanopores present a considerable dilemma in terms of cross-sectioning due to their one dimensional shape and small diameters. Ideally, the cross-section of a nanopore should be cut directly along the center axis in order to reveal the thin film composing the nanotube within. When pores are cut accurately film thicknesses can be measured along the pore side walls down the length of the pore. However, if it is not cut accurately along the pore axis film thickness measurements can be skewed as a result of the pores' cylindrical character, meaning film thicknesses can appear larger than they actually are.

Previous studies on conformality of thin films within high aspect ratio nanopores consist of cutting a bulk nanoporous film parallel to the nanopores' long axis and scavenging the cross-sectioned interface in order to find pores that have been cleaved along their specific axis. Gordon et al. used a dual-beam SEM-FIB in order to cleave and image a thin film deposited inside elliptical pores etched deep into a silicon wafer.[66] The SEM-FIB cleaves the silicon along the natural crystallographic axis and allows for continuous cutting without having to remove the sample. Elam et al. imaged a thin film deposited within a porous anodic aluminum oxide (AAO) by embedding the film in

epoxy and perpendicularly polishing the sample along the nanoporous axis. This allows for top down images of the deposited in pores to be accurately measured at different depths within the sample.[67] However, in order to obtain a highly resolved thickness profile down the length of a high aspect ratio nanopore would require several iterations of polishing and SEM imaging for one sample. Employing traditional SEM cross-sectioning techniques to characterize thin film conformality is possible, but proves to be time consuming and highly dependent upon accurate cleaving along a structures central axis.

Although SEM provides a direct observation of ALD films within nanopores allowing for qualitative assessment of ALD conformality, quantifying film thicknesses and subsequent conformality has proven to be difficult. In combination with SEM imaging Elam et al. employed the use of electron probe micro-analysis (EPMA) in order to create zinc compositional profiles as a function of pore depth of a cross-sectioned ZnO ALD coated porous AAO membrane. Although this work demonstrates the deposition behavior of various process parameters by calculating the relative concentration of Zn down the length of the nanopore it does not provide an actual thickness measurement.

Perez et al. demonstrated a methodology to experimentally determine thin film thicknesses and subsequent conformality using template-synthesized nanotubes fabricated by ALD within a porous AAO template.[44] The novelty of using AAO is that once thin films are deposited within the pores the template is removed by a dissolution process, releasing cylindrical nanotubes comprised of the ALD thin films. Released nanotubes were then imaged using bright-field TEM and then analyzed using an image

analysis program based on a simple geometric model and the grey scale contrast of the image. This technique gave direct measurements of film thickness and subsequent conformality of films down the length of a nanopore. However, the shortcoming of this technique is that nanotubes have a tendency to break at various points along the axis making it difficult to locate complete nanotubes. Also, this technique requires very clean sample prep in order to use the image analysis program.

In this chapter, a method is proposed to extract thin film thicknesses and subsequent conformality down the length of an ultra-high aspect ratio nanopore through the use of cross-sectional SEM combined with energy dispersive spectroscopy (EDS) line scans. EDS is a chemical microanalysis technique that detects the energy of x-rays emitted from the sample when the SEM electron beam hits the surface and does not require intensive sample preparation to perform measurements. Film thicknesses were determined through a cylindrical assumption using metal intensity signals measured during EDS line scans and compared to film thicknesses directly measured from the release of ALD based nanotubes from a porous AAO membrane in TEM. Although TEM analysis is a more accurate method of measuring film thicknesses and determining film conformality down the length of a nanopore, the rigid sample preparation and serendipity of finding a full nanotube means a comparable method is necessary.

## 5.2 Materials and Methods

A porous AAO template was synthesized using a two-step anodization method set forth by Masuda.[79] Aluminum foils (99.99%, Alfa Aesar) were electropolished and anodized at 40 V and 10 °C in an electrolytic bath of 0.3M oxalic acid. Foils were

anodized for ~7 hrs during a first anodization in order to produced ordered orthogonal pores with respect to the substrate. The 1st anodized membrane was removed using an aqueous mixture of phosphoric acid (6 wt%) and chromic acid (1.8 wt %), leaving a textured and ordered aluminum surface for the 2nd anodization to initiate from. Foils were anodized for a 2nd time for ~2 hrs 17 min for a pore depth of ~10 μm deep. Pores were widened to ~90 nm using a pore-widening solution of phosphoric acid (0.1M) at 38 °C. Membranes were not removed from the underlying aluminum substrate; therefore, pores were only open on one end.

High-k dielectric $TiO_2$ thin films were deposited by alternating reactant exposures of titanium tetraisopropoxide (TTIP) (99.99%, Air Liquide) as the metal precursor and ozone as the oxidizing agent. The ALD equipment consists of a stainless steel ultra-high vacuum outer chamber with a 100mm mini-capped reactor embedded within. Precursors were introduced through 3 mm slit raised above the wafer in a cross-flow direction and exhausted through an opposing downstream 3 mm slit to a mechanical pump. Porous AAO templates were adhered flat to a 100 mm wafer by silver paint with the open ended pore exposed to precursor flow. Substrate temperatures were maintained at 200 °C and a base pressure of 100 mTorr.

Liquid titanium tetraisopropoxide (TTIP) was held in a temperature controlled vessel heated to 58 $^{o}$C in order to achieve a vapor pressure of ~0.6 Torr. A TTIP dose of 0.47 μmols was fed into the reactor for an exposure time of 0.3 sec followed by a 20 sec evacuation of unreacted precursor and byproducts. Ozone was produced by flowing 200 sccm of $O_2$ through an MKS $O_3$mega ozone generator. An over-dosing exposure of ozone

(1.82 μmols) at a concentration of 300 g/$m^3$ was introduced into the reactor and followed by another 20 sec evacuation step. A growth rate of 0.66 Å/cycle was achieved over 250 cycles and was determined from the films deposited across the Si planar wafers the porous AAO templates were attached to using a Sopra GES5 ellipsometer.

After ALD deposition, a piece of the porous AAO sample was used for TEM analysis. Samples were placed in a 25 wt% phosphoric acid solution for 24 hrs, which dissolved the alumina template thus releasing the $TiO_2$ nanotubes in solution. Nanotubes were filtered using DI water and a drop of solution was placed on a standard holy-carbon TEM grid. TEM studies were performed on a JEOL 2100F microscope with a $LaB_6$ source operated at 200 keV. Images were taken using a post-column Gatan CCD camera and analyzed using ImageJ open source program. Film non-conformality was determined by the [max-min]/[max+min].

The rest of the coated porous AAO sample was used to make cross-sectioned samples for EDS analysis. Samples were epoxied to a small piece of silicon with a notch scribed in the back center pore side down. The backside of the AAO template was scratched to induce etching of the aluminum substrate in a $Cu_2Cl$ solution. Templates were etched with help of a sonicator for approximately 20 min followed by sonicating the sample in isopropanol for an additional 10 min removing any Cu particles left on the surface. Samples were then cleaved using the notch in the back side of the silicon as an initiator. Before EDS measurements were taken samples were coated with a thin film of Au/Pd in order to reduce sample charging during measurements. EDS studies were performed using a Bruker's Quantax micro-analysis system attached to a Hitachi SU-70

high resolution scanning electron microscope operating at a 20 kV accelerating voltage and a magnification of 6K. EDS line scans were performed across the cleaved cross-section of the coated AAO membrane parallel to the nanopores, as seen in Figure 38a, at various stage tilts in order to determine a zero point. Scans consisted of 100 equally spaced point measurements dictated by the position and length of the user drawn EDS line marker.

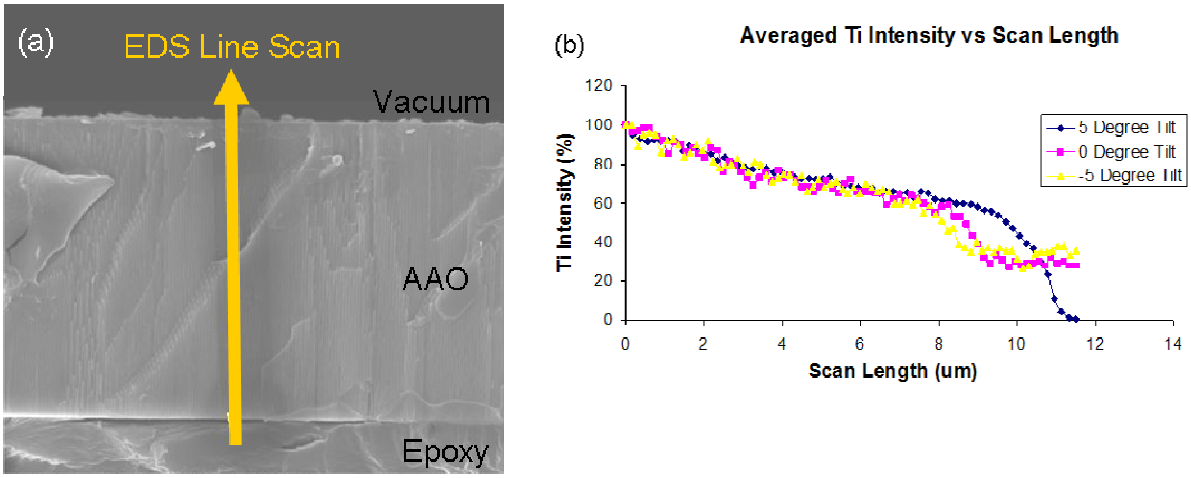


**Figure 38. (a) SEM image displaying a cleaved $TiO_2$ coated AAO template epoxied to a silicon substrate demonstrating the position of an EDS line scan position and (b) the corresponding averaged Ti Intensity curves versus the length of the EDS line scan for the tilts 5, 0, and -5 degrees.**

## 5.3 Results

### 5.3.1 EDS Inferred Thickness

Porous AAO membranes with dimensions of 90 nm in diameter and 10 µm deep, creating an aspect ratio of ~111 were coated with 250 cycles of $TiO_2$ ALD at a deposition temperature of 200 °C. Membranes were attached to silicon chips by firmly pressing the AAO template pore side down into a small dollop of epoxy making sure the epoxy is

thinned under the membrane in order to prevent excessive charging or drifting of the sample during measurements. However, due to uneven pressing of the sample into the epoxy samples could be tilted at various angles due to the amount of epoxy left under the sample. After the aluminum base of the AAO membrane was etched away samples were broken in half exposing a cleaved cross-section of the ALD coated AAO pores as seen in Figure 38a. The SEM image in Figure 38a demonstrates the difficulty found in cleaving a porous AAO membrane as indicated by the many sheared pores across the interface making it nearly impossible to visually measure film thickness down the length of a pore.

Therefore, EDS was used to measure the intensity of Ti atoms as a means to measure the composition of $TiO_2$ down the length of the AAO membrane. Oxygen could not be measured due to the template being comprised of $Al_2O_3$ itself, thus convoluting the O signal from the $TiO_2$ ALD film. EDS line scans approximately 11.5 μm long were placed along the cleaved surface of the AAO membrane parallel to the pores as seen in Figure 38a. Scans were taken starting from slightly below the pore entrance and ending well into the vacuum designated area. However, depending on the tilt of the sample this does not necessarily guarantee the electron beam is entirely off the sample. The electron beam has a plume depth and resolution of 1 μm and for that reason samples were measured at various SEM stage tilts in order to determine a zero point dictating that the beam is no longer measuring the sample. Samples were measured at 5, 0, and -5 degrees, with 0 being the original positioning of the stage. As seen in the graph of Figure 38b, all three tilts display the decreasing intensity of the Ti down the length of the scan, however, scans made at stage tilts 0 and -5 degrees never measure 0% Ti inferring that the beam is

scanning at an angle back into the sample. It is imperative to find the 0% ± 2% in order to determine the Ti intensity at the bottom of the pore without any overlap into vacuum. The electron beam moves in small increments and measures a percentage of Ti relative to the maximum amount of Ti measured in the sample. Therefore, when near the bottom of the pore, the beam scans over part of the sample as well as the vacuum space off the sample. Meaning that when the beam is at a scan location of 10.9 μm the intensity profile is still indicating that Ti is being measured even though the sample is only 10 μm long. However, when samples are tilted due to sample preparation, not only are the scans indicating the beam is measuring more Ti atoms at the bottom of the pore, but the 100% intensity at the top of the pore is skewed as well due to the beam scanning over a larger area coated with 100% $TiO_2$ (ie. the surface). However, the scan made at a 5 degree stage tilt displays 0% Ti at the end of the scan. Therefore, the EDS profile for the length of the AAO membrane can be determined by setting the 100% Ti intensity as the pore entrance and going a length of 10 μm down the scan length to determine where the bottom of the pore is.

In order to extract film thicknesses as a function of pore depth a relationship was devised between the intensity of a specified element measured by EDS and the volume of a nanotube. It was assumed that ALD films deposited within a porous AAO membrane form cylindrical nanotubes and therefore, allowed a cylindrical assumption to be made:

$$I(x) \propto kV(x) \qquad \text{Eq. 1}$$

where, I is the EDS intensity for a specified element, k is a constant, and V is the Volume of a cylinder (Eq. 2) at a given position x down the length of a nanopore (Figure 39a).

$$V(x) = \pi(r_{pore}^2 - r_1(x)^2)L \qquad \text{Eq. 2}$$

Where, $r_{pore}$ is the original radius of the nanopore, $r_1$ is the radius of the nanopore after deposition at a position x down the length, L, of the nanopore. As the electron beam scans the surface of the cleaved interface of the porous AAO it encounter hundreds of nanotubes due to the resolution of the electron beam. Therefore, the model multiplies the number of nanotubes for which the beam scans by the area of the cylinder (Eq. 3), where the number of nanotubes is calculated by the width of the beam, ω, divided by the interpore spacing, $D_{int}$, of the AAO membrane (Eq. 4) (Figure 39b).

$$\frac{V(x)}{L} = N\pi(r_{pore}^2 - r_1(x)^2) \qquad \text{Eq. 3}$$

$$N = \frac{\omega}{D_{\text{int}}} \qquad \text{Eq. 4}$$

Assuming the electron beam to be a cube, the model also takes into consideration the length of the nanopore the electron beam scan at any given time by multiplying the area of the nanotube by the length of the beam, ω, in Eq. 5.

$$\frac{V(x)}{L}\omega = N\pi(r_{pore}^2 - r_1(x)^2)\omega \qquad \text{Eq. 5}$$

By substituting Eq. 5 into Eq. 1 the intensity of an element measured by EDS can be set to the area of the nanotube as a function of position x being measured by a beam of

length, ω (Eq. 6).

$$I(x) \propto k\frac{V(x)}{L}\omega = Nk\pi(r_{pore}^2 - r_1(x)^2)\omega \qquad \text{Eq. 6}$$

In order to extract film thickness as a function of position x, the radius of the nanotube at position x after deposition must be determined (Eq.7).

$$r_1(x) = [r_{pore}^2 - I(x)A_o]^{1/2} \qquad \text{Eq. 7}$$

Where,

$$A_o = \frac{D_{\text{int}}}{k\pi\omega^2} = -\frac{r_1(x)^2 - r_{pore}^2}{I(x)} \qquad \text{Eq. 8}$$

It is known that the film thickness is the difference between $r_{pore}$ and $r_1(x)$ (Eq. 9) (Figure 39c). Therefore, we can determine $A_o$ by using the planar film thickness as measured by ellipsometry to calculate $r_1(0)$.

$$t(x) = r_{pore} - r_1(x) \qquad \text{Eq. 9}$$

By using Eq. 7 in conjunction with Eq. 9, thickness profiles can be extracted for ALD films down the length of a porous AAO membrane by using the I(x) associated with the position within the pore.

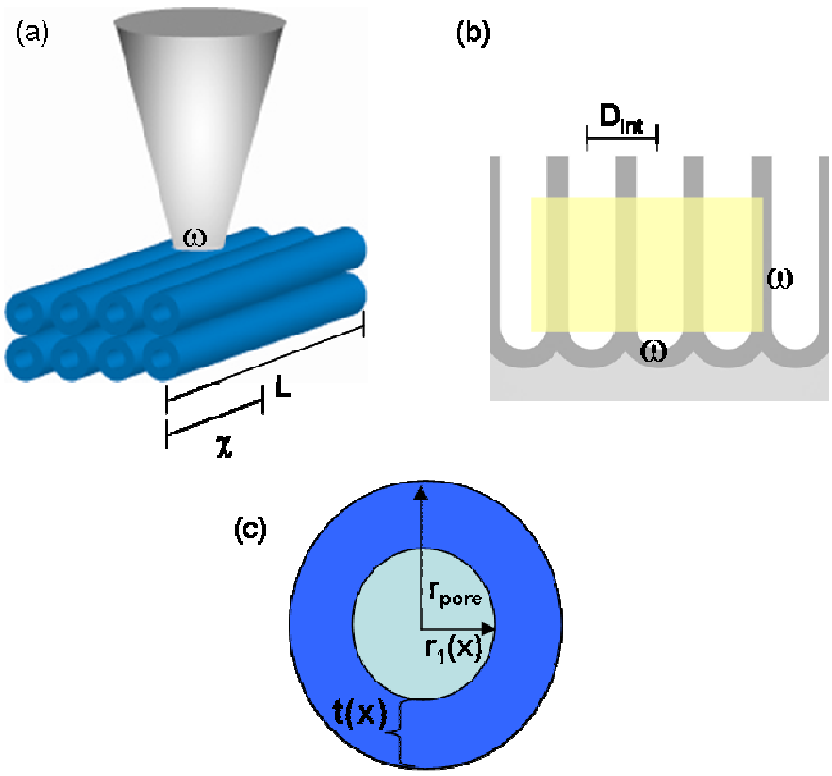


**Figure 39. Schematic of how the EDS inferred thickness method was derived. (a) Demonstrates an electron beam of width ω scans several nanotubes of length (L) at position x. (b) Demonstrates the electron beam of area $\omega^2$ spanning several nanopores within the porous AAO template with an interpore spacing of $D_{int}$. (c) Demonstrates film thickness at position x is a function of the inner radius at position x.**

Pores 90 nm in diameter and 10 μm deep were coated with 250 cycles of $TiO_2$ ALD resulting in a planar film thickness of 16.6 nm. Samples were cleaved and placed in the SEM at a -5 degree stage tilt using an SEM probe current of 20 kV. EDS line scans 11.5 μm in length were placed across the cleaved interface parallel to the pores. $TiO_2$ ALD film thickness profiles within the porous AAO membrane were extracted using the EDS inferred thickness method and plotted versus pore depth (Figure 40). Thickness

profiles demonstrate a strong gradient down the length of the pore with a conformality of ~55%. Conformality within the last 0.5 μm of the pore is ~88%.

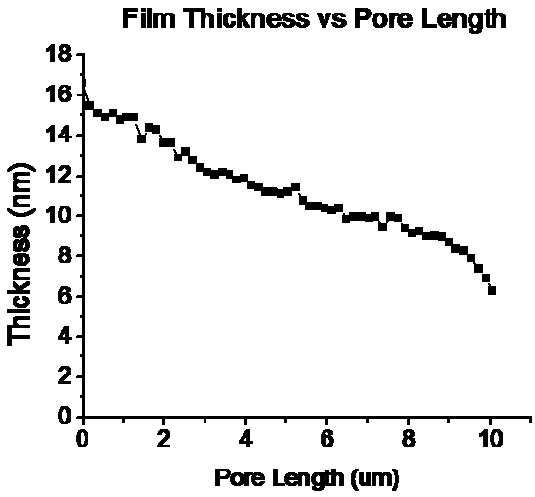


**Figure 40. Graph of EDS inferred film thickness as a function of pore length. Curve displays a notable gradient down the length of the pore with film thickness measuring around ~7nm near the bottom of the poor.**

### 5.3.2 TEM Nanotube Metrology

TEM images reveal $HfO_2$ nanotubes produced by the removal of the AAO membrane after ALD deposition are cylindrical in shape, characteristic of the pores in which they were formed, as seen in Figure 41. Nanotubes appear as long rectangular ribbons with dark edges running along their lengths. Figure 41a displays a cluster of nanotubes illustrating the broadening structure reminiscent of a nail-head connecting the nanotubes to one another. This structure is created by the deposition of ALD on the top surface of the AAO membrane. Figure 41a also demonstrated the thinning of the wall down the length of the nanotube indicating reduced deposition deep within the pores and a decrease in conformality. Figure 41b shows a single $HfO_2$ nanotube with no nail-head

top implying the nanotube broke midway down the length of the nanotube. The inset in Figure 41b is the selected area diffraction (SAD) pattern confirming the amorphous character of the $HfO_2$ nanotubes. To see the fabrication method of $HfO_2$ nanotubes please refer to Appendix V.

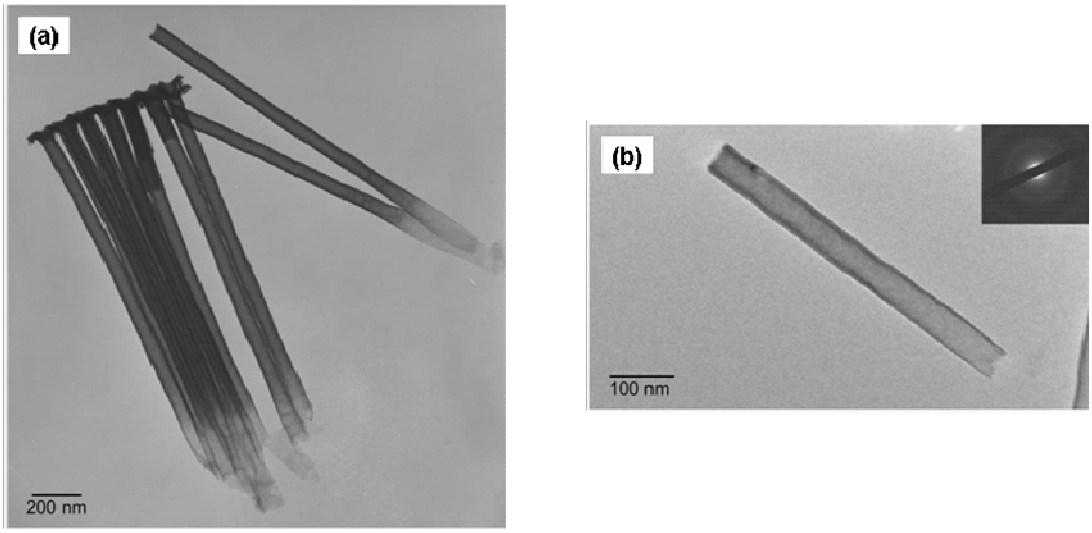


**Figure 41. TEM images of $HfO_2$ nanotubes made by deposition of $HfO_2$ ALD into porous AAO membranes followed by membrane dissolution; a) Group of $HfO_2$ nanotubes demonstrating the nail-head top of the nanotube and thinning of wall thickness down the length of the nanotube and b) a single $HfO_2$ nanotube broken midway down the full nanotube with an inset of the selected area diffraction pattern dictating that the films are amorphous.[44]**

Bright field TEM records the intensity of electrons transmitted through a thin sample in order to produce an image. Therefore, the darker edges of the nanotube can be attributed to a higher material density at the nanotube wall. Due to this correlation the nanotube wall thicknesses can be extracted using ImageJ image analysis program.[44] Nanotubes were fabricated by the deposition of $TiO_2$ using ALD within a 10 μm deep nanoporous AAO membrane followed by dissolution of the membrane. A TEM image

found in Figure 42 displays the bulbous bottom half of a 10 μm long $TiO_2$ nanotube with a measured wall thickness of ~ 7 nm near the bottom and ~ 9 nm about 0.5 μm up the nanotube. This constituted 87.5 % conformality within the bottom portion of the nanotube. It should be noted that the TEM sample consisted of a significant amount of debris which is believed to be a mixture of dried phosphoric acid particulates and dust particles from the sample preparation.

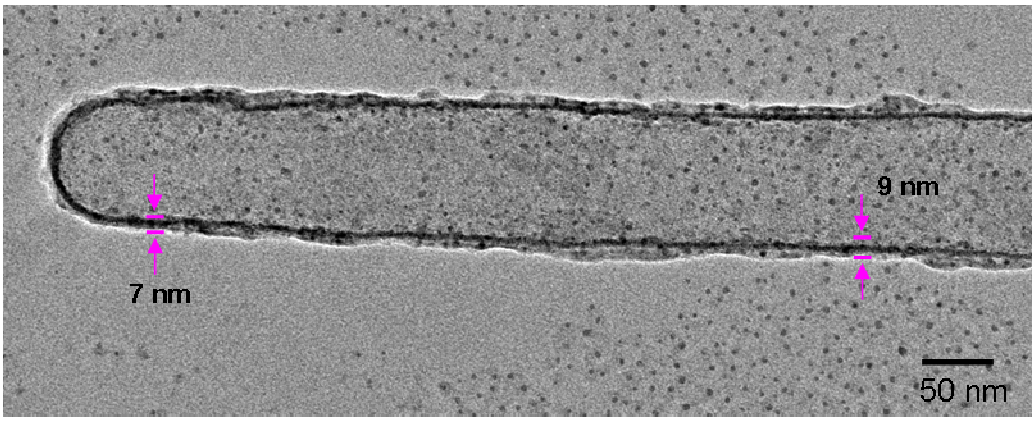


**Figure 42. TEM image of a $TiO_2$ nanotube with wall thickness of ~7 nm near the bottom and ~9 nm about 0.5 μm up the length of the nanotube.**

## 5.4 Discussion

ALD is widely emerging in the world of nanotechnology due to its precise atomic-level thickness control and unprecedented conformality over very demanding 3D nanoscale topographies. It has already been demonstrated as a useful deposition technique in the fabrication of energy devices[20-22], memory and thin film transistor applications[9, 14, 28], optoelectronics[15, 16], catalysis[17-19], coating nanoparticles[32-36], as well as various MEMS[23-27] and NEMS[5, 29, 49, 130] devices. A large contingent of ALD process chemistries have been identified, placing a

great need on rapid characterization and optimization of ALD process parameters for nanostructure applications.[4]

The distinctiveness of ALD derives from its self-limiting adsorption/desorption reactions during each precursor half cycle. However, the self-limiting behavior falls short due to depletion effects and process complexities associated with the precise amount of precursor and sufficient purge times to avoid parasitic CVD-like behavior. While the benefits of ALD are usually kept intact for planar cases, it is not always the case for high aspect ratio nanostructures, such as porous AAO, where deposition mechanisms are now diffusion limited rather than surface kinetics limited.[66] Due to this behavior, the development of new metrology techniques for measuring thin films in complex nanostructures is critical as is emphasized by the International Technology Roadmap for Semiconductors.[131] However, qualitative and quantitative metrology for novel nanostructures has proven challenging due to decreasing dimensions encountered in next generation devices.

The use of EDS line scans as opposed to SEM and TEM imaging is meant to help alleviate frustrations found during sample preparation and imaging of ALD thin films within nanoporous structures. Sample preparation of this method is meant to be relatively easy as precise cleaving of a nanopore is not necessary due to the fact that the electron beam used during SEM measurements penetrates the sample well past the interface of the cleaved surface and creating a cascade of x-rays to be measure via EDS. $TiO_2$ ALD film thicknesses extracted from the EDS inferred thickness method are in excellent agreement with direct measurements of nanotube wall thicknesses determined

in TEM. There could be discrepancies based on how well one can measure wall thicknesses from TEM images.

## 5.4 Conclusions

The combination of porous AAO and ALD presents an attractive platform for the advancement of nanotechnology; however, measuring thin films deposited in high aspect ratio nanostructures has proven difficult. This work demonstrates an EDS analysis method that makes use of a cleaved, ALD coated porous AAO template revealing the parallel nanopores along the template's cross-section. The sample preparation of this method is meant to be relatively easy as compared to methods that utilize precise cross-sectioning and sample thinning techniques and are considered quite time consuming.

A means to extract film thicknesses and conformality of ALD thin films deposited in the high aspect ratio nanopore of an AAO template was demonstrated through the use of an EDS inferred thickness model. The model was based on a cylindrical assumption in which a nanotube formed within an AAO nanopore is comprised of the ALD film used. Extracted film thicknesses from the EDS inferred thickness model were validated by comparing results to film measurements of a released nanotube imaged via TEM. Initial film thicknesses within the nanopore/tube were considered to be equivalent to film thicknesses measured across the planar surface. The results from the EDS inferred thickness method are comparable to direct TEM measurements and demonstrate the usefulness of this method to extract film thickness and conformality, as will prove to be directly relevant to the understanding and control of ALD processes and their integration into nanotechnology.

# Chapter 6: ALD Conformality and Process Optimization in 3D Ultrahigh Aspect Ratio Nanopores

This chapter discusses the critical role of interdependent process parameters, such as reactant dose, surface residence time, and purge time on the conformality of an ALD thin film when transitioning from a 2D planar system into that of a 3D ultra-high aspect ratio nanopore. It has been demonstrated in Chapter 4 that excellent uniformity can be achieved with higher precursor doses and increased surface residence times, even though the growth rates exhibited a non-ideal saturation of the surface. The production of $H_2O$ during the TTIP half-cycle is proposed as the culprit to secondary reactions that complete the ALD cycle and deposit more than the expected sub-monolayer of growth. When transitioning from a 2D planar case in the viscous flow regime to that of a molecular flow regime found in an ultra-high aspect ratio nanopore, the complex reaction dynamics that occur in the planar system is intensified in a nanopore. Increased doses are necessary to compensate for the increase in surface area, as well as longer surface residence times for molecules to diffuse down the pore and extended purge times to allow unreacted precursor and by-products diffuse out. However, as these process parameters are deemed necessary to deposit conformal films within a high aspect ratio nanopore, the complex reaction dynamics that occur on the planar surface will have great influence on the deposition within the nanopore.

## 6.1 Introduction

In order to keep up with Moore's Law, the International Semiconductor Roadmap has emphasized a need to access reduced feature sizes found in the device designs of transistor and memory technologies.[132] However, as capacitor technology transitions from the early days of planar capacitors to that of trench capacitors having aspect ratios greater than 60:1, conformal coatings are playing an increasing crucial role.[133] Conventional deposition techniques, such as the physical vapor deposition (PVD) methods sputtering and evaporation, as well as chemical vapor deposition (CVD), are found to have limited abilities to coat complex structures with increasing aspect ratios due to their poor step coverage.[66] The increasing need to deposit thin, continuous pin-hole free films in complex 3D geometries is not only limited to ULSI technologies, but is also essential to a wide range of other technologies, such as optoelectronics[2, 15, 16], catalysis[18, 49, 134], energy devices[20-22, 98, 135], gas sensors[30], micro-electro-mechanical systems (MEMS)[23, 24, 26, 136], and nano-electro-mechanical systems (NEMS)[33, 37, 38, 49], that all exploit the benefits found in using nano-scaled structures with increasingly high aspect ratios. Therefore, researchers have turned to atomic layer deposition (ALD) to offer high quality films with atomic level thickness control and unprecedented uniformity and conformality in the most demanding 3D nanostructures.

ALD is a gas phase deposition technique which utilizes self-limiting surface chemistries to control film thickness down to the atomic scale. This control is inherent in the self-limiting surface chemistry where reactants are sequentially pulsed creating saturated chemisorbed surface reactions in order to achieve a monolayer or less of film

per cycle. Much work has focused on the interplay of key ALD process parameters, particularly in terms of thickness control and uniformity.[14, 68, 80, 104, 113] It was determined that when in a 2D planar viscous flow regime, the rate limiting step of the ALD deposition is the surface reaction kinetics across a planar surface; therefore, when precursors are underdosed, a thickness gradient occurs due to an insufficient amount of precursor being supplied to completely saturate the surface.[66, 68]

In recent years, there has been an increasing interest in the combination of ALD deposited within the high aspect ratio nanopores found in a porous anodic alumina (PAA) membrane. PAA is a self-assembled, electrochemical templating technique that results in the formation of a high density of cylindrical nanopores within a close-packed hexagonal array on the surface of an aluminum template.[97, 137] PAA naturally lends itself to many applications in nanotechnology, such as a template for nanowire and nanotube fabrication[29, 49, 98, 99], scaffolds for catalysts[18, 49, 134], dye sensitized solar cells[98], batteries[93], and sensors[30]. Recently Banerjee et al, demonstrated an operational metal-insulator-metal (MIM) electrostatic nanocapacitor by depositing multilayers of ALD TiN-$Al_2O_3$-TiN films within a PAA membrane with an aspect ratio of ~200.[21] Although they demonstrated an equivalent planar capacitance of ~100 $\mu F/cm^2$ using $Al_2O_3$ as the dielectric layer ($\varepsilon_k$ ~9), it is believed that with the use of high-k dielectrics, such as $HfO_2$ ($\varepsilon_k$ ~14) or $TiO_2$ ($\varepsilon_k$ ~80), as well as, higher aspect ratio nanopores higher equivalent capacitance values can be achieved.[21, 138]

The combination of ALD and PAA has led to considerable attention to optimizing ALD conformality within ultra-high aspect ratio nanopores in a molecular flow regime.

Works include simple models for determining precursor dose[66], Monte Carlo techniques to understand the importance of precursor sticking probability[67], solving simultaneously Boltzmann's transport and surface reaction equations[101, 139] and correlating them with experimental results while trying to optimize conformality in ultra-high aspect ratio structures. These models and work demonstrate that when deposition transitions from a 2D planar structure in a viscous flow regime to that of a 3D nanostructure in a molecular flow regime different reaction mechanisms dominate the deposition, where in a 3D nanostructure the rate limiting step is the Knudsen diffusion of precursor molecules[66, 140]. Therefore, deposition within a 3D nanostructure in a molecular flow regime requires much more control over deposition parameters than for planar or micro-scale features found in a viscous flow regime. Although there has been much focus on both the 2D and 3D cases separately, there has been little focus on the actual influence the 2D planar deposition may present on the conformality within a 3D ultra-high aspect ratio nanopore.

In this chapter, we investigate the impact of key process parameters such as reactant dose, surface residence time, and purge time on conformality profiles of ALD layers deposited into the nanopores of a PAA membrane while comparing them to the 2D planar deposition behavior. We focus on the deposition of $TiO_2$ as a high-k dielectric material using titanium tetraisopropoxide (TTIP) and ozone as the metal containing and oxidizing precursors, respectively. This study will illustrate that while uniform films can be achieved, the growth behavior across the planar surface will have a significant impact on conformality profiles within an ultra-high aspect ratio nanopore due to changing

aspect ratios and the interplay between diffusion and surface reactions when transition between viscous and molecular flow regimes.

## 6.2 Experimental Setup

PAA templates were synthesized using a two-step anodization method as seen in Chapter 2.[97] In short, a piece of electropolished aluminum foil (99.99%, Alfa Aesar) was anodized at 40 V and 103 °C in an electrolytic bath of 0.3 M oxalic acid. Foils were anodized for ~7 hrs in order to produce well ordered parallel pores with respect to the aluminum surface. These 1$^{st}$ anodized membranes were etched off by an aqueous solution of phosphoric acid (6 wt%) and chromic acid (1.8 wt%), leaving a pre-textured and ordered aluminum surface. Foils were anodized for a second time for 2 hrs 17 min defining a pore depth of ~ 10 μm. Pore diameters were adjusted to ~90 nm by using a pore widening solution of 0.1 M of phosphoric acid at 38 °C.

High-k dielectric TiO2 films were deposited in a custom built ultra-high vacuum (UHV) cross-flow wafer scale ALD reactor, using titanium tetraisopropoxide (TTIP) and ozone ($O_3$) as precursors. Precursors were introduced and exhausted through 2 opposing slits positioned 3 mm above the wafer. The mini-reactor was operated at 130 mTorr and the substrate heater was maintained at 200 °C. TTIP doses were varied using the same dosing scheme found in Chapter 4 (Figure 33) for a single μpulse, 3, and 6 μpulses in both parallel and in series, while ozone doses were maintained in an over-saturation regime. Purge times were maintained at 20 sec between both precursors' half cycles, except when investigating the purge time parameter during the TTIP dose on deposition behavior.

TiO2 films were deposited on both flat Si substrates and in PAA templates. Si samples were dipped in a 3% HF solution to remove the native oxide and PAA templates were adhered to the Si near the inlet of the precursors. After deposition planar maps of film thickness were obtained using a Sopra GES5 spectroscopic ellipsometer with an automated xy stage. Thickness profiles were taken of equidistant points across the wafer in the direction of the flow, with the first point being closest to the gas inlet and the last point being closest to the exhaust outlet. The percentage of uniformity is determined by the ratio of the standard deviation over the mean value ($\sigma/\mu$) of all points taken across the wafer subtracted from 100%.

High resolution top down and cross sectional SEM was performed on bare and ALD coated PAA samples using a Hitachi SU-70 SEM equipped with EDS. Cross sectional PAA samples were made by removing the underlying aluminum in a $CuCl_2$ solution and cleaving the remaining PAA membrane. EDS line scans were taken across the cleaved ALD deposited PAA templates. Film thickness as a function of pore length was extracted from the EDS compositional scans by setting the intensity proportional to the cylindrical volume of the sample being measured. The percentage conformality was determined by taking the (max - min) / (max + min)*100% and subtracted from 100%.

## 6.3 Results

PAA membranes were fabricated in oxalic acid and anodized for 2 hrs and 17 mins allowing pores to grow to a depth of 10 μm and pore widened for 46 min and achieving pore diameters of ~88 nm. Pore diameters and depths were verified using top-

down and cross-sectional SEM images. The pore density was calculated from the interpore spacing of 110 nm and determined to be 1.27 x$10^{10}$ pores/$cm^2$. One pore repeat unit consists of a hexagonal unit cell and a cylindrical pore, therefore the surface area of one unit is calculated to be 2.77 x $10^{-8}$ $cm^2$. Therefore, the surface area of a PAA membrane increases by ~350% as compared to a planar Si wafer.

ALD is dependent upon sufficient doses in order to completely saturate a surface and deposit uniform and conformal films. Therefore, the effects of the process parameters, dose and surface residence time of the TTIP reactant, on film uniformity across a 2D planar Si wafer versus conformality within a nanoporous PAA membrane were investigated. The TTIP precursor dose was varied from an "ideal" planar saturation level to that of over-saturating, while maintaining the ozone dose at an over-saturation level. In order to increase the dose and surface residence time of a precursor, doses were broken up and introduced into the reaction chamber in the same fashion as that discussed in Chapter 4. $TiO_2$ films were deposited simultaneously across planar Si wafers and in PAA membranes with an aspect ratio of 111 for 250 cycles. Figure 43 displays 4 consecutive ALD runs demonstrating highly uniform thickness profiles across the surface of a 100 mm planar wafer, with the direction of flow going from 0 mm to 70 mm. The single μpulse case introduced 0.55 μmols into the system with a surface residence time of about 10 sec, as determine by monitoring the increase in the reactor pressure until it returned to the base pressure of 100 mTorr (as seen in Chapter 4, Figure 33). The single μpulse scheme was deemed the ideal planar saturation level as it produced ideal growth rates of ~0.66 Å/cycle, as reported in the literature, and had across-wafer uniformity of

99.6 % (standard deviation, 1 sigma). As doses were introduced in parallel to achieve an over-saturating dose (i.e. increased TTIP partial pressure, therefore, increased amount of molecules) and subsequent longer surface residence times, thickness profiles demonstrated that wafer uniformity was maintained at ~ 98%, even as growth rates increased. It was discussed in Chapter 4 that the increase in growth rates are due to complex secondary reaction mechanisms associated with using TTIP as a precursor. Interestingly, as doses were introduced "in series", the resulting film continued to maintain uniformity even though its growth rate decreased from the "in parallel" counterpart as a result of the 10 sec delay between µpulses creating an intermediate purge step.

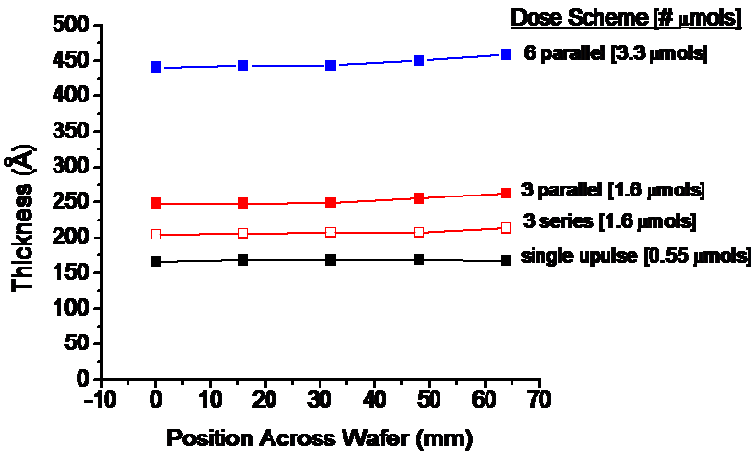


**Figure 43. Highly uniform films of $TiO_2$ ALD thin films deposited across 2D planar wafers for 250 cycles for three different dosing schemes. Demonstrates increased film thicknesses, yet maintained film uniformities.**

Figure 44a illustrates that the benefits of uniform ALD seen for planar wafers in

the viscous flow regime (Figure 43) do not translate into good conformality down the length of a high aspect ratio nanopore in the molecular flow regime. Thicknesses with respect to 0 μm pore depth correspond to the planar thicknesses at pore entrances, where deposition in a pore for the single μpulse case demonstrates film thicknesses deplete from the initial 166 Å ± 1 Å at the pore entrance ( 0 μm) down to roughly 70 Å ± 2 Å near the bottom of the pore (8.5 μm). This decrease in film thickness constitutes a decrease in conformality by ~30%. Initially this drop in film thickness was believed to be due to insufficient doses as a result of higher surface area and/or insufficient surface residence times for a molecule to diffuse down the length of the nanopore. However, as doses were increased from an "ideal" saturating dose to an over-saturating dose "in parallel", films within the pore exhibited notable gradients down the length of the pore (Figure 44a). Conformality as a function of the number of molecules introduced into the system for each dosing scheme is shown in Figure 44b for three different regions within the nanopore. Conformality was determined between 0 μm to 8.5 μm pore depth in order to determine the overall trend in conformality and avoid any influence that may be imposed by inaccurate computation of the EDS inferred thicknesses. The results in Figure 44b demonstrate that films are ~70% conformal for the single μpulse case (black dashed line) as opposed to ~35% conformal associated with the 6 μpulse case introduced in parallel (blue dashed line) from 0 μm to 8.5 μm down the length of the pore.

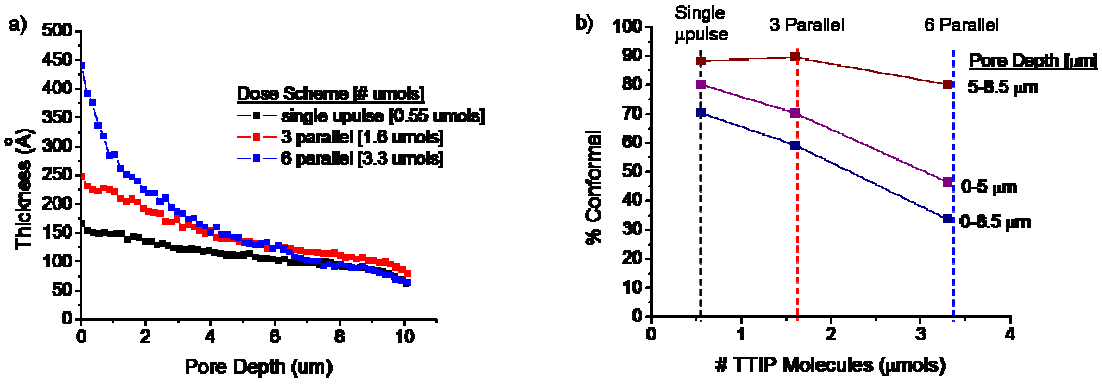


**Figure 44. a) $TiO_2$ thickness profiles down the length of a 10 µm deep nanopore for increasing doses introduced in parallel and b) their corresponding conformalities as a function of the number of TTIP molecules introduced in parallel for three different regions within the nanopore: 0-8.5 µm, 0-5 µm, and 5-8.5 µm.**

As the number of TTIP molecules is increased as a function of the dose scheme used, steeper gradients appear to occur within the first 5 µm of the nanopore, implying two deposition regions may occur within the pore. Figure 44b displays the conformality as a function of the number of molecules associated with each dosing scheme as deposited within 1) the top half of the nanopore from 0 µm to 5 µm and 2) the bottom half the pore from 5 µm to 8.5 µm. The plot highlights that the first 5 µm of a nanopore has a significant decrease in conformality as opposed to the bottom half of the pore. The results further indicate the decrease in conformality within the first 5 µm as the number of TTIP molecules and subsequent surface residence times associated with the dosing schemes "in parallel" are increased, where as the bottom half of the nanopores appear to be in good correlation to each other. Therefore, the overall trend in conformality, from 0 µm to 8.5 µm, echoes the conformality within the top half of the

nanopore.

Figure 44 indicated that an increase in TTIP dose and surface residence time produced significant gradients down the length of an ultra-high aspect ratio nanopore. Therefore, it was believed that an increase in TTIP purge time could significantly improve conformality within the pores. Purge times were varied for a TTIP dose of 3 μpulses introduced in parallel in combination with an over-saturating ozone dose, 250 cycles of $TiO_2$ were deposited simultaneously across 100 mm planar Si wafers and PAA membranes with an aspect ratio of 111. Figure 45 demonstrates highly uniform films were maintained across planar wafers as purge times were varied from 10 sec to 60 sec. Thicknesses associated with a 10 sec purge resulted in significantly higher growth rates indicative of a CVD behavior, conversely, some CVD process are still capable of producing uniform films. On the other hand, the combination of uniform films and the saturating behavior of the film thicknesses as purge times were increased, reiterated that deposition is attributed to the complex reaction dynamics associated with complex secondary reaction mechanisms when using TTIP as a precursor.

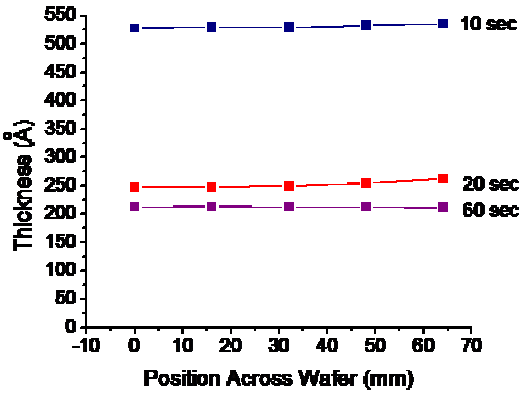


**Figure 45. Highly uniform films of $TiO_2$ ALD thin films deposited across 2D planar wafers using an over-dose of ozone and a TTIP dose of 3 µpulses (1.6 µmols) in parallel followed by various purge lengths.**

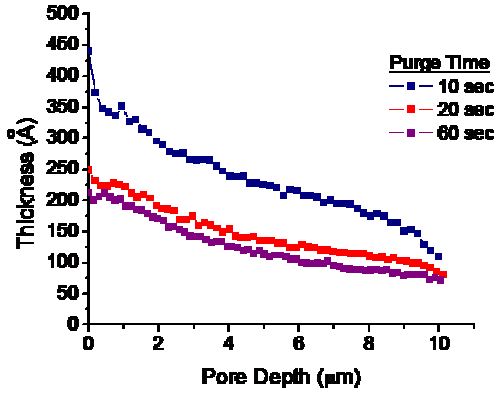


**Figure 46. $TiO_2$ thickness profiles down the length of a 10 µm deep PAA nanopore for different purge times after 3 µpulses introduced in parallel. Profiles are associated with the planar depositions found in Figure 48.**

Nonetheless, when transitioning to an ultra-high aspect ratio nanopore the benefits of planar uniformity still do not translate into good conformality within the pore. Figure 46 exhibits steep thickness gradients down the length of a 10 µm deep nanopore. Film thicknesses within the nanopores are dependent on film thicknesses found across the planar surface. Planar results in Figure 45 indicate that film thicknesses associated with a 10 sec purge exceed the 440 Å film thickness limit imposed by the nanopore diameter of 88 nm. Therefore, films deposited with in the PAA membrane actually clog the pore and result in a strong gradient within the pore. Figure 47 plots the conformality of the films in an ultra high aspect ratio nanopore as a function of the purge time. Results indicate that an increase in purge time does not improve film conformality rather it tends to saturate. This behavior alludes to a more intricate interaction between a precursor's dose and surface residence time in a molecular flow regime exists.

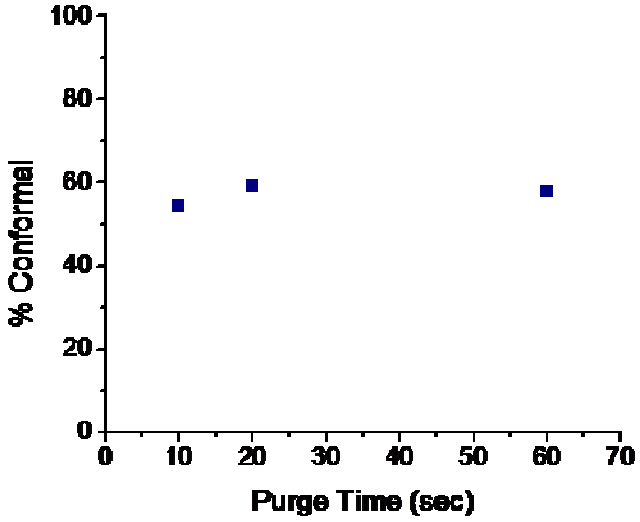


**Figure 47. Conformality determined for thickness profiles found in Figure 49 as a function of the TTIP purge time following a dose of 3 μpulses introduced in parallel.**

Thickness profiles displayed in Figure 46 show significant gradients down the length of an ultra-high aspect ratio nanopore and imply that longer purge times do not in fact improve conformality. Therefore, doses were introduced in series with the fore thought that a 10 sec delay between μpulses would act as an intermediate purge step, allowing more molecules to be introduced into the system without the increase in surface residence time. $TiO_2$ films were deposited across 100 mm planar wafers simultaneously with a PAA membrane with aspect ratios of 111 for 250 cycles. As discussed earlier, Figure 43 shows a film deposited across a 2D planar surface with 98.6% uniformity (standard deviation, 1 sigma). Although film growth rates are ~ 26% higher than those of the single μpulse case, the intermediate purge step seems to dispel some of the secondary reactions associated with using TTIP as a precursor. Therefore, when transitioning to an

ultra-high aspect ratio nanopore the benefits of planar uniformity are starting to be translated into good conformality within the nanopore. Figure 48 reveals that although gradients still exist down the length of the pore, they are not as severe as the dose introduced in parallel scheme and tend to behave more like a single µpulse.

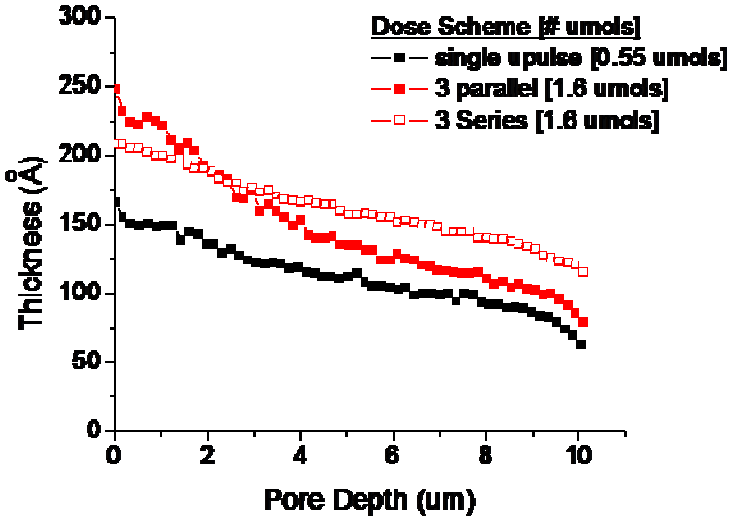


**Figure 48. $TiO_2$ thickness profiles down the length of a 3D ultra-high aspect ratio nanopore with an aspect ratio of 111 for different dosing schemes. Profiles are associated with the planar depositions found in Figure 43.**

Figure 49 presents the conformality as a function of the number of TTIP molecules introduced into the system for the three different dosing schemes used, as well as, the various purge times investigated with the 3 µpulses "in parallel" dosing scheme. Results signify that dose introduced "in series" improves the conformality within a nanopore as compare to the single µpulses case and doses introduced "in parallel". It further demonstrates that the purge time had no significant effect on the conformality

with in an ultra-high aspect ratio nanopore. Therefore, conformality benefits from the introduction of intermediate purges between μpulses, as to allow more molecules to be introduced into the system to compensate for increased surface areas, but also allows unreacted precursor, by-products to purge out of the system while allowing any secondary reactions to equilibrate before more precursor is introduced.

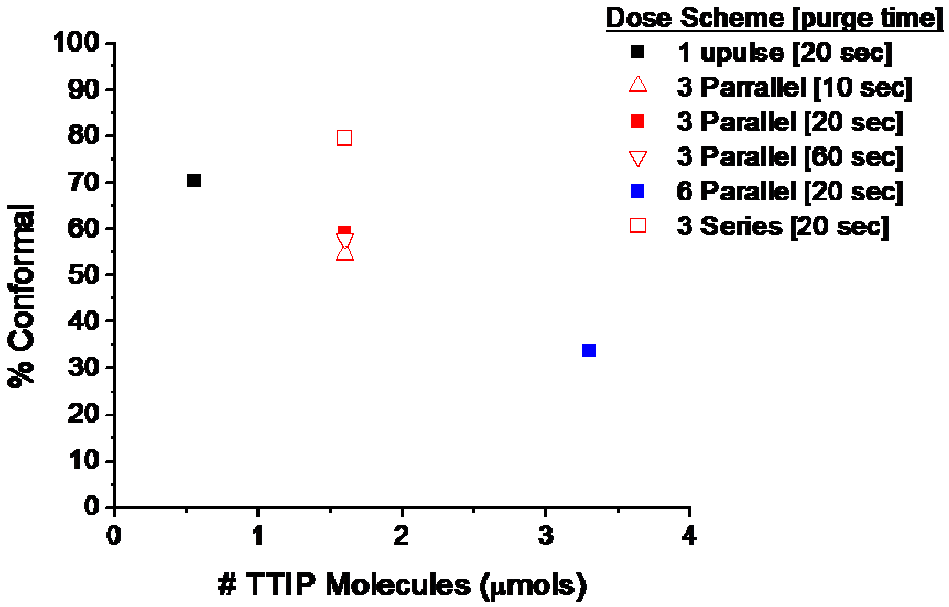


Figure 49. Conformality determined for thickness profiles found in Figure 44, 46 and 48 as a function of the number of TTIP molecules introduce into the system for various dosing schemes and purge times.

## 6.4 Discussion

Maintaining wafer scale uniformity and nanopore conformality is dependent upon the complex reaction dynamics associated with chemisorbed reactions found within

different flow regimes. Highly uniform $TiO_2$ films were deposited across 2D planar wafers even with an observed increase in growth rates. Chapter 4 attributed the increase in planar growth rates to the complex reaction dynamics associated with the production of $H_2O$ as a by-product when using TTIP as a precursor, where higher doses and longer surface residence times encouraged secondary reactions. However, when transitioning to an ultra-high aspect ratio nanopore these complex reaction mechanisms are magnified and are highly influenced by the dose and surface residence time of the precursor. As doses and surface residence times were increased to compensate for the increase in surface area and the diffusion of precursors down the length of an ultra-high aspect ratio nanopore, notable gradients were observed as a function of pore depth. Several explanations can be attributed to the decrease in conformality within a nanopore, such as the transition from viscous flow to molecular flow, the continually changing aspect ratio, and the complex reaction mechanisms associated with using of TTIP and ozone as precursors.

One of the trademarks of the ALD process is the self-limiting surface chemistry which is dependent on sufficient amounts of precursor to be supplied to completely saturate a surface. Therefore, when transitioning from a 2D planar wafer to that of a 3D nanopore, higher doses are necessary to account for the increase in surface area. However, when transitioning from the 2D, viscous flow to 3D, molecular flow, higher doses are not the only requirement to deposit conformal films. When transitioning from different flow regimes, different deposition mechanisms will dominate the deposition kinetics. In a viscous flow, reactions are limited by the surface reaction times, whereas,

in molecular flow the rate limiting step is the Knudsen diffusion of the larger precursor molecules (in this case TTIP). Therefore, in order to compensate for higher surface areas and longer diffusion times, the dose (i.e. the partial pressure) and surface residence time of the TTIP precursor were increased. During the course of deposition the aspect ratio changes with every cycle requiring precursors to either be put in a constant over-saturating regime or the doses and surface residence times need to be compensated for with each cycle. Also with an increase in aspect ratio, it is imperative that unreacted precursor and by-products are given sufficient time to purge out of the system before the next precursor is introduced.

The production of water during both the TTIP and ozone half-cycles is considered detrimental when in the confines of an ultra-high aspect ratio nanopore. Water is considered a very "sticky" molecule due to its high polarity and therefore, can linger within a system requiring extensive purge times. In the case of ozone, if purge times are insufficient, a parasitic CVD-like reaction can occur within the nanopore due to both the metal and oxidizing precursors being present in the system simultaneously. To further compound the situation is the transition regime that exists between systems in viscous flow versus that of a molecular flow. In the viscous flow regime, higher partial pressures of a precursor can lead to higher particle interactions directing the flow in a laminar streamline across a surface (i.e. the velocity at the wall is zero), therefore, the time it takes to completely saturate a surface is relatively short and decreases with higher pressures. However, when in the molecular flow regime, the mean free path between two molecules is so large that the flow is dominated by gas-wall collisions, taking a longer

time for a reactant to find an active surface site. When transitioning from one flow regime to another, a transition regime is created, where gas molecules not only collide with each other, but with the wall of the system as well. In the case of TTIP, the production of water can have a detrimental impact on the deposition kinetics within this transition regime. After a TTIP molecule adsorbs to the surface, its by-product of water can possibly self-react leading to a completed ALD reaction or it could react with the incoming flux of TTIP molecules, thus leading to a parasitic CVD-like reaction. When CVD-like reactions occur within the pores the precursor is inevitably depleted thus creating thickness gradients down the length of the nanopore. Nevertheless, some TTIP molecules will diffuse through the transition region unreacted and will chemisorb on the surface within the molecular flow regime, therefore, resuming an ALD reaction. However, molecules in a molecular flow regime are subject to their wall interaction and can therefore change direction regardless of their incoming trajectory. Therefore, the probability of a molecule to continue to flow in the positive direction (i.e. towards the bottom of the pore) rather than in the negative direction (i.e. back towards the transition region) is cut in half. Therefore, the deposition within an ultra-high aspect ratio nanopore can be thought of as a mixture of CVD and ALD-like behaviors.

## 6.5 Conclusions

ALD is receiving credit for some of the most demanding deposition processes in nanotechnology due to its exceptional ability to coat ultra-high aspect ratio structures with very thin films. PAA provides a versatile and easy platform to analyze ALD profiles in order to optimize the ALD processes and achieve conformal films. It was

demonstrated that maintaining atomic level thickness control with wafer scale uniformity and nanopore conformality is subject to the complex reaction dynamics associated with chemisorbed reactions in various flow regimes. The influence of interdependent process parameters such as reactant dose, surface residence time, and purge time on uniformity and conformality profiles of $TiO_2$ ALD was investigated. The study illustrates that uniform films were achieved across a 2D planar wafer in viscous flow, even with observed growth rates. However, the complex mechanisms associated with higher growth rates in the viscous flow regime are magnified when in the confines of an ultra-high aspect ratio nanopore leading to a decrease in film conformality. Several possible explanations were attributed to the decrease in conformality within a nanopore, such as the transition from viscous to molecular flow, the continually changing aspect ratio, and the complex reaction mechanisms associated with using of TTIP and ozone as precursors. Precursor doses, surface residence times, and purge times are only a few of the contributing factors in understanding the complex reaction dynamics found within the ALD process. Further investigations of the complex interplay of process parameters is essential to the optimization of the ALD process and will play an important role in the design and nanofabrication of next generation energy devices.

# Chapter 7: Conclusions and Future Work

## 7.1 Conclusions

Nature's ability to self-assemble and self-limit is leading the way for next generation energy devices. Atomic Layer Deposition is receiving responsibility for some of the most demanding deposition processes in the nano-community, by demonstrating its unique ability to process ultrathin films with unprecedented uniformity and conformality across 2D planar and complex 3D nanostructure topographies. PAA has proven itself to be a versatile and easy platform for device design as well as nanostructure templating. Our recent development of an operational MIM electrostatic nanocapictor requires the use of high-k dielectric thin films deposited into the confines of an ultra-high aspect ratio PAA membrane. Currently our work is limited by the use of $Al_2O_3$ as our high-k dielectric material. It is believed that through the use of higher-k materials, such as $TiO_2$, higher capacitance values can be achieved. As no two ALD chemistries or reactors are the same, the deposition of $TiO_2$ ALD required an in depth study of the growth behavior when transitioning from a 2D planar system to that of a 3D ultra-high aspect ratio nanopore in order to optimize the process conditions to achieve conformal ALD films.

Using a commercial Beneq ALD reactor, I reemphasized the conformal behavior of ALD to coat the complex surface topography of a highly scalloped Al surface produced after the removal of the 1$^{st}$ anodized PAA membrane. I demonstrated that the evolution of surface profiles change with the ALD layer thickness and are influenced by the way ALD conformally decorates the underlying topography. Excellent agreement

was seen between the experimental data and the results of a simple geometric 3D extrusion model developed by Dr. Israel Perez confirming that ALD produces highly conformal films even on highly structured, sharp features of a complex nanotopography. The model demonstrates how the surface effectively becomes planarized with increased ALD film thickness, where ALD growth fronts from higher surface features dominate the surface profiles and eventually merge. This work illustrates the benefits of ALD to conformally coat and modify surface topographies in which sharp asperities or nano-roughness could potentially limit device performance.

I iterated that ALD is a self-limiting and self-saturating gas phase deposition technique that is highly dependent on the precursor chemistries used and the interplay of critical process parameters, such as temperature, reactant dose, surface residence time, and purge time. Using a custom built UHV ALD system; I deposited high-k $TiO_2$ thin films using TTIP and ozone while employing a unique dosing scheme in order to evaluate the relationship between film metrics, growth rate and uniformity, and the process parameters: precursor's partial pressure, surface residence time, and purge time. Results demonstrated increased growth rates as a function of increased reactant surface residence times within the process chamber. It was proposed that the complex reaction mechanisms associated with using TTIP as a precursor led to secondary reaction mechanisms and higher growth rates due to the production of $H_2O$ as a by-product during the TTIP half cycle of the ALD process. Longer purge times confirmed that the increased growth was not due to physisorbed precursor molecules or parasitic CVD reactions. Although the films exhibited higher growth rates, they still revealed

exceptionally uniform films across the wafer, further emphasizing that the ALD reaction was self-limiting and self-saturating.

I proposed a method to extract film thicknesses and subsequent conformality of deposited ALD films within ultra-high aspect ratio nanopores through the use of EDS line scans. A relationship between the deposited ALD film thickness and intensity profiles from EDS line scans along a cleaved PAA template was determined through a cylindrical assumption and the growth rate determined from planar film thicknesses. Film thickness profiles were compared to direct measurements from TEM images of released ALD based nanotubes. EDS inferred profiles and TEM images demonstrated that although there was a strong depletion of film thickness down the length of the nanotube, films could still be accurately measured.

I demonstrated the crucial interplay of process parameters, such as reactant dose, surface residence time, and purge time on the deposition of thin films in ultra-high aspect ratio nanopores as compared to deposition across a planar wafer. I deposited high-k $TiO_2$ thin films using TTIP and ozone as precursors, while employing a unique dosing scheme to evaluate the relationship between film metrics, uniformity and conformality, and the process parameters. Results indicate that uniform films across a 2D planar wafer do not translate into conformal films within a nanopore when less than optimized processes are used. Several explanations were attributed to the decrease in film conformality and the subsequent rise of CVD-like behaviors within an ultra-high aspect ratio nanopore. Possible explanations include the transition from viscous to molecular flow, continually changing aspect ratios, and the complex reactions associated with using TTIP and ozone.

## 7.2 Future Work

Growth rates, uniformity and conformality are to a large extent the golden standards to evaluate the performance of an ALD process. We have shown that our cross-flow ALD system is a versatile platform to study the impact of reactant exposures, surface residence times, and purge times on film growth behaviors across planar 2D wafers as well as complex 3D nanostructures. $TiO_2$ ALD films have a strong potential to be the next generation high-k dielectric material.[141] Throughout this work a number of tools and methodologies have been developed to examine the extrinsic (growth rate, thickness uniformity and conformality) properties of $TiO_2$ ALD films using TTIP and ozone as the self-limiting precursors. Therefore, a logical continuation of this work is to further the investigation of the complex reaction mechanisms associated with the use of the precursors TTIP and ozone through in-situ chemical analysis using mass spectrometry. It is also important to characterize the intrinsic (electrical, optical, compositional) properties of the $TiO_2$ films not only across planar 2D wafers but in complex 3D nanostructures is a key component to the next generation of MIM electrostatic nanocapacitors.

$TiO_2$ ALD exhibits its highest dielectric constant in its rutile phase at $\varepsilon_k$ ~80.[141] However, as deposited $TiO_2$ films are amorphous and require high temperature annealing that could potentially lead to grain growth in the high-k dielectric causing an increase in the leakage current, as well as potentially damage the metal electrode within an MIM electrostatic nanocapacitors.[141, 142] It has been noticed that the deposition of $TiO_2$ on the conductive metal Ru leads to the deposition of rutile $TiO_2$.[125] Ru and $RuO_2$ are

both conducting materials that can both be used as the bottom electrode of an MIM nanocapacitor.[60, 141] Recently, our UHV ALD reactor has been outfitted for the deposition of Ru and RuO ALD. Preliminary results achieved by Keith Gregorczyk illustrate the complex deposition mechanisms of depositing Ru within a PAA membrane. Ru ALD films were deposited at 250 °C using Ru(Cyprus)$^{TM}$ and molecular oxygen ($O_2$) on four different pretreated substrates: Si, $SiO_2$, $Al_2O_3$, and $TiO_2$. Planar results found that after 200 cycles of deposition, Ru was deposited on the Si, $SiO_2$, and $TiO_2$ films with a growth rate of ~0.5 Å/cycle with a very short nucleation time. However, films were extremely rough as seen by SEM images of the surface. Films deposited on $Al_2O_3$ coated wafers demonstrated a lengthy nucleation period of greater than 200 cycles, thus potentially leading to problems in using Ru as a bottom electrode in our MIM nanocapacitor work. We are currently investigating the use of a $TiO_2$ ALD nucleation layer under the Ru in order to push forward with the high-k rutile $TiO_2$ creating an insulator-metal-insulator-metal (IMIM) nanocapacitor. However, as with depositing any new chemistry the process metrics have to be optimized in order to find the optimal conditions for both extrinsic (growth rate, uniformity, conformality) and intrinsic (electrical, optical, compositional) properties for Ru ALD deposited across planar 2D wafers, as well as in ultra-high aspect ratio nanopores.

Future work in the commercial Beneq reactor encompasses pushing the limits of ALD conformality within ultra-high aspect ratio nanopores. The Beneq tool has been touted for it unprecedented conformality within high aspect ratio structures, however, this process metric has only been seen for ideal ALD chemistries $Al_2O_3$ and ZnO using high vapor pressure sources. Conformality studies of ZnO ALD deposited within PAA

membranes using diethylzinc (DEZ) and water has highlighted the complex adsorption/desorption mechanisms that can often be associated with using water as an oxidizing precursor. Results demonstrated that longer purge times during the ALD process allowed for the manipulation of film deposition down the length of a nanopore due to water's ability to physisorb multilayers. It was found that longer purge times assist in desorption of these multilayers, thus effecting the film's resulting film thickness and subsequent conformality within an ultra-high aspect ratio nanopore. This work could prove to be useful in the fabrication and design of new energy devices, such as solar cells.

Additional process optimization on the Beneq tool is being continued by Alex Kozen in order to further the conformality studies of ALD chemistries whose precursors require the use of a bubbler system due to their low vapor pressures. However, due to the virtual valving system the Beneq system employs it makes changing the precursor dose extremely difficult. It is has been discussed in this paper that the conformality within a high aspect ratio nanopore is dependent upon higher doses as well as higher surface residence times. Therefore, machinery to enforce a quasistatic flow is being introduced. ALD conformality is vital to next generation nanotechnology and requires the process development and optimization of many ALD processes.

# Appendices

## Appendix I. Substrate Temperature Calibration

Figure II. Calibration of ALD substrate heater as measured by a 13 point thermocouple wafer. a) Diagram of 100 mm 13 point SensArray™ thermocouple wafer. b) Wafer temperature as a function of controller temperature at 100 mTorr. c) Wafer temperature as a function of pressure at 175 °C setpoint temperature.

a)

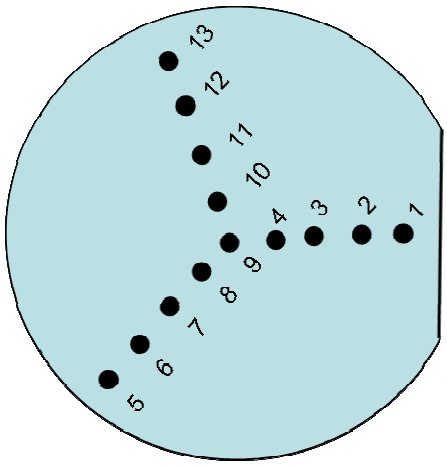

b)

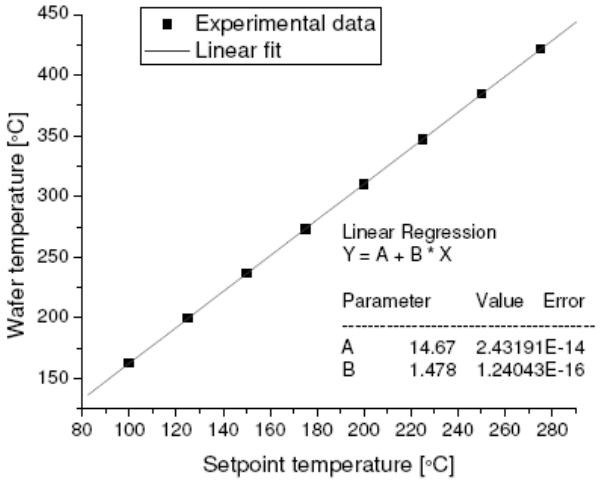
Experimental data
Linear fit
Linear Regression
Y = A + B * X
Parameter Value Error
A 14.67 2.43191E-14
B 1.478 1.24043E-16
Wafer temperature [°C]
Setpoint temperature [°C]

c)

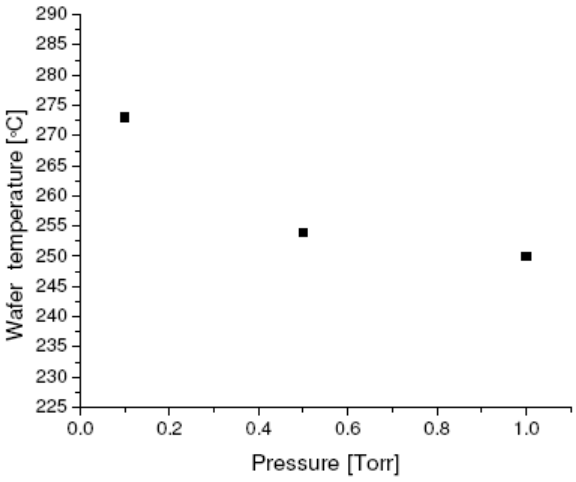
Wafer temperature [°C]
Pressure [Torr]

## Appendix II. Reactant Vapor Pressure

Figure III. Reactant vapor pressure vs temperture for titanium tetraisopropoxide (TTIP).

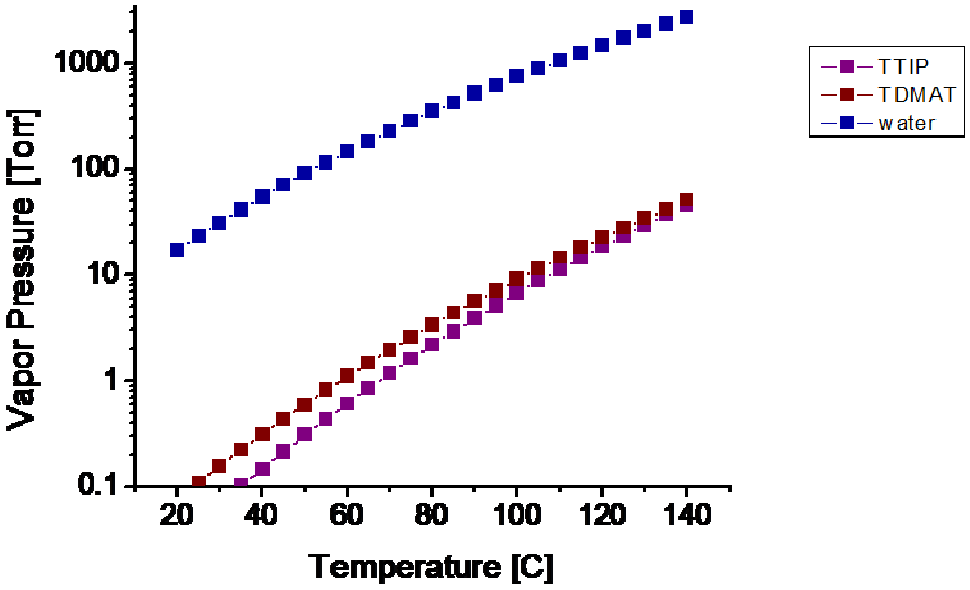


Vapor pressure laws for liquid precursors (Source: Air Liquide, France)

| | |
|---|---|
| TTIP | log P [Torr] = 9.465 - 3222/T [K] |
| TDMAT | log P [Torr] = 8.6 – 2850/T [K] |
| Water | log P [Torr] = 8.07 – 1730/T [K] |

## Appendix III. Trimethylaluminum (TMA) Gas Line Delivery System

Reproducible precursor doses of TMA were achieved by implementing a pressure end-point control system where each precursor vapor is introduced through a needle valve into a temperature-controlled volume. Upon reaching a given pressure setpoint, the inlet valve between the precursor and the volume was closed and the gases were released into the chamber for 0.3 s. The minimum and maximum pressures were monitored for each cycle in order to determine the number of µmols introduced into the system. After each pulse, any gas remaining between the fill valve and the needle valve, where dumped into the exhaust vacuum through a bypass valve.

Figure IV. Record of maximum and minimum pressures in TMA delivery volume over 100 cycles. Calculated doses (open diamonds) are shown on the right axis.

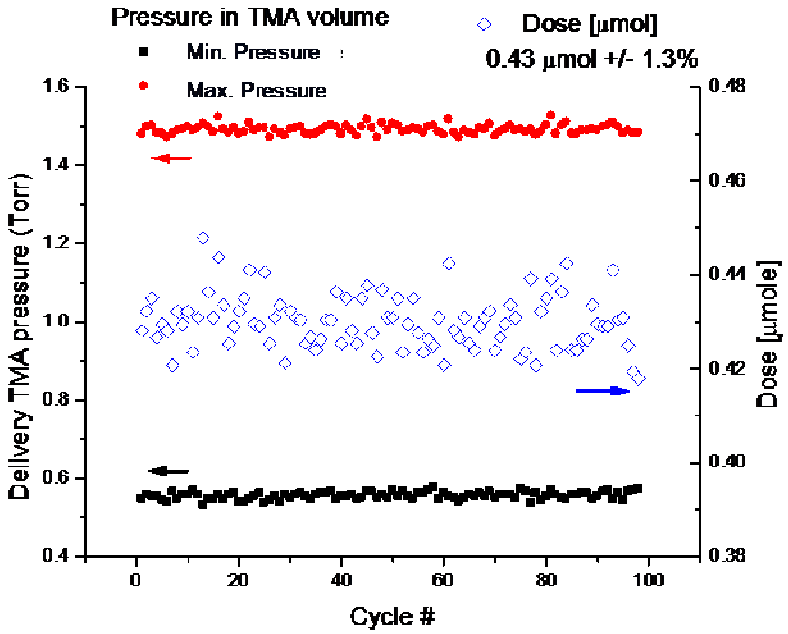

## Appendix IV. Calibration of Ozone Dose

Figure V. Calibration of Ozone does is only controlled by a needle valve and exposure time. Compared the pressure increase in the mini-reactor ($P_{RGA}$) during known TMA doses and $O_3$ pulses to establish exact $O_3$ does in mols (done in conditions where no chemical reactions occurred). Calculated integrated peak for $P_{RGA}$ under different known TMA doses to establish regression.

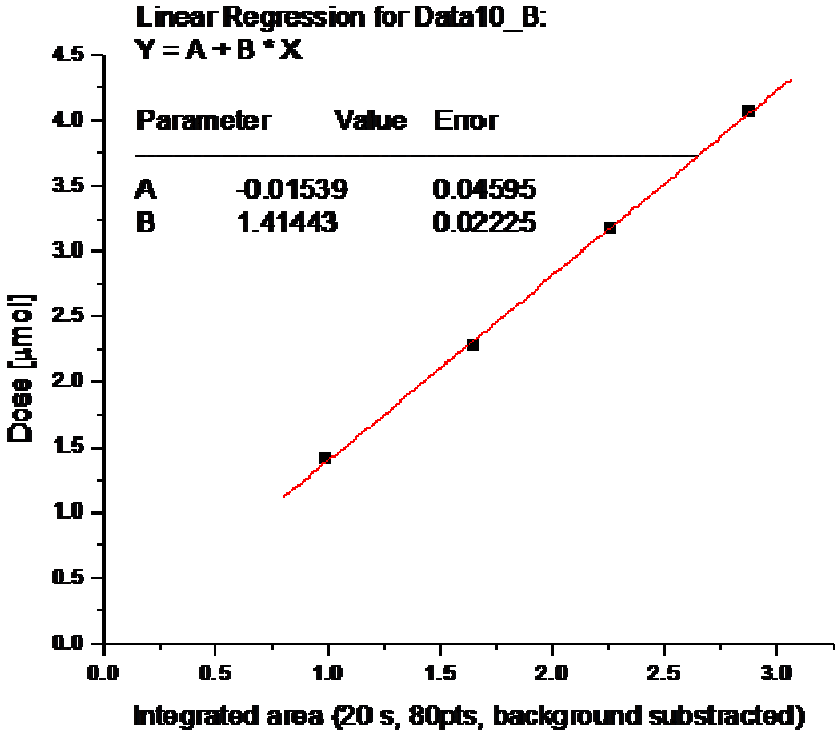

## Appendix V. $HfO_2$ ALD Nanotube Fabrication[44]

A porous AAO template was synthesized by a two-step anodization method.[79]. In brief, a piece of electropolished aluminum foil (99.99%, Alfa Aesar) was anodized at 40V and 10°C in an electrolytic bath of 0.3M oxalic acid. In the first step of the anodization process, the foil was anodized for long enough (~ 7 hours) so that the pores were ordered and growing orthogonally with respect to the substrate. The AAO film that was created was then etched off by an aqueous mixture of phosphoric acid (6 wt %) and chromic acid (1.8 wt %), leaving a pre-textured and ordered aluminum surface. In the second step of the anodization process, the foil was anodized for a set amount of time (~1 hour) defining the depth of the pores to be ~4um. Pore diameters were adjusted to ~60 nm using a pore-widening solution of phosphoric acid (0.1 M) at 38 °C. Membranes were not detached from the substrate before ALD processing and therefore its nanopores only had one open end.

High-K dielectric $HfO_2$ thin films were deposited by alternating reactant exposures of tetrakis(ethylmethylamino)hafnium (TEMAH), that is, $Hf[N(CH_3)(C_2H_5)]_4$ [99.99% grade, Sigma Aldrich], as the organometallic precursor and DI water as an oxidant. The ALD equipment consists of a stainless steel tube (25" in length and 3" in diameter) in a tube furnace. Precursors and nitrogen gases were introduced through one end of the reactor, while un-reacted precursors and reaction byproducts were exhausted at the opposite end of the tube to a rotary vane vacuum pump. Substrates were introduced into the system through a removable flange at the exhaust end of the reactor. The wafer temperature was measured via a thermocouple to be 200 ˚C. During each of the self-

limited half reactions corresponding to the alternating exposures of TEMAH and water, reactants were dosed to achieve full surface saturation resulting in excellent thickness control at the atomic level as a sub-monolayer of oxide was consistently deposited for each cycle.

A reservoir containing 5 g of liquid TEMAH was placed in an incubation oven set to 105 ˚C to achieve a vapor pressure of approximately 2 Torr. Prior to each exposure, the TEMAH gas was fed into a 20 mL isothermal volume and TEMAH doses were controlled by timing the opening of a pneumatically actuated valve. A 0.85 µmol dose of TEMAH was determined to be sufficient to achieve full saturation on a Si substrate located in next to the AAO template. In the case of water, the vessel was kept at room temperature. Accurate water dosage was achieved by filling up a 20 mL isothermal volume up to a targeted pressure monitored by a capacitance gauge and then discharging the gas into the reactor for a fixed amount of time. This pressure end-point control approach was required to minimize the effect of the cooling of the water source over the process duration due to the forced vaporization of the precursor and the resulting decrease of its vapor pressure. Full saturation was achieved by filling up the volume at 7 Torr. We estimate the partial pressures of both the water and TEMAH doses to be ~7 mTorr from the pressure spike recorded by a downstream pressure sensor (average change in pressure over peak width).

Throughout the deposition process, 30 sccm of nitrogen was continuously flowed into the reactor maintaining a reactor pressure of 96 mTorr. A growth rate of 1 Å cycle$^{-1}$ was achieved over 100 cycle process. Prior to each pulse, a 10 s $N_2$ purge was initiated to ensure that un-reacted precursor and reaction byproduct, mainly $(CH_3)(C_2H_5)NH$, were

adequately purge out of the reactor.

After ALD deposition, samples were place in 0.1M NaOH solution for 1 hour which dissolved away the alumina membrane freeing the $HfO_2$ film in solution. After filtration with DI water, a drop of the solution was placed on a carbon coated Cu TEM grid.

# References


[1] M. Leskela and M. Ritala, "Atomic layer deposition (ALD): from precursors to thin film structures," *Thin Solid Films,* vol. 409, pp. 138-146, 2002.

[2] L. Niinisto, J. Paivasaari, J. Niinisto, M. Putkonen, and M. Nieminen, "Advanced electronic and optoelectronic materials by Atomic Layer Deposition: An overview with special emphasis on recent progress in processing of high-k dielectrics and other oxide materials," *Physica Status Solidi a-Applied Research,* vol. 201, pp. 1443-1452, 2004.

[3] H. Kim, H. B. R. Lee, and W. J. Maeng, "Applications of atomic layer deposition to nanofabrication and emerging nanodevices," *Thin Solid Films,* vol. 517, pp. 2563-2580, 2009.

[4] R. L. Puurunen, "Surface chemistry of atomic layer deposition: A case study for the trimethylaluminum/water process," *Journal of Applied Physics,* vol. 97, 2005.

[5] M. Leskela, M. Kemell, K. Kukli, V. Pore, E. Santala, M. Ritala, and J. Lu, "Exploitation of atomic layer deposition for nanostructured materials," *Materials Science & Engineering C-Biomimetic and Supramolecular Systems,* vol. 27, pp. 1504-1508, 2007.

[6] O. Sneh, M. A. Cameron, and S. M. George, "Adsorption and desorption kinetics of H2O on a fully hydroxylated SiO2 surface," *Surface Science,* vol. 364, pp. 61-78, 1996.

[7] O. Sneh, R. B. Clark-Phelps, A. R. Londergan, J. Winkler, and T. E. Seidel, "Thin film atomic layer deposition equipment for semiconductor processing," *Thin Solid Films,* vol. 402, pp. 248-261, 2002.

[8] G. D. Wilk, R. M. Wallace, and J. M. Anthony, "High-kappa gate dielectrics: Current status and materials properties considerations," *Journal of Applied Physics,* vol. 89, pp. 5243-5275, 2001.

[9] E. Gerritsen, N. Emonet, C. Caillat, N. Jourdan, M. Piazza, D. Fraboulet, B. Boeck, A. Berthelot, S. Smith, and P. Mazoyer, "Evolution of materials technology for stacked-capacitors in 65 nm embedded-DRAM," *Solid-State Electronics,* vol. 49, pp. 1767-1775, 2005.

[10] M. Leskela and M. Ritala, "Atomic layer deposition chemistry: Recent developments and future challenges," *Angewandte Chemie-International Edition,* vol. 42, pp. 5548-5554, 2003.

[11] M. Schumacher, P. K. Baumann, and T. Seidel, "AVD and ALD as two complementary technology solutions for next generation dielectric and conductive thin-film processing," *Chemical Vapor Deposition,* vol. 12, pp. 99-108, 2006.

[12] M. Knez, K. Niesch, and L. Niinisto, "Synthesis and surface engineering of complex nanostructures by atomic layer deposition," *Advanced Materials,* vol. 19, pp. 3425-3438, 2007.

[13] C. R. Manoj and V. R. Rao, "Impact of high-k gate dielectrics on the device and circuit performance of nanoscale FinFETs," *Ieee Electron Device Letters,* vol. 28,

pp. 295-297, 2007.
[14] S. K. Kim, G. J. Choi, J. H. Kim, and C. S. Hwang, "Growth behavior of Al-doped TiO2 thin films by atomic layer deposition," *Chemistry of Materials,* vol. 20, pp. 3723-3727, 2008.
[15] D. M. King, X. H. Du, A. S. Cavanagh, and A. Weimer, "Quantum confinement in amorphous TiO2 films studied via atomic layer deposition," *Nanotechnology,* vol. 19, p. 6, Nov 2008.
[16] J. S. King, D. Heineman, E. Graugnard, and C. J. Summers, "Atomic layer deposition in porous structures: 3D photonic crystals," *Applied Surface Science,* vol. 244, pp. 511-516, 2005.
[17] M. Kemell, V. Pore, M. Ritala, M. Leskela, and M. Linden, "Atomic layer deposition in nanometer-level replication of cellulosic substances and preparation of photocatalytic TiO2/cellulose composites," *Journal of the American Chemical Society,* vol. 127, pp. 14178-14179, 2005.
[18] M. J. Pellin, P. C. Stair, G. Xiong, J. W. Elam, J. Birrell, L. Curtiss, S. M. George, C. Y. Han, L. Iton, H. Kung, M. Kung, and H. H. Wang, "Mesoporous catalytic membranes: Synthetic control of pore size and wall composition," *Catalysis Letters,* vol. 102, pp. 127-130, 2005.
[19] E. Santala, M. Kemell, M. Leskela, and M. Ritala, "The preparation of reusable magnetic and photocatalytic composite nanofibers by electrospinning and atomic layer deposition," *Nanotechnology,* vol. 20, 2009.
[20] P. Banerjee, Perez, I., Robertson, E., Lee, S.B., Rubloff, G.W., "Lateral two terminal nanotube devices and method for their formation," U.S., 2007.
[21] P. Banerjee, Perez, I., Henn-Lecordier, L., Lee, S.B., Rubloff, G.W., "Nanotubular metal-insulator-metal capacitor arrays for energy storage," *Nature Nanotechnology,* vol. 4, pp. 292-296, 2009.
[22] P. Banerjee, Perez, I., Henn-Lecordier, L., Lee, S.B., Rubloff, G.W., "ALD based metal-insulator-metal (MIM) nanocapacitors for energy storage," *ECS Transactions,* 2009.
[23] C. Nistorica, J. F. Liu, I. Gory, G. D. Skidmore, F. M. Mantiziba, B. E. Gnade, and J. Kim, "Tribological and wear studies of coatings fabricated by atomic layer deposition and by successive ionic layer adsorption and reaction for microelectromechanical devices," *Journal of Vacuum Science & Technology A,* vol. 23, pp. 836-840, 2005.
[24] C. F. Herrmann, F. W. DelRio, D. C. Miller, S. M. George, V. M. Bright, J. L. Ebel, R. E. Strawser, R. Cortez, and K. D. Leedy, "Alternative dielectric films for rf MEMS capacitive switches deposited using atomic layer deposited Al2O3/ZnO alloys," *Sensors and Actuators a-Physical,* vol. 135, pp. 262-272, 2007.
[25] T. M. Mayer, J. W. Elam, S. M. George, P. G. Kotula, and R. S. Goeke, "Atomic-layer deposition of wear-resistant coatings for microelectromechanical devices," *Applied Physics Letters,* vol. 82, pp. 2883-2885, 2003.
[26] N. D. Hoivik, J. W. Elam, R. J. Linderman, V. M. Bright, S. M. George, and Y. C. Lee, "Atomic layer deposited protective coatings for micro-electromechanical systems," *Sensors and Actuators a-Physical,* vol. 103, pp. 100-108, 2003.
[27] J. F. Liu, C. Nistorica, I. Gory, G. Skidmore, F. M. Mantiziba, and B. E. Gnade, "Layer-by-layer deposition of zirconium oxide films from aqueous solutions for

friction reduction in silicon-based micro electromechanical system devices," *Thin Solid Films,* vol. 492, pp. 6-12, 2005.

[28] A. Javey, H. Kim, M. Brink, Q. Wang, A. Ural, J. Guo, P. McIntyre, P. McEuen, M. Lundstrom, and H. J. Dai, "High-kappa dielectrics for advanced carbon-nanotube transistors and logic gates," *Nature Materials,* vol. 1, pp. 241-246, 2002.

[29] J. S. Lee, B. Min, K. Cho, S. Kim, J. Park, Y. T. Lee, N. S. Kim, M. S. Lee, S. O. Park, and J. T. Moon, "Al2O3 nanotubes and nanorods fabricated by coating and filling of carbon nanotubes with atomic-layer deposition," *Journal of Crystal Growth,* vol. 254, pp. 443-448, 2003.

[30] R. Artzi-Gerlitz, K. D. Benkstein, D. L. Lahr, J. L. Hertz, C. B. Montgomery, J. E. Bonevich, S. Semancik, and M. J. Tarlov, "Fabrication and gas sensing performance of parallel assemblies of metal oxide nanotubes supported by porous aluminum oxide membranes," *Sensors and Actuators B-Chemical,* vol. 136, pp. 257-264, 2009.

[31] M. A. Cameron, I. P. Gartland, J. A. Smith, S. F. Diaz, and S. M. George, "Atomic layer deposition of SiO2 and TiO2 in alumina tubular membranes: Pore reduction and effect of surface species on gas transport," *Langmuir,* vol. 16, pp. 7435-7444, 2000.

[32] J. D. Ferguson, A. W. Weimer, and S. M. George, "Atomic layer deposition of ultrathin and conformal Al2O3 films on BN particles," *Thin Solid Films,* vol. 371, pp. 95-104, 2000.

[33] D. M. King, X. H. Liang, Y. Zhou, C. S. Carney, L. F. Hakim, P. Li, and A. W. Weimer, "Atomic layer deposition of TiO2 films on particles in a fluidized bed reactor," *Powder Technology,* vol. 183, pp. 356-363, 2008.

[34] J. D. Ferguson, A. W. Weimer, and S. M. George, "Atomic layer deposition of SiO2 films on BN particles using sequential surface reactions," *Chemistry of Materials,* vol. 12, pp. 3472-3480, 2000.

[35] J. D. Ferguson, A. W. Weimer, and S. M. George, "Atomic layer deposition of Al2O3 films on polyethylene particles," *Chemistry of Materials,* vol. 16, pp. 5602-5609, 2004.

[36] J. D. Ferguson, A. R. Yoder, A. W. Weimer, and S. M. George, "TiO2 atomic layer deposition on ZrO2 particles using alternating exposures of TiCl4 and H2O," *Applied Surface Science,* vol. 226, pp. 393-404, 2004.

[37] A. Johansson, T. Torndahl, L. M. Ottosson, M. Boman, and J. O. Carlsson, "Copper nanoparticles deposited inside the pores of anodized aluminium oxide using atomic layer deposition," *Materials Science & Engineering C-Biomimetic and Supramolecular Systems,* vol. 23, pp. 823-826, 2003.

[38] A. Johansson, J. Lu, J. O. Carlsson, and M. Boman, "Deposition of palladium nanoparticles on the pore walls of anodic alumina using sequential electroless deposition," *Journal of Applied Physics,* vol. 96, pp. 5189-5194, 2004.

[39] J. Biener, T. F. Baumann, Y. M. Wang, E. J. Nelson, S. O. Kucheyev, A. V. Hamza, M. Kemell, M. Ritala, and M. Leskela, "Ruthenium/aerogel nanocomposites via atomic layer deposition," *Nanotechnology,* vol. 18, 2007.

[40] R. G. Gordon, J. Becker, D. Hausmann, and S. Suh, "Vapor deposition of metal oxides and silicates: Possible gate insulators for future microelectronics," *Chemistry of Materials,* vol. 13, pp. 2463-2464, 2001.

[41] A. W. Ott, J. W. Klaus, J. M. Johnson, S. M. George, K. C. McCarley, and J. D. Way, "Modification of porous alumina membranes using Al2O3 atomic layer controlled deposition," *Chemistry of Materials,* vol. 9, pp. 707-714, 1997.

[42] R. L. Puurunen, W. Vandervorst, W. F. A. Besling, O. Richard, H. Bender, T. Conard, C. Zhao, A. Delabie, M. Caymax, S. De Gendt, M. Heyns, M. M. Viitanen, M. de Ridder, H. H. Brongersma, Y. Tamminga, T. Dao, T. de Win, M. Verheijen, M. Kaiser, and M. Tuominen, "Island growth in the atomic layer deposition of zirconium oxide and aluminum oxide on hydrogen-terminated silicon: Growth mode modeling and transmission electron microscopy," *Journal of Applied Physics,* vol. 96, pp. 4878-4889, 2004.

[43] D. R. G. Mitchell, G. Triani, D. J. Attard, K. S. Finnie, P. J. Evans, C. J. Barbe, and J. R. Bartlett, "Atomic layer deposition of TiO2 and Al2O3 thin films and nanolaminates," *Smart Materials & Structures,* vol. 15, pp. S57-S64, 2006.

[44] I. Perez, E. Robertson, P. Banerjee, L. Henn-Lecordier, S. J. Son, S. B. Lee, and G. W. Rubloff, "TEM-based metrology for HfO2 layers and nanotubes formed in anodic aluminum oxide nanopore structures," *Small,* vol. 4, pp. 1223-1232, 2008.

[45] L. Nyns, A. Delabie, M. Caymax, M. M. Heyns, S. Van Elshocht, C. Vinckier, and S. De Gendt, "HfO2 Atomic Layer Deposition Using HfCl4/H2O: The First Reaction Cycle," *Journal of the Electrochemical Society,* vol. 155, pp. G269-G273, 2008.

[46] W. J. Maeng and H. Kim, "Electrical properties of atomic layer deposition HfO2 and HfOxNy on si substrates with various crystal orientations," *Journal of the Electrochemical Society,* vol. 155, pp. H267-H271, 2008.

[47] X. Y. Liu, S. Ramanathan, A. Longdergan, A. Srivastava, E. Lee, T. E. Seidel, J. T. Barton, D. Pang, and R. G. Gordon, "AID of hafnium oxide thin film from tetrakis(ethylmethylamino)hafnium and ozone," *Journal of the Electrochemical Society,* vol. 152, pp. G213-G219, 2005.

[48] W. J. Maeng and H. Kim, "Thermal and plasma-enhanced ALD of Ta and Ti oxide thin films from alkylamide precursors," *Electrochemical and Solid State Letters,* vol. 9, pp. G191-G194, 2006.

[49] M. Kemell, E. Harkonen, V. Pore, M. Ritala, and M. Leskela, "Ta2O5- and TiO2-based nanostructures made by atomic layer deposition," *Nanotechnology,* vol. 21.

[50] J. W. Elam, J. A. Libera, M. J. Pellin, A. V. Zinovev, J. P. Greene, and J. A. Nolen, "Atomic layer deposition of W on nanoporous carbon aerogels," *Applied Physics Letters,* vol. 89, 2006.

[51] R. K. Grubbs, C. E. Nelson, N. J. Steinmetz, and S. M. George, "Nucleation and growth during the atomic layer deposition of W on Al2O3 and Al2O3 on W," *Thin Solid Films,* vol. 467, pp. 16-27, 2004.

[52] W. Lei, L. Henn-Lecordier, M. Anderle, G. W. Rubloff, M. Barozzi, and M. Bersani, "Real-time observation and optimization of tungsten atomic layer deposition process cycle," *Journal of Vacuum Science & Technology B,* vol. 24, pp. 780-789, 2006.

[53] J. W. Elam, C. E. Nelson, R. K. Grubbs, and S. M. George, "Nucleation and growth during tungsten atomic layer deposition on SiO2 surfaces," *Thin Solid Films,* vol. 386, pp. 41-52, 2001.

[54] A. Rahtu and M. Ritala, "Reaction mechanism studies on titanium isopropoxide-water atomic layer deposition process," *Chemical Vapor Deposition,* vol. 8, pp. 21-28, 2002.
[55] A. Palma and A. Alavi, "An ab initio study of titanium tetra-iso-propoxide (TTIP) adsorption mechanism on a Si(100) surface," *Computational Materials Science,* vol. 33, pp. 244-249, 2005.
[56] V. R. Rai and S. Agarwal, "Surface reaction mechanisms during ozone-based atomic layer deposition of titanium dioxide," *Journal of Physical Chemistry C,* vol. 112, pp. 9552-9554, 2008.
[57] V. R. Rai and S. Agarwal, "Surface Reaction Mechanisms during Plasma-Assisted Atomic Layer Deposition of Titanium Dioxide," *Journal of Physical Chemistry C,* vol. 113, pp. 12962-12965, Jul 2009.
[58] C. Ducso, N. Q. Khanh, Z. Horvath, I. Barsony, M. Utriainen, S. Lehto, M. Nieminen, and L. Niinisto, "Deposition of tin oxide into porous silicon by atomic layer epitaxy," *Journal of the Electrochemical Society,* vol. 143, pp. 683-687, 1996.
[59] S. K. Kim, C. S. Hwang, S. H. K. Park, and S. J. Yun, "Comparison between ZnO films grown by atomic layer deposition using H2O or O-3 as oxidant," *Thin Solid Films,* vol. 478, pp. 103-108, 2005.
[60] J. H. Kim, D. S. Kil, S. J. Yeom, J. S. Roh, N. J. Kwak, and J. W. Kim, "Modified atomic layer deposition of RuO2 thin films for capacitor electrodes," *Applied Physics Letters,* vol. 91, 2007.
[61] J. W. Elam, A. Zinovev, C. Y. Han, H. H. Wang, U. Welp, J. N. Hryn, and M. J. Pellin, "Atomic layer deposition of palladium films on Al2O3 surfaces," *Thin Solid Films,* vol. 515, pp. 1664-1673, 2006.
[62] A. C. Jones, H. C. Aspinall, P. R. Chalker, R. J. Potter, T. D. Manning, Y. F. Loo, R. O'Kane, J. M. Gaskell, and L. M. Smith, "MOCVD and ALD of high-kappa dielectric oxides using alkoxide precursors," *Chemical Vapor Deposition,* vol. 12, pp. 83-98, 2006.
[63] S. M. George, "Atomic Layer Deposition: An Overview," *Chemical Reviews,* vol. 110, pp. 111-131, Jan.
[64] M. Ylilammi, "Monolayer thickness in atomic layer deposition," *Thin Solid Films,* vol. 279, pp. 124-130, 1996.
[65] M. Y. Li, Y. Y. Chang, H. C. Wu, C. S. Huang, J. C. Chen, J. L. Lue, and S. M. Chang, "Effect of process pressure on atomic layer deposition of Al2O3," *Journal of the Electrochemical Society,* vol. 154, pp. H967-H972, 2007.
[66] R. G. Gordon, D. Hausmann, E. Kim, and J. Shepard, "A kinetic model for step coverage by atomic layer deposition in narrow holes or trenches," *Chemical Vapor Deposition,* vol. 9, pp. 73-78, 2003.
[67] J. W. Elam, D. Routkevitch, P. P. Mardilovich, and S. M. George, "Conformal coating on ultrahigh-aspect-ratio nanopores of anodic alumina by atomic layer deposition," *Chemistry of Materials,* vol. 15, pp. 3507-3517, 2003.
[68] L. Henn-Lecordier, M. Anderle, E. Robertson, and G. W. Rubloff, "Exploring the limits of atomic layer deposition: the process window for Al2O3 ALD from TMA and H2O," *Chemical Vapor Deposition,* submitted.
[69] J. F. O'Hanlon, *A User's Guide to Vacuum Technology*, 2nd ed. New York: John

Wiley & Sons, 1989.
[70] J. W. Diggle, T. C. Downie, and C. W. Goulding, "ANODIC OXIDE FILMS ON ALUMINUM," *Chemical Reviews,* vol. 69, pp. 365-&, 1969.
[71] G. E. Thompson, "Porous anodic alumina: Fabrication, characterization and applications," *Thin Solid Films,* vol. 297, pp. 192-201, 1997.
[72] H. Masuda and K. Fukuda, "Ordered Metal Nanohole Arrays Made By a 2-step Replication of Honeycomb Structures of Anodic Alumina," *Science,* vol. 268, pp. 1466-1468, 1995.
[73] W. Lee, K. Nielsch, and U. Gosele, "Self-ordering behavior of nanoporous anodic aluminum oxide (AAO) in malonic acid anodization," *Nanotechnology,* vol. 18, Nov 2007.
[74] A. P. Li, F. Muller, A. Birner, K. Nielsch, and U. Gosele, "Hexagonal pore arrays with a 50-420 nm interpore distance formed by self-organization in anodic alumina," *Journal of Applied Physics,* vol. 84, pp. 6023-6026, 1998.
[75] K. S. Kang, Y. S. Meng, J. Breger, C. P. Grey, and G. Ceder, "Electrodes with high power and high capacity for rechargeable lithium batteries," *Science,* vol. 311, pp. 977-980, 2006.
[76] C. Liu, F. Li, L. P. Ma, and H. M. Cheng, "Advanced Materials for Energy Storage," *Advanced Materials,* vol. 22, pp. E28-+.
[77] R. Liu, S. Il Cho, and S. B. Lee, "Poly( 3,4-ethylenedioxythiophene) nanotubes as electrode materials for a high-powered supercapacitor," *Nanotechnology,* vol. 19, 2008.
[78] L. Henn-Lecordier, W. Lei, M. Anderle, and G. W. Rubloff, "Real-time sensing and metrology for atomic layer deposition processes and manufacturing," *Journal of Vacuum Science & Technology B,* vol. 25, pp. 130-139, 2007.
[79] H. Masuda and M. Satoh, "Fabrication of gold nanodot array using anodic porous alumina as an evaporation mask," *Japanese Journal of Applied Physics Part 2-Letters,* vol. 35, pp. L126-L129, Jan 1996.
[80] E. Langereis, S. B. S. Heil, H. C. M. Knoops, W. Keuning, M. C. M. van de Sanden, and W. M. M. Kessels, "In situ spectroscopic ellipsometry as a versatile tool for studying atomic layer deposition," *Journal of Physics D-Applied Physics,* vol. 42, 2009.
[81] J.A. Woollam Co., Inc., http://www.jawoollam.com/tutorial_1.html, March 20, 2010
[82] H. G. Tompkins and W. A. McGahan, *Spectroscopic ellipsometry and reflectometry, a user's guide*: Wiley-Interscience, 1999.
[83] Trinity College School of Physics, http://www.tcd.ie/Physics/Surfaces/ellipsometry2.php, March 20, 2010
[84] W. Vanderlinde, "SEM Short Course: Scanning Electron Microscopy," College Park: Laboratory for Physical Sciences, 2008.
[85] R. Egerton, *Physical Principles of Electron Microscopy: An Introduction to TEM, SEM, AEM*. New York: Springer, 2007.
[86] P. Flewitt and R. Wild, *Physical Methods For Materials Characterization*. Philadelphia: IOP Publishing, 2003.
[87] Purdu University, http://www.purdue.edu/REM/rs/sem.htm, March 30, 2010
[88] University of Nebraska-Lincoln, http://www.unl.edu/CMRAcfem/temoptic.htm,

March 30, 2010
[89] W. Vanderlinde, "SEM Short Course: Energy Dispersive X-ray Analysis," Laboratory for Physical Sciences, 2008.
[90] Oxford Instruments PLC, http://www.x-raymicroanalysis.com/x-ray-microanalysis-explained/pages/tutorial3/interaction.htm, 2010
[91] Galloway, "Atomic Force Microscopy: A Guide to Understanding and Using the AFM," 2004.
[92] Wikipedia, http://en.wikipedia.org/wiki/Atomic_force_microscopy, March 31, 2010
[93] R. Liu and S. B. Lee, "MnO2/Poly(3,4-ethylenedioxythiophene) coaxial nanowires by one-step coelectrodeposition for electrochemical energy storage," *Journal of the American Chemical Society,* vol. 130, pp. 2942-2943, 2008.
[94] J. W. Elam, G. Xiong, C. Y. Han, H. H. Wang, J. P. Birrell, U. Welp, J. N. Hryn, M. J. Pellin, T. F. Baumann, J. F. Poco, and J. H. Satcher, "Atomic layer deposition for the conformal coating of nanoporous materials," *Journal of Nanomaterials,* 2006.
[95] R. Rosenberg, D. C. Edelstein, C. K. Hu, and K. P. Rodbell, "Copper metallization for high performance silicon technology," *Annual Review of Materials Science,* vol. 30, pp. 229-262, 2000.
[96] S. M. Gates, "Surface chemistry in the chemical vapor deposition of electronic materials," *Chemical Reviews,* vol. 96, pp. 1519-1532, 1996.
[97] H. Masuda, H. Yamada, M. Satoh, H. Asoh, M. Nakao, and T. Tamamura, "Highly ordered nanochannel-array architecture in anodic alumina," *Applied Physics Letters,* vol. 71, pp. 2770-2772, 1997.
[98] A. B. F. Martinson, J. W. Elam, J. T. Hupp, and M. J. Pellin, "ZnO nanotube based dye-sensitized solar cells ZnO nanotube based dye-sensitized solar cells," *Nano Letters,* vol. 7, pp. 2183-2187, 2007.
[99] Y. K. Zhou, C. M. Shen, and H. L. Li, "Synthesis of high-ordered LiCoO2 nanowire arrays by AAO template," *Solid State Ionics,* vol. 146, pp. 81-86, 2002.
[100] H. Masuda, F. Hasegwa, and S. Ono, "Self-ordering of cell arrangement of anodic porous alumina formed in sulfuric acid solution," *Journal of the Electrochemical Society,* vol. 144, pp. L127-L130, 1997.
[101] M. K. Gobbert, V. Prasad, and T. S. Cale, "Predictive modeling of atomic layer deposition on the feature scale," *Thin Solid Films,* vol. 410, pp. 129-141, 2002.
[102] H. Asoh, K. Nishio, M. Nakao, T. Tamamura, and H. Masuda, "Conditions for fabrication of ideally ordered anodic porous alumina using pretextured Al," *Journal of the Electrochemical Society,* vol. 148, pp. B152-B156, 2001.
[103] W. Lee, R. Ji, U. Gosele, and K. Nielsch, "Fast fabrication of long-range ordered porous alumina membranes by hard anodization," *Nature Materials,* vol. 5, pp. 741-747, 2006.
[104] Q. Xie, J. Musschoot, D. Deduytsche, R. L. Van Meirhaeghe, C. Detavernier, S. Van den Berghe, Y. L. Jiang, G. P. Ru, B. Z. Li, and X. P. Qu, "Growth kinetics and crystallization behavior of TiO2 films prepared by plasma enhanced atomic layer deposition," *Journal of the Electrochemical Society,* vol. 155, pp. H688-H692, 2008.
[105] Q. Xie, Y. L. Jiang, C. Detavernier, D. Deduytsche, R. L. Van Meirhaeghe, G. P.

Ru, B. Z. Li, and X. P. Qu, "Atomic layer deposition of TiO2 from tetrakis-dimethyl-amido titanium or Ti isopropoxide precursors and H2O," *Journal of Applied Physics,* vol. 102, 2007.

[106] A. Niskanen, K. Arstila, M. Leskela, and M. Ritala, "Radical enhanced atomic layer deposition of titanium dioxide," *Chemical Vapor Deposition,* vol. 13, pp. 152-157, 2007.

[107] L. K. Tan, H. Gao, Y. Zong, and W. Knoll, "Atomic Layer Deposition of TiO2 to Bond Free-Standing Nanoporous Alumina Templates to Gold-Coated Substrates as Planar Optical Waveguide Sensors," *Journal of Physical Chemistry C,* vol. 112, pp. 17576-17580, 2008.

[108] I. Jogi, K. Kukli, J. Aarik, A. Aidla, and J. Lu, "Precursor-dependent structural and electrical characteristics of atomic layer deposited films: Case study on titanium oxide," *Materials Science in Semiconductor Processing,* vol. 9, pp. 1084-1089, 2006.

[109] S. Duenas, H. Castan, H. Garcia, E. San Andres, M. Toledano-Luque, I. Martil, G. Gonzalez-Diaz, K. Kukli, T. Uustare, and J. Aarik, "A comparative study of the electrical properties of TiO2 films grown by high-pressure reactive sputtering and atomic layer deposition," *Semiconductor Science and Technology,* vol. 20, pp. 1044-1051, 2005.

[110] G. A. Battiston, R. Gerbasi, A. Gregori, M. Porchia, S. Cattarin, and G. A. Rizzi, "PECVD of amorphous TiO2 thin films: effect of growth temperature and plasma gas composition," *Thin Solid Films,* vol. 371, pp. 126-131, 2000.

[111] N. G. Kubala, P. C. Rowlette, and C. A. Wolden, "Self-Limiting Deposition of Anatase TiO2 at Low Temperature by Pulsed PECVD," *Electrochemical and Solid State Letters,* vol. 12, pp. H259-H262, 2009.

[112] M. Ritala, M. Leskela, L. Niinisto, and P. Haussalo, "TITANIUM ISOPROPOXIDE AS A PRECURSOR IN ATOMIC LAYER EPITAXY OF TITANIUM-DIOXIDE THIN-FILMS," *Chemistry of Materials,* vol. 5, pp. 1174-1181, 1993.

[113] J. Aarik, A. Aidla, T. Uustare, M. Ritala, and M. Leskela, "Titanium isopropoxide as a precursor for atomic layer deposition: characterization of titanium dioxide growth process," *Applied Surface Science,* vol. 161, pp. 385-395, 2000.

[114] K. Bange, C. R. Ottermann, O. Anderson, U. Jeschkowski, M. Laube, and R. Feile, "INVESTIGATIONS OF TIO2 FILMS DEPOSITED BY DIFFERENT TECHNIQUES," *Thin Solid Films,* vol. 197, pp. 279-285, 1991.

[115] G. T. Lim and D. H. Kim, "Characteristics of TiOx films prepared by chemical vapor deposition using tetrakis-dimethyl-amido-titanium and water," *Thin Solid Films,* vol. 498, pp. 254-258, 2006.

[116] J. H. Kwon, M. Dai, M. D. Halls, and Y. J. Chabal, "Detection of a formate surface intermediate in the atomic layer deposition of high-k dielectrics using ozone," *Chemistry of Materials,* vol. 20, pp. 3248-3250, 2008.

[117] R. Katamreddy, R. Inman, G. Jursich, A. Soulet, and C. Takoudis, "Atomic layer deposition of HfO2, Al2O3, and HfAlOx using O-3 and metal(diethylamino) precursors," *Journal of Materials Research,* vol. 22, pp. 3455-3464, 2007.

[118] S. K. Kim, S. Y. Lee, M. Seo, G. J. Choi, and C. S. Hwang, "Impact of O-3

feeding time on TiO2 films grown by atomic layer deposition for memory capacitor applications," *Journal of Applied Physics,* vol. 102, 2007.
[119] C. R. Ottermann and K. Bange, "Correlation between the density of TiO2 films and their properties," *Thin Solid Films,* vol. 286, pp. 32-34, 1996.
[120] A. W. Ott, J. W. Klaus, J. M. Johnson, and S. M. George, "Al3O3 thin film growth on Si(100) using binary reaction sequence chemistry," *Thin Solid Films,* vol. 292, pp. 135-144, 1997.
[121] R. Matero, A. Rahtu, M. Ritala, M. Leskela, and T. Sajavaara, "Effect of water dose on the atomic layer deposition rate of oxide thin films," *Thin Solid Films,* vol. 368, pp. 1-7, 2000.
[122] M. Rose, J. Niinisto, I. Endler, J. W. Bartha, P. Kucher, and M. Ritala, "In Situ Reaction Mechanism Studies on Ozone-Based Atomic Layer Deposition of Al2O3 and HfO2," *Acs Applied Materials & Interfaces,* vol. 2, pp. 347-350.
[123] D. N. Goldstein, J. A. McCormick, and S. M. George, "Al2O3 Atomic Layer Deposition with Trimethylaluminum and Ozone Studied by in Situ Transmission FTIR Spectroscopy and Quadrupole Mass Spectrometry," *Journal of Physical Chemistry C,* vol. 112, pp. 19530-19539, 2008.
[124] E. Langereis, W. Keuning, S. Rushworth, A.Kingsley, F. Roozeboom, M. C. M. v. d. Sanden, and W. M. M. Kessels, "Remote plasma ALD of $TiO_2$ and $SrTiO_3$: Ti precursor evaluation and substrate temperature dependence," in *ALD AVS* Monterey, CA, 2009.
[125] S. K. Kim, W. D. Kim, K. M. Kim, C. S. Hwang, and J. Jeong, "High dielectric constant TiO2 thin films on a Ru electrode grown at 250 degrees C by atomic-layer deposition," *Applied Physics Letters,* vol. 85, pp. 4112-4114, 2004.
[126] H. S. Park, J. S. Min, J. W. Lim, and S. W. Kang, "Theoretical evaluation of film growth rate during atomic layer epitaxy," *Applied Surface Science,* vol. 158, pp. 81-91, 2000.
[127] A. Rahtu, M. Ritala, and M. Leskela, "Atomic layer deposition of zirconium titanium oxide from titanium isopropoxide and zirconium chloride," *Chemistry of Materials,* vol. 13, pp. 1528-1532, 2001.
[128] Y. Gao, "In-situ IR and spectroscopic ellipsometric analysis of growth process and structural properties of Ti1-xNbxO2 thin films by metal-organic chemical vapor deposition," *Thin Solid Films,* vol. 346, pp. 73-81, 1999.
[129] G. A. Battiston, R. Gerbasi, M. Porchia, and A. Marigo, "INFLUENCE OF SUBSTRATE ON STRUCTURAL-PROPERTIES OF TIO2 THIN-FILMS OBTAINED VIA MOCVD," *Thin Solid Films,* vol. 239, pp. 186-191, 1994.
[130] M. Kemell, M. Ritala, M. Leskela, R. Groenen, and S. Lindfors, "Coating of Highly Porous Fiber Matrices by Atomic Layer Deposition," *Chemical Vapor Deposition,* vol. 14, pp. 347-352, 2008.
[131] "International Technology Roadmap for Semiconductors," International Sematech, Texas, 2005.
[132] J. Robertson, "High dielectric constant oxides," *European Physical Journal-Applied Physics,* vol. 28, pp. 265-291, 2004.
[133] F. Wiest, V. Capodieci, O. Blank, M. Gutsche, J. Schulze, I. Eisele, J. Matusche, and U. I. Schmidt, "Conformal aluminum oxide coating of high aspect ratio structures using metalorganic chemical vapor deposition," *Thin Solid Films,* vol.

496, pp. 240-246, 2006.
[134] P. C. Stair, C. Marshall, G. Xiong, H. Feng, M. J. Pellin, J. W. Elam, L. Curtiss, L. Iton, H. Kung, M. Kung, and H. H. Wang, "Novel, uniform nanostructured catalytic membranes," *Topics in Catalysis,* vol. 39, pp. 181-186, 2006.
[135] M. Berginski, J. Huepkes, W. Reetz, B. Rech, and M. Wuttig, "Recent development on surface-textured ZnO : Al films prepared by sputtering for thin-film solar cell application," *Thin Solid Films,* vol. 516, pp. 5836-5841, 2008.
[136] E. R. Parker, B. J. Thibeault, M. F. Aimi, M. P. Rao, and N. C. MacDonald, "Inductively coupled plasma etching of bulk titanium for MEMS applications," *Journal of the Electrochemical Society,* vol. 152, pp. C675-C683, 2005.
[137] G. Xiong, J. W. Elam, H. Feng, C. Y. Han, H. H. Wang, L. E. Iton, L. A. Curtiss, M. J. Pellin, M. Kung, H. Kung, and P. C. Stair, "Effect of atomic layer deposition coatings on the surface structure of anodic aluminum oxide membranes," *Journal of Physical Chemistry B,* vol. 109, pp. 14059-14063, Jul 2005.
[138] A. C. Jones, H. C. Aspinall, P. R. Chalker, R. J. Potter, K. Kukli, A. Rahtu, M. Ritala, and M. Leskela, "Some recent developments in the MOCVD and ALD of high-kappa dielectric oxides," *Journal of Materials Chemistry,* vol. 14, pp. 3101-3112, 2004.
[139] M. K. Gobbert, V. Prasad, and T. S. Cale, "Modeling and simulation of atomic layer deposition at the feature scale," *Journal of Vacuum Science & Technology B,* vol. 20, pp. 1031-1043, 2002.
[140] S. O. Kucheyev, J. Biener, T. F. Baumann, Y. M. Wang, A. V. Hamza, Z. Li, D. K. Lee, and R. G. Gordon, "Mechanisms of atomic layer deposition on substrates with ultkahigh aspect ratios," *Langmuir,* vol. 24, pp. 943-948, 2008.
[141] S. K. Kim, K. M. Kim, O. S. Kwon, S. W. Lee, C. B. Jeon, W. Y. Park, C. S. Hwang, and J. Jeong, "Structurally and electrically uniform deposition of high-k TiO2 thin films on a Ru electrode in three-dimensional contact holes using atomic layer deposition," *Electrochemical and Solid State Letters,* vol. 8, pp. F59-F62, 2005.
[142] S. W. Jeong, H. J. Lee, K. S. Kim, M. T. You, Y. Roh, T. Noguchi, W. Xianyu, and J. Jung, "Effects of annealing temperature on the characteristics of ALD-deposited HfO2 in MIM capacitors," *Thin Solid Films,* vol. 515, pp. 526-530, 2006.